EFFECT OF HYDROGEN AND MAGNETIC FIELD ON THE MECHANICAL BEHAVIOR OF MAGNETOSTRICTIVE IRON-GALLIUM ALLOYS

by

Meenakshisundaram Ramanathan

A dissertation submitted to the faculty of
The University of Utah
in partial fulfillment of the requirements for the degree of

Doctor of Philosophy

Department of Metallurgical Engineering

University of Utah

August 2012

The University of Utah Graduate School

STATEMENT OF DISSERTATION APPROVAL

The dissertation of **Meenakshisundaram Ramanathan**

has been approved by the following supervisory committee members:

Sivaraman Guruswamy	, Chair	**4-13-2012** Date Approved
Zhigang Zak Fang	, Member	**4-13-2012** Date Approved
Michael L. Free	, Member	**4-13-2012** Date Approved
Michael K. McCarter	, Member	**4-13-2012** Date Approved
Michael S. Moats	, Member	**4-13-2012** Date Approved

and by **Jan D. Miller** , Chair of

the Department of **Metallurgical Engineering**

and by Charles A. Wight, Dean of The Graduate School.

ABSTRACT

Magnetostrictive Fe-Ga and other iron-based alloys are candidates for use in sensing, actuation and large-scale energy harvesting applications. Exposure to aqueous electrochemical environments is anticipated in some of these applications which could potentially introduce hydrogen into the alloy and cause severe ductility reduction due to hydrogen embrittlement. These alloys may also be simultaneously exposed to magnetic field. This study therefore examines the effect of hydrogen and magnetic field on the mechanical behavior of these alloys. This study could also provide an understanding of the relationship between hydrogen embrittlement and magnetoelastic behavior in these alloys.

In this work, the effect of hydrogen and magnetic field on the fracture behavior of [100]-oriented Fe-17.5 at.% Ga alloy single crystals and polycrystalline Fe-15 at.% Ga alloy were examined. Three-point bend tests and tensile tests were used to study the fracture behavior. Tests were done in different conditions to understand the effect of hydrogen and magnetic field on the fracture behavior of these materials. Hydrogen loading was done by in-situ electrochemical charging and magnetic field was applied to the samples either by using $Nd_2Fe_{14}B$ permanent magnets or by using solenoid coils. Before doing the three-point bend test on the Fe-Ga single crystal samples, tests were done using high-strength AISI 4340 steel to optimize the testing procedures and parameters.

In all cases, the samples tested with hydrogen charging show a drastic reduction in ductility and fracture stress values. In the case of [100]-oriented Fe-17.5 at.% Ga alloy single crystal samples tested with hydrogen charging, the presence of applied magnetic field increased the stress required for fracture and a corresponding increase in bending strain values. This is attributed to a decrease of the elastic modulus values on the application of magnetic field in this magnetostrictive alloy. The hydrogen embrittlement was characterized by a change in fracture surface from a ductile type fracture to a brittle cleavage type fracture. Acoustic emission signals collected during the test correspond to the fracture behavior.

TABLE OF CONTENTS

LIST OF TABLES

LIST OF FIGURES

NOMENCLATURE

List of Symbols

B	Magnetic induction
E_{me}	Magnetoelastic energy
H	Magnetic field strength
H_{ci}	Intrinsic coercivity
m	Magnetic moment
M	Magnetization
M_s	Saturation magnetization
M_r	Remanence
T_c	Curie temperature
ε	Tensile strain
ε_b	Bending strain
λ	Magnetostrictive strain / magnetostriction
λ_s	Saturation magnetostriction
λ_t	Transverse magnetostriction
μ	Magnetic permeability
σ	Tensile stress
σ_b	Bending stress

σ_s	Specific magnetization
χ_m	Magnetic susceptibility

List of Acronyms

A	Ampere
AE	Acoustic emission
BCC	Body centered cubic
DG	Directionally grown
emu	Electromagnetic unit of magnetic moment
FCC	Face centered cubic
G	Gauss
H	Henries
HAR	Hydrogen absorption reaction
HE	Hydrogen embrittlement
HEDE	Hydrogen enhanced decohesion
HEI	Hydrogen embrittlement index
HELP	Hydrogen enhanced localized plasticity
HER	Hydrogen evolution reaction
NDT	Nondestructive testing
Oe	Oersteds
ppm	Parts per million
RE	Rare-earth

SEM	Scanning electron microscopy
T	Tesla
TEM	Transmission electron microscopy
UHP	Ultra high purity
VSM	Vibrating sample magnetometer
Wb	Weber

ACKNOWLEDGEMENTS

I take this opportunity to sincerely thank my advisor, Professor Sivaraman Guruswamy, for all the support and encouragement during the last several years of my graduate life. He has been a great motivator, mentor and teacher, whose energy and enthusiasm for research has motivated me to be a good student and researcher. Apart from research, he has been greatly helpful with improving my writing and presentation skills. He has always been accessible, willing to help and appreciative of new ideas, which made my PhD life challenging and rewarding.

I would also like to thank Professor Zhigang Zak Fang, Professor Michael Free, Professor Michael McCarter and Professor Michael Moats for their time by being in my graduate supervisory committee and for helping me by sharing their knowledge and valuable suggestions.

I would like to thank the Department of Metallurgical Engineering and the University of Utah for giving me an opportunity to travel a long way from my home country, India, to do my graduate studies. I would also like to acknowledge the National Science Foundation for the support of this research work through the grant DMR-0854166. The electron microscopy was accomplished at the Electron Microscopy Center for Materials Research at the Argonne National Laboratory, a U.S. Department of Energy, Office of Science Laboratory, operated under Contract No: DE–AC02_06CH11357 by the University of Chicago, Argonne, LLC.

I would like to thank Dr. Gavin Garside for helping me during the first few months in the lab to learn the basic operations of various equipment. I would like to thank my labmates, Biswadeep Saha and Chai Ren, for their friendship and support during the entire period of my graduate studies. I would like to thank Abhijeet Shukla for helping me with potentiodynamic polarization measurements and Pei Sun for helping with some of the scanning electron microscopy work.

My special thanks go to the Metallurgical Engineering office staff, Karen Haynes, Kay Argyle and Evelyn Wells, who have always been enthusiastic and willing to lend a helping hand. I would also like to thank Mining Engineering office staff member, Pamela Hofmann, for helping with binding my several versions of reports in the process of thesis writing.

Finally, I would like to record my sincere thanks and love for my parents and brother who have always been behind me as a morale support and encouragement in all the ventures I take.

CHAPTER 1

INTRODUCTION

Magnetostrictive materials exhibit reversible strains and changes in elastic properties in the presence of an applied magnetic field and the reciprocal effect of changes in magnetic properties with the application of stress [1]. Joule magnetostriction refers to the phenomenon of changes in linear dimensions on the application of a magnetic field.

Although the phenomenon of magnetostriction was observed by Joule as early as 1840, the first application of these materials was during the World War II period in underwater sonar devices. The earliest magnetostrictive alloys used in engineering applications were Ni-based alloys with saturation magnetostriction values in the range of -100×10^{-6} to 100×10^{-6} [2]. Rare-earth elements Tb and Dy exhibit large basal plane magnetostriction of about 1 %. But their low ordering temperatures restrict their use to cryogenic temperatures. Subsequently, an intense search for magnetostrictive materials with high magnetostriction at room temperature led to the discovery of Laves phase compound, $TbFe_2$, with a room temperature magnetostriction of about 0.4 % at an applied magnetic field of 25 kOe. Partial substitution of Tb with Dy in $TbFe_2$ decreased the magnetization anisotropy and therefore hysteresis. At room temperature, minimum anisotropy and hysteresis were obtained in $Tb_{0.3}Dy_{0.7}Fe_2$ (Terfenol-D) alloy with a room

temperature magnetostriction of about 0.16-0.24 % strain along the [111] crystallographic direction at an applied magnetic field of about 2 kOe. The main drawbacks of Terfenol-D are the difficulty in obtaining preferred [111] crystallographic orientation and brittleness, and its cost.

Magnetostrictive materials that overcome the limitations of Terfenol-D and offer adequate magnetostriction with desired characteristics such as large low-field magnetostriction, low cost, high mechanical strength, good ductility, negligible hysteresis and higher operating temperatures are of interest for various engineering applications. This led to the focus on developing Fe-based binary alloys. Fe-Al and Fe-B alloys have long been known for their low field magnetostriction. It was hypothesized by Guruswamy et al. [3] that the addition of nonmagnetic Ga to Fe results in dramatic increase in the Joule magnetostriction of Fe. Subsequent work on single crystal and polycrystalline Fe-Ga alloys confirmed that Ga addition can dramatically increase the magnetostriction of Fe [4-16], with magnetostriction values that were about three times those observed in the Fe-Al system and ten times those observed in pure iron. Fe-Ga alloys have an excellent combination of large low-field magnetostriction, high mechanical strength, good ductility, toughness and low associated cost.

Fe-Ga and other ferrous alloys such as Fe-Al, Fe-Mo and Fe-W that exhibit large magnetostrictive behavior at low magnetic fields are candidates for use in sensing, actuation and large-scale energy harvesting applications such as that from wind and ocean. These magnetostrictive alloys, during their applications, are likely to be exposed to aqueous electrochemical environments. This exposure could potentially introduce hydrogen into the alloy, with the dissolved hydrogen concentration in the Fe alloy lattice

determined by the current density associated with electrochemical process in the aqueous environment [17].

Hydrogen present even in few parts per million is sufficient to embrittle steels and Fe alloys at room temperature [18]. Embrittlement, either ductile or brittle, can be described as a condition which decreases the toughness of the material or increases the ease of crack growth. Hydrogen embrittlement in Fe-based alloys has been studied by many workers during the past few decades and various mechanisms have been proposed [19-27]. The effect of hydrogen on the mechanical properties is dependent on different conditions such as the type of loading, metallurgical structure, impurity level, strength level, load level, strain rate, type of charging and charging current density [28]. The hydrogen embrittlement is more pronounced at room temperature, at lower strain rate and is more severe in the regions of maximum triaxiality like a void or notch [20].

In most cases, hydrogen exposure is through an electrochemical process in aqueous corroding environments and in many of these environments, the alloy components are also prone to be exposed simultaneously to electrically induced magnetic fields, which are also believed to affect the hydrogen embrittlement susceptibility of these alloys. Therefore, it is also important to study the effect of magnetic field on the hydrogen embrittlement susceptibility.

Magnetization is believed to affect the hydrogen embrittlement susceptibility of iron and its alloys. A strong applied magnetic field near saturation can affect the domain structure and therefore could change the interstitial-dislocation interaction [29, 30], which affects the mechanical properties of the alloys. Magnetization is also reported to affect the hydrogen absorption reaction and thereby, it affects the hydrogen embrittlement

behavior [31, 32]. The influence of magnetic field on the mechanical behavior of ferromagnetic alloys such as Fe and steel containing hydrogen has been examined in the past. Such studies on Fe-Ga alloys is of particular interest, as these Fe-Ga alloys would experience significant changes in internal strains due to magnetostriction and changes in elastic modulus in addition to changes in magnetization with the application of magnetic field.

Plastic deformation and fracture of solid materials is accompanied by spontaneous emission of elastic waves, leading to low-amplitude acoustic emission signals [33-36]. Acoustic emission generated during fracture of materials contains potential information about the fracture onset and propagation [37]. Elastic energy released during crack initiation and propagation can be detected and recorded using acoustic emission measurements. Onset of deformation of material and failure can be detected by acoustic emission. Detection and analysis of acoustic emission signals during the fracture of hydrogen charged Fe-Ga alloy specimens under mechanical loading could provide a correlation between acoustic emission activity and the embrittlement process. Therefore, acoustic emission analysis may be used as a supplementary tool in understanding the failure mechanisms associated with hydrogen embrittlement [38-40].

In this work, the effect of hydrogen and magnetic field on the mechanical behavior of magnetostrictive Fe-17.5 at.% Ga alloy single crystal were examined using three-point bend tests. The use of single crystal samples in this work minimizes the number of material variables and therefore makes it easier to examine the influence of hydrogen and magnetic field. The use of single crystal samples also allows a better higher bound estimate for cleavage stress in these Fe-based alloys. Due to the difficulty in

obtaining single crystals of reasonable size, limited three-point bend tests were carried out on single crystal samples. In order to optimize the three-point bend testing procedures and parameters, high-strength AISI 4340 steel, a material that is well characterized for its hydrogen embrittlement susceptibility, was used. Hydrogen was introduced into the alloy by in-situ cathodic charging in an aqueous H_2SO_4 electrolyte. The magnetic field was applied using $Nd_2Fe_{14}B$ permanent magnets attached to the sample or by using a solenoid coil. The fracture surfaces were examined using a scanning electron microscope. The acoustic emission signals were collected continuously during the bend test to examine the relative magnitudes of energy release during fracture onset and propagation. Saturation magnetization and magnetostrictive strain values of the Fe-17.5 at.% Ga alloy were also determined. Tensile tests were used to study the hydrogen embrittlement behavior in polycrystalline magnetostrictive Fe-15 at.% Ga alloys and in this case, the magnetic field was applied using a solenoid coil.

CHAPTER 2

BACKGROUND

This chapter will present a brief theoretical background on various aspects of magnetism, magnetostriction, hydrogen embrittlement and acoustic emission measurement techniques.

2.1 Basic Terms in Magnetism

2.1.1 Magnetic Field Strength / Intensity (H)

The externally applied magnetic field is referred to as the magnetic field strength or field intensity. If the magnetic field (H) is generated by means of a cylindrical solenoid coil, with number of turns N, length *l* and carrying a current of magnitude I, then

$$H = N I / l \tag{2.1}$$

The SI unit of field strength is A/m and the CGS unit is Oe [1].

2.1.2 Magnetic Moment (m)

Considering a magnet of pole strength + *p* and – *p* separated by length *l*, the magnetic moment can be expressed as,

$$m = p\, l \tag{2.2}$$

The SI unit for magnetic moment is Am^2. Magnetic moment can also be defined as the maximum torque experienced by the magnet when placed in a unit external magnetic field. Hence, the CGS unit of magnetic moment is erg/oe or emu (electromagnetic unit of magnetic moment).

2.1.3 Magnetization (M)

The magnetization or intensity of magnetization can be defined as the magnetic moment (m) per unit volume (v) of the material.

$$M = m / v \tag{2.3}$$

It is sometimes convenient to refer to the value of magnetization in terms of unit mass (w) rather than unit volume (v), and in this case, it is termed as specific magnetization (σ).

$$\sigma = m / w \tag{2.4}$$

The SI unit of magnetization is A/m and CGS unit is emu/cm^3 (emu/g in case of specific magnetization).

2.1.4 Magnetic Induction / Magnetic Flux Density (B)

Magnetic induction or magnetic flux density represents the magnitude of the internal field strength within a substance that is subjected to an applied magnetic field (H). The SI unit for magnetic induction is Wb/m^2 (webers per square meter) or T (Tesla) and the CGS unit is G (Gauss) [41].

2.1.5 Magnetic Permeability (μ)

Ratio of magnetic induction (B) to applied magnetic field (H) is termed magnetic permeability. It is the property of the specific medium though which the magnetic field (H) passes and in which the magnetic induction (B) is measured.

$$\mu = B / H \tag{2.5}$$

The SI unit of permeability is Wb/Am (webers per ampere meter) or H/m (henries per meter) and it has no units in the CGS system. The permeability of a vacuum is a universal constant that has a value of $4\pi \times 10^{-7}$ H/m.

2.1.6 Magnetic Susceptibility (χ_m)

Ratio of magnetization (M) to applied magnetic field (H) is termed magnetic susceptibility (χ_m). It is a dimensionless quantity and has no units.

$$\chi_m = M / H \tag{2.6}$$

2.2 Magnetization Curve and Hysteresis Loop

Magnetic materials can be classified as magnetically soft or hard based on their magnetization behavior. Materials exhibiting low coercivity values (small hysteresis) are said to be magnetically soft, whereas materials with high coercivity (large hysteresis) are said to be magnetically hard [1]. The nature of a magnetization curve also depends on the physical condition of the material, and is affected by plastic deformation and thermal treatments.

Figure 2.1 shows a typical magnetization curve of a ferromagnetic material, with change in magnetization (M) as a function of applied magnetic field (H). Application of magnetic field to a material in a demagnetized state results in a rapid initial increase in magnetization followed by a gradual increase. As the applied field increases, the magnetization reaches a maximum at a certain magnetic field and remains constant with further increase of magnetic field. This magnetization value is termed saturation magnetization (M_s). On reducing the magnetic field, the magnetization value is seen to decrease, but does not follow the same path. When the magnetic field is reversed to zero, the corresponding magnetization value does not reach zero and this value of magnetization on the removal of the field is termed as remanence (M_r). To remove this remanent magnetization, the magnetic field is applied in the opposite direction. The magnetic field that is required to bring the magnetization to zero is termed as intrinsic coercivity (H_{ci}). As the field in the opposite direction is increased, at a certain magnetic field, the magnetization reaches negative saturation. On reversing the magnetic field, the magnetization follows the curve with negative remanence, zero magnetization and finally reaches the positive saturation magnetization, completing the hysteresis loop.

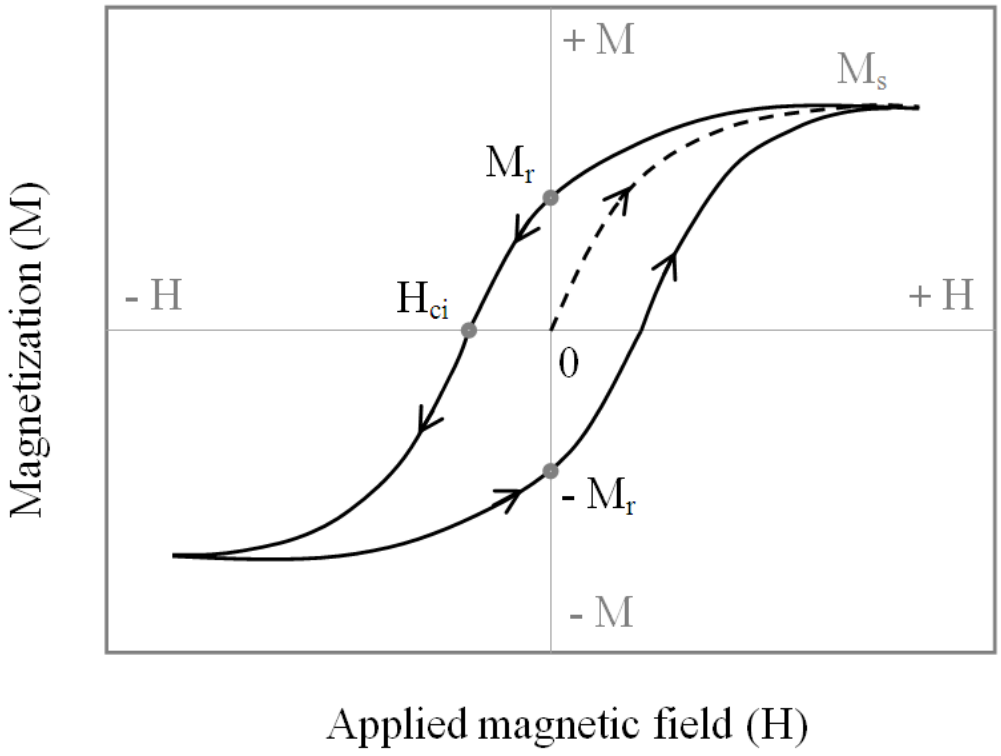

Figure 2.1 A typical hysteresis curve showing magnetization versus applied magnetic field.

2.3 Magnetic Anisotropy

One factor that affects the shape of the hysteresis loop is the magnetic anisotropy, which refers to the dependence of the magnetic properties of a material on the direction in which they are measured. The main types of magnetic anisotropy are: (i) magnetocrystalline anisotropy, (ii) shape anisotropy and (iii) stress anisotropy.

It is easier to magnetize a single crystal in a particular crystallographic orientation than in others. This property of easy magnetization in a particular crystallographic direction in a single crystal is called magnetocrystalline anisotropy. The direction of easy magnetization of a crystal is the direction of spontaneous domain magnetization in the demagnetized state [1]. For example, in the case of an iron single crystal, <100> is the easy magnetization direction, and therefore, the domains of iron in a demagnetized state, below Curie temperature, are spontaneously magnetized to saturation in <100> directions, as shown schematically in Figure 2.2 (a). On applying the magnetic field (H) in [100] direction, the [100]-oriented domains will grow in volume by the mechanism of domain-wall motion (Figure 2.2 (b)). At saturation, there is only one single domain oriented in [100] direction (Figure 2.2 (c)).

There is no net crystal anisotropy in the case of a polycrystalline material with random grain orientation. If the material is spherical, irrespective of the direction, it can be uniformly magnetized with the same applied magnetic field [1]. But if the material is nonspherical, it is easier to magnetize it along the longer axis than along the shorter axis. This is referred to as shape anisotropy. The reason for this is the demagnetizing field which is stronger along the shorter axis than along the longer axis.

The applied mechanical stress in a material can alter the magnetic domain

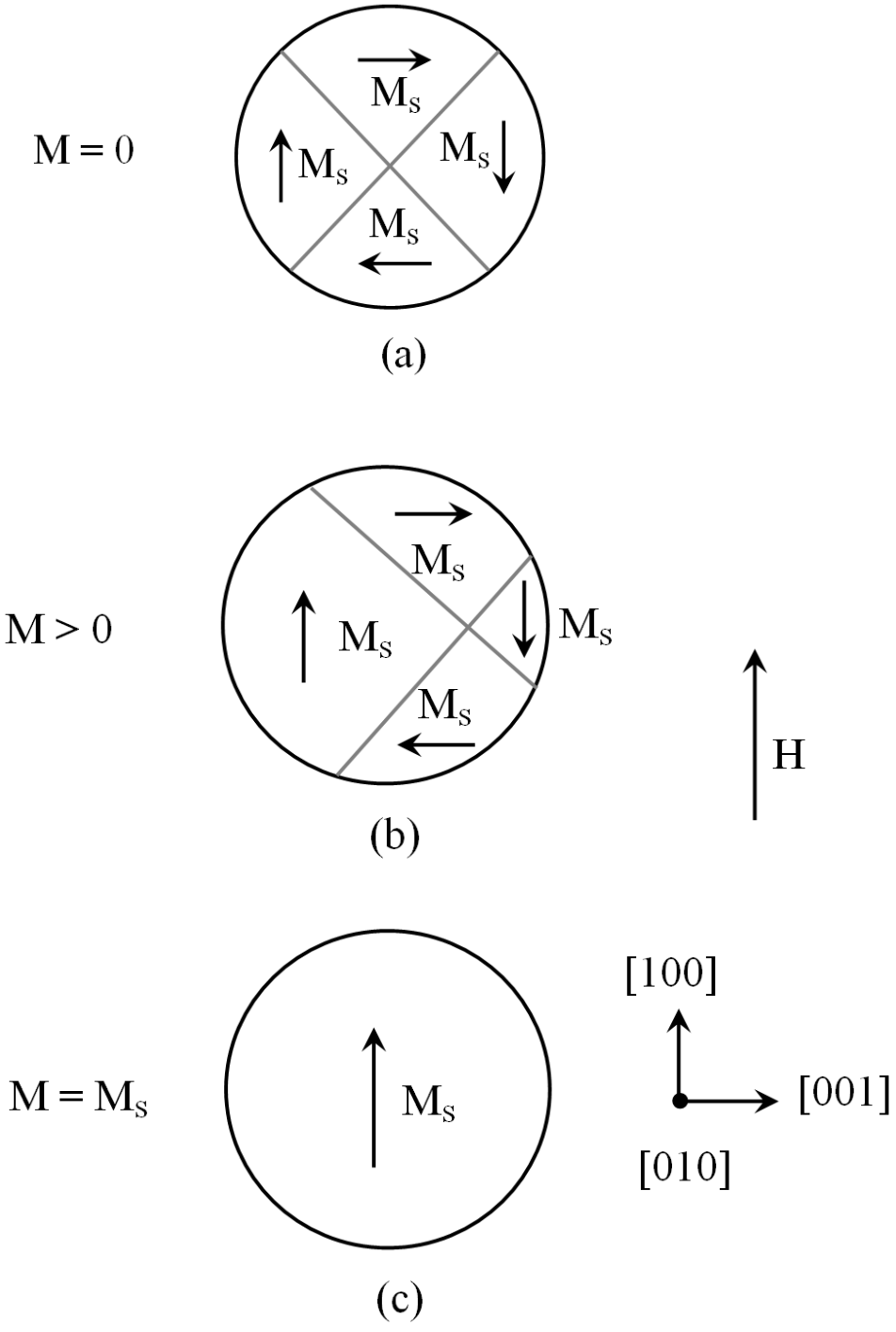

Figure 2.2 A schematic of domain structure in a single crystal of iron; magnetic field applied along [100] direction (adapted from reference [1]).

structure, and so it is another major source of anisotropy. This stress anisotropy is related to the phenomenon of magnetostriction [42].

2.4 Magnetostriction

It was observed by English physicist James Prescott Joule as early as 1842 that an iron rod when magnetized lengthwise increased in length. Change in the dimension of a material body on application of magnetic field is termed as magnetostriction [1, 2, 43]. This magnetostrictive strain is given as a fractional change in length ($\Delta l/l$) and is denoted by the symbol λ, to differentiate it from the strain (ε) caused by application of stress. The λ value measured at magnetic saturation is termed as saturation magnetostriction (λ_s) and magnetostriction in general, if not mentioned specifically, is a term used to denote saturation magnetostriction.

There are two aspects to magnetostriction. The first is the anisotropic part which causes anisotropic change in dimension, such as a change in length, and this is termed Joule magnetostriction. A schematic diagram of Joule magnetostriction is shown in Figure 2.3 (a). The second aspect is the isotropic part which causes a change in volume of the material and is termed volume magnetostriction.

Although every material exhibits a magnetostrictive response, the λ_s is usually very small even in strong ferromagnetic materials and typically on the order of 10^{-5}. In weakly magnetic materials, this effect is even smaller, by about two orders of magnitude and can be observed only in very strong magnetic fields. The value of λ_s can be positive, negative or, in some alloys, zero at certain temperatures. The value of λ varies with magnetization which depends on applied magnetic field (H). Figure 2.3 (b) shows a

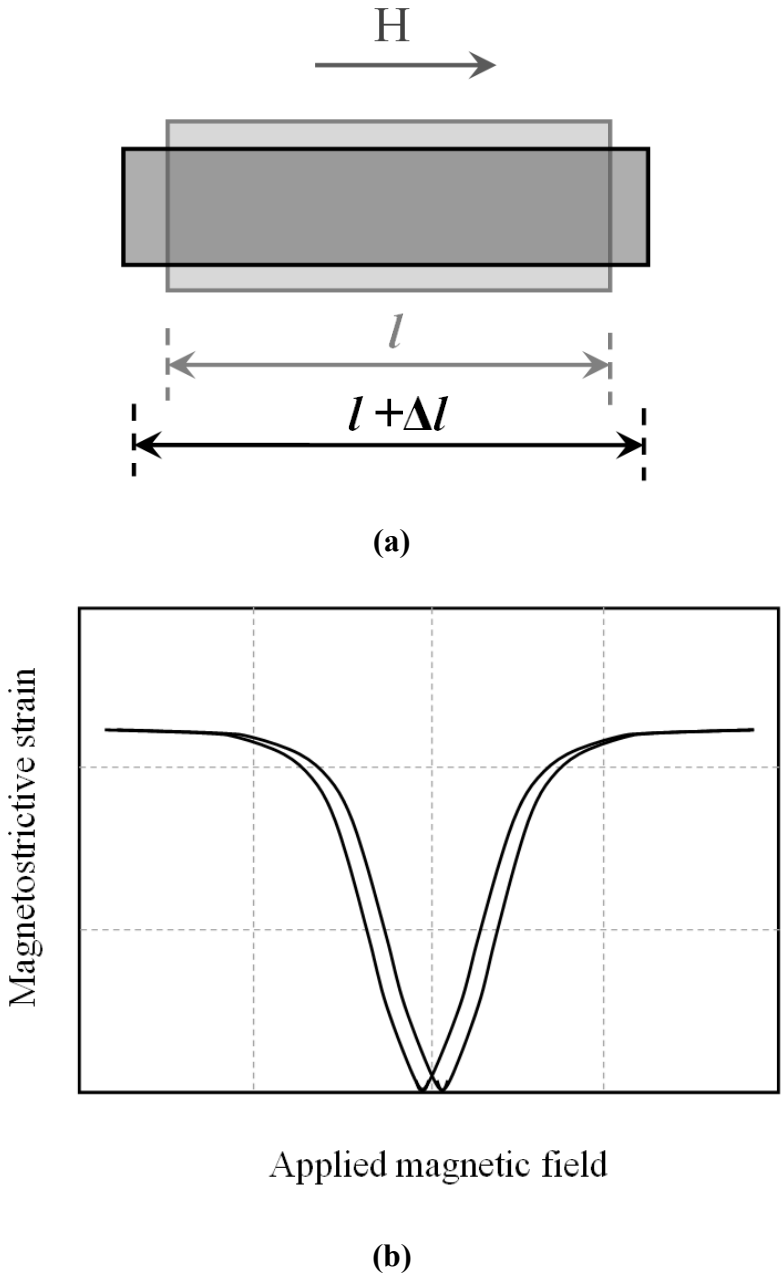

Figure 2.3 Joule magnetostriction phenomenon: (a) schematic; (b) typical magnetostriction plot showing magnetostrictive strain versus applied magnetic field.

typical magnetostriction plot showing magnetostrictive strain versus applied magnetic field [42]. The process of magnetization occurs by two mechanisms, domain wall motion and domain rotation. The domain rotation contributes to most of the Joule magnetostriction. This increase in linear dimension is accompanied by a transverse magnetostriction (λ_t) which causes reduction of transverse dimension in opposite sign given by the equation,

$$\lambda_t = -1/2\ \lambda \qquad (2.7)$$

2.4.1 Physical Origin of Magnetostriction

The phenomenon of magnetostriction is due to a coupling between the spin and the orbital motion of the electrons in the material [1]. Above the Curie temperature (T_c), the net magnetic moment of each atom is randomly oriented and is in a paramagnetic state, as shown in the topmost row of Figure 2.4. Now, considering the spin-orbit coupling to be very strong, just below T_c, the magnetic moments are spontaneously oriented in the direction of crystal anisotropy. This leads to a spontaneous magnetostrictive strain within each domain. The net moments are randomly oriented and the contribution of the magnetostrictive strain in each domain to the total strain in the material body is given as $\Delta L'/L'$. On applying a strong magnetic field, the moments of the various domains rotate towards the applied field direction, or the domains favorably oriented towards the field grow at the expense of other domains by the movement of domain walls. The magnetostrictive strain along the length direction is given as $\Delta L/L$.

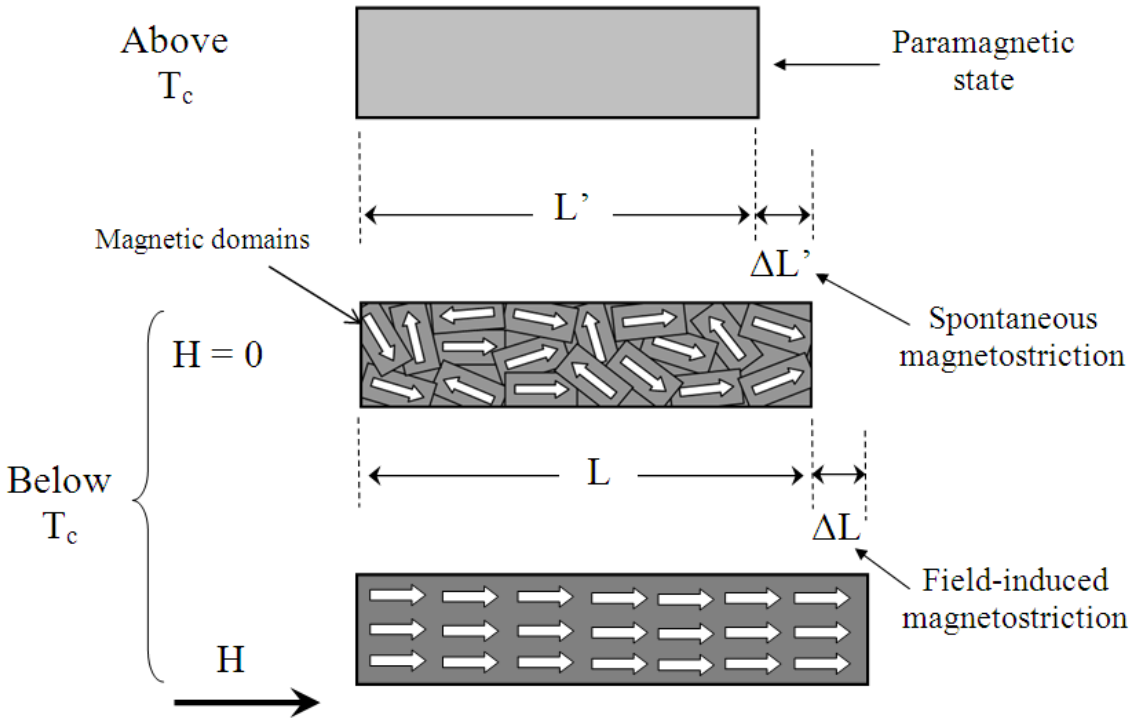

Figure 2.4 Mechanism of magnetostriction.

2.4.2 Magnetostriction Measurement Techniques

The magnetostrictive strains can be as small as 10^{-9} and as large as $2x10^{-3}$. Small strains can only be measured by adequate magnification by mechanical, electrical or optical devices. Early Joule magnetostriction measurements were carried out using optical devices to magnify the magnetostrictive strain to an observable magnitude. Electrical methods were later developed, and the most widely used among the electrical methods is the strain gage method that was developed by Goldman in 1947 [44]. More accurate and sensitive methods have been developed over the years. Table 2.1 summarizes the various methods used for measuring magnetostriction coefficients with sample capability, their sensitivity and the temperature range of use [2].

In the strain gage method, precision electrical-resistance strain gage is used. This strain gage is made from an alloy wire or foil grid, embedded in a thin paper or polymer sheet, and is cemented to the sample. When the sample dimension changes, the grid of the strain gage attached to it is also strained and this causes a change in electrical resistance of the gage. The resistance of the gage is calibrated for the strain measurements. Due to small changes in resistance values, the measurements are carried out in a bridge circuit. The strain gages are cemented to the sample using special adhesives that secure a perfect contact between the sample and the resistance elements.

The strain gage method is one of the most widely used methods for magnetostriction measurement because of the following advantages. First, it is one of the cheapest methods and can be used for measuring moderate to large magnetostriction (above 10^{-6}, sensitivity is typically 10^{-7}) [43]. The sample preparation is simple compared to other methods. Another advantage is that it is possible to attach multiple strain gauges

Table 2.1

Comparison of various methods used for magnetostriction coefficient measurements [2, 43].

Method	**Samples**	**Ultimate sensitivity**	**Temperature range (remarks)**
Strain gage extensometer	Bulk, ribbon	10^{-7}	4.2 – 700 K (caution: magnetoresistance)
Three-terminal capacitance	Bulk, ribbon	10^{-9}	0 – 400 K (with a lower sensitivity above 20 K)
Optical interferometer	Bulk, ribbon, wire	10^{-8}	4.2 – 300 K (sample preparation is delicate)
X-ray diffractometer	Bulk, ribbon, wire, thin film	10^{-5}	1.5 – 400 K
Wiedemann effect	Bulk, ribbon, wire	10^{-10}	1.5 – 400 K (sensitivity 10^{-13} is possible in a dynamic regime)
Tube type dilatometer	Bulk, ribbon	10^{-8}	1.5 – 1000 k (fragile)
Cantilever	Thin film	10^{-7}	1.6 – 400 K

on the sample to simultaneously measure longitudinal and transverse magnetostrictive strain values.

2.4.3 Magnetostriction Coefficient Measurement in Cubic Single Crystals

The magnetostriction coefficient, (3/2) λ_{100}, is an important material property and is an important parameter in various magneto-elastic equations. A single crystal sample with desired orientation is used for this measurement. A strain gage is cemented to one of the flat (001) faces of the oriented single crystal sample along the [100] direction, as shown in Figure 2.5 (a). The first measurement is done by magnetizing the sample along the [100] direction, and the magnetostrictive strain is measured along the same [100] direction (Figure 2.5 (b)). The second measurement is done by magnetizing the sample along the [010] direction, and the magnetostrictive strain is measured along the [100] direction (Figure 2.5 (c)). The difference between these two measurements gives the (3/2) λ_{100} value. The quantity so measured has a value independent of the nature of the demagnetized state of the specimen [1, 43].

2.5 Magnetomechanical Effect

There is a close connection between the magnetostriction of a material and its magnetic behavior under stress. The effect of stress on magnetization is called inverse magnetostrictive effect or magnetomechanical effect [1]. A material with positive magnetostriction will elongate when magnetized, and an applied tensile stress which elongates the material tends to increase the magnetization. In case of materials with

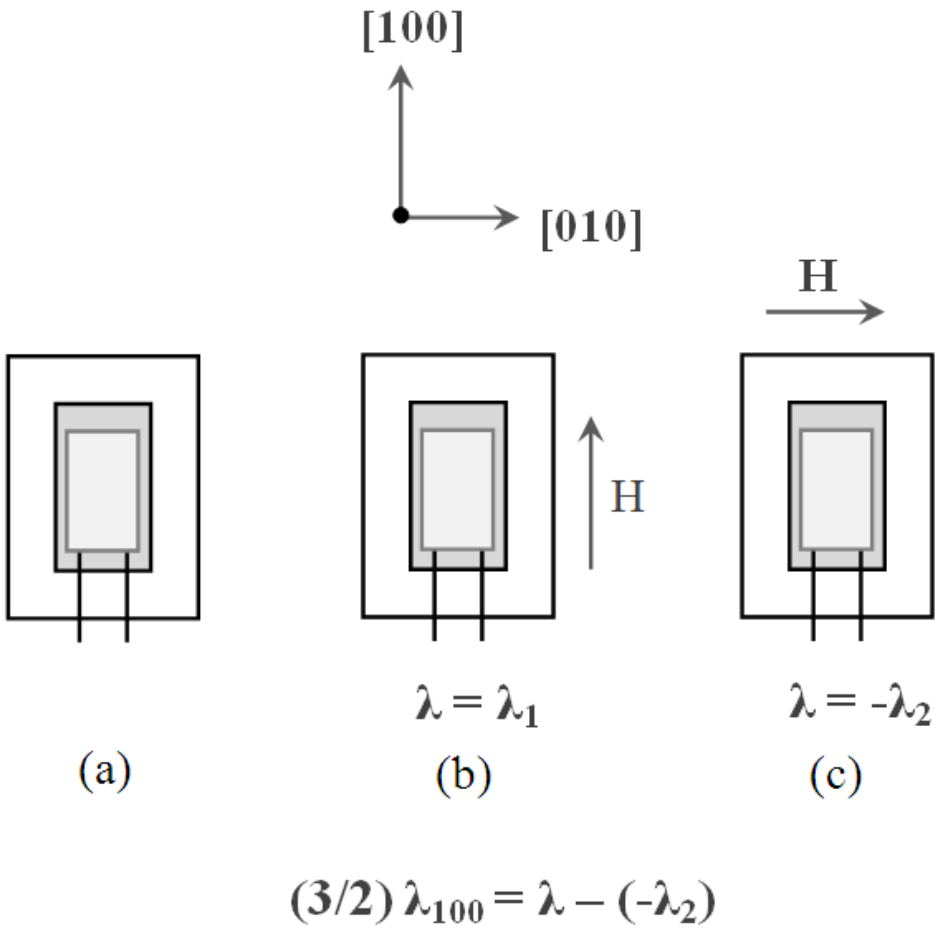

Figure 2.5 Magnetostriction coefficient measurement: (a) schematic of strain gage attached to (100) face of the sample along [100] direction; (b) magnetizing the sample along [100] direction and the magnetostrictive strain measured along the same [100] direction; (c) magnetizing the sample along [010] direction and the magnetostrictive strain measured along the [100] direction.

negative magnetostriction, this effect is reversed.

Figure 2.6 can be used to explain the reason as to why it is easy to magnetize a material with positive magnetostriction when stressed in tension. Let Figure 2.6 (a) represent a small portion of the material, comprising four domains, as shown schematically. The application of a small tensile stress to the demagnetized specimen (Figure 2.6 (b)) will cause domain walls to move in such a way as to decrease the volume of domains magnetized at right angles to the stress axis, because such domains have high magnetoelastic energy (E_{me}). These domains are completely eliminated by a higher value of stress (Figure 2.6 (c)) and E_{me} is now a minimum. The domain structure is now identical to that of a uniaxial crystal. Only a small applied magnetic field is now required to saturate the material, because transition from Figure 2.6 (c) to Figure 2.6 (d) can be accomplished by an easy 180° wall motion.

The same material (with positive magnetostriction) under compressive stress (Figure 2.7) is difficult to magnetize. This is due to the domain moment orientation in this case (Figure 2.7 (c)) being perpendicular to the stress direction, and so energy equal to the magnetoelastic energy, in the form of magnetic field, is needed to rotate the domain by 90° towards the field direction (Figure 2.7 (d)). Therefore, this makes it difficult to magnetize a material with positive magnetostriction under compressive stresses.

All the stresses mentioned here are well below the yield stress, beyond which the material undergoes a permanent change in dimensions and various magnetic properties will be affected.

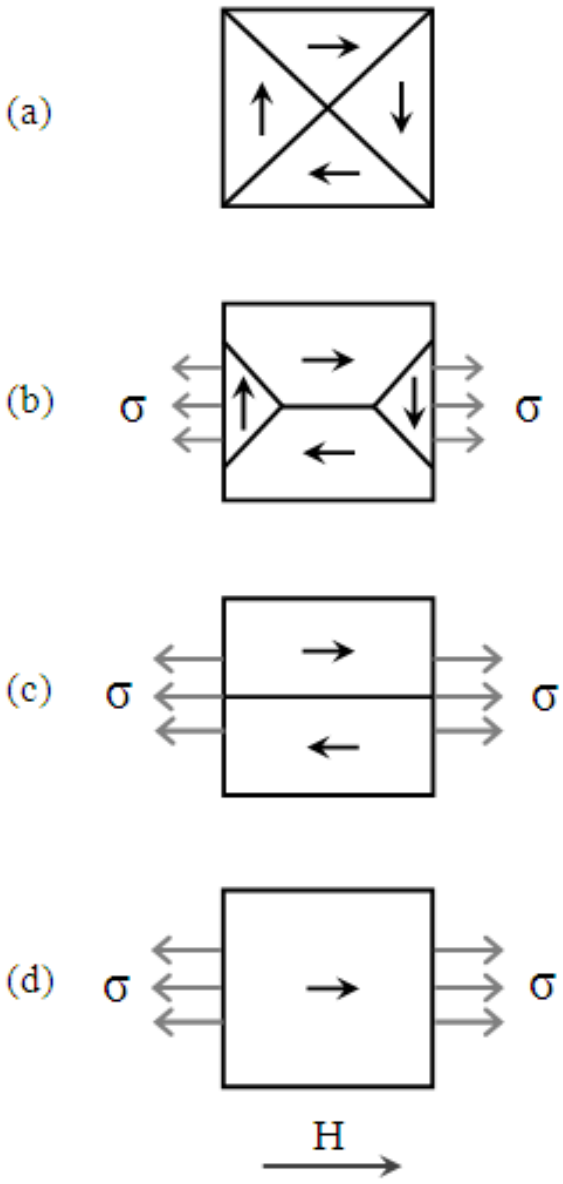

Figure 2.6 A schematic of magnetization of a material with positive magnetostriction under tensile stress (adapted from Reference [1]).

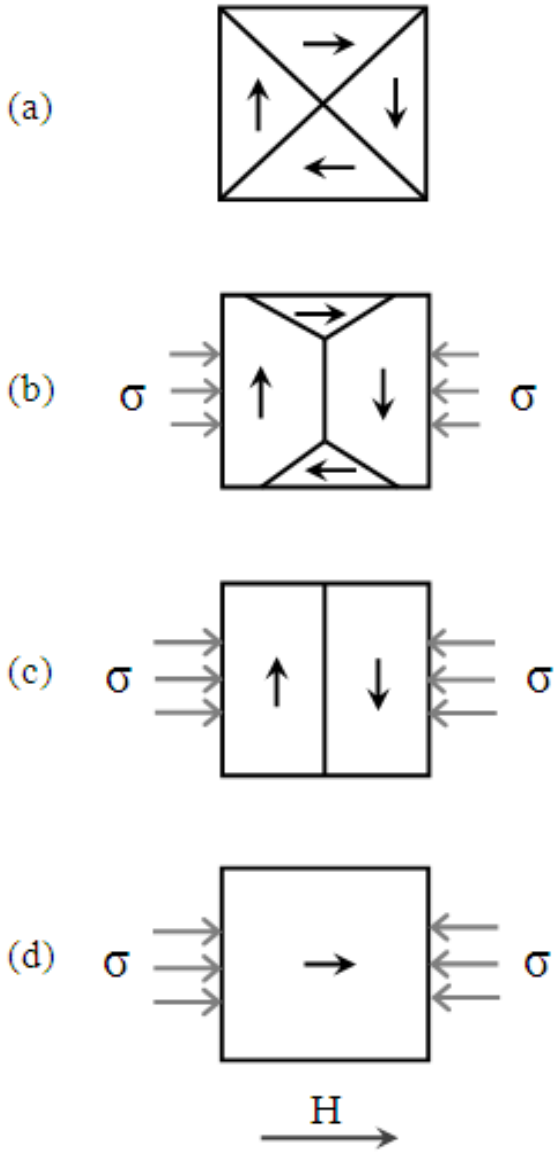

Figure 2.7 A schematic of magnetization of a material with positive magnetostriction under compressive stress (adapted from Reference [1]).

2.6 Magnetostrictive Materials

As mentioned earlier, magnetostrictive materials exhibit reversible strains and change in the elastic properties in the presence of applied magnetic field, or reciprocal effect of changes in magnetic properties with the application of stresses [1,2]. Magnetostrictive materials exhibit an inherent coupling between their mechanical and magnetic states, thereby making use of their direct effect in case of actuators or indirect effect in case of sensors [45]. Magnetostrictive materials are magnetic analogs to piezoelectric materials and exhibit a large displacement per single element. They can deliver large force and power, and can operate over a broad range of frequency. Materials that exhibit large Joule magnetostriction are of great interest in various applications like acoustic sensors and generators, underwater sonar devices, linear motors and actuators, positioning devices, mechanical vibration damping devices and torque sensors such as in antilock braking systems.

Although the phenomenon of magnetostriction was observed by Joule as early as in 1840s, the first application of this phenomenon was during World War II when pure Ni exhibiting magnetostrictive strain of about -77×10^{-6} along [001] was used in underwater sonar generators [2]. At room temperature, a single crystal of pure iron exhibits a magnetostrictive strain of about 20 ppm in [100] direction [46]. The earliest magnetostrictive alloys used in engineering applications were Ni-based alloys such as Ni-Fe, Ni-V, Ni-Cr, Ni-Mn, Ni-Co and Ni-Cu with saturation magnetostriction values ranging from -100×10^{-6} to 100×10^{-6}.

2.6.1 Rare-Earth-Based Magnetostrictive Materials

Later in the 1960s, it was discovered that rare-earth elements like Tb and Dy exhibit a large-basal plane magnetostrictive strain of about 1 % at cryogenic temperatures. They have a low Curie temperature of -53 °C and -184 °C, respectively. Their low ordering temperatures restrict their use to cryogenic temperatures. The search for magnetostrictive materials with large magnetostriction at room temperature led to discovery of rare-earth-based Laves phase compound, (RE)-Fe_2, which had a large room temperature magnetostriction. The $TbFe_2$ alloy has a room temperature magnetostriction of about 4000 ppm at an applied magnetic field of 25 kOe and $DyFe_2$ has a magnetostriction value of 1890 ppm in the [111] direction [2, 46]. However, achieving these values requires a very large magnetic field because of their large magnetization anisotropy and magnetostriction anisotropy.

Optimal alloying of $TbFe_2$ and $DyFe_2$ minimizes magnetization anisotropy and therefore hysteresis. The optimal composition varies with temperature. At room temperature, the minimum in anisotropy and hysteresis is achieved for $Tb_{0.3}Dy_{0.7}Fe_2$ (Terfenol-D) alloy. Room temperature magnetostriction observed in this alloy is about 0.16-0.24 % strain along the [111] crystallographic direction but the applied field was less than about 2 kOe. This value is still high, requiring substantial cooling of the field applying coils. One of the major drawbacks of Terfenol-D is the difficulty in obtaining preferred [111] crystallographic orientation, as the natural crystal growth direction is [112] and this reduces the magnetostriction values. The other limitations of this alloy are that it is brittle, has low Young's modulus and low tensile strength. This requires that the material is always kept under compressive stress, which is a constraint in component

design. In addition, the high temperature sensitivity and high field needed makes it necessary to have an elaborate cooling system. Moreover, it is expensive due to the presence of rare-earth elements in this alloy. So non-rare-earth-based alloys which can overcome the limitations of Terfenol-D were desired for widespread applications.

2.6.2 Non-Rare-Earth-Based Magnetostrictive Materials

Magnetostrictive materials that overcome the limitations of Terfenol-D and offer adequate magnetostriction with desired characteristics such as large low-field magnetostriction, low cost, high mechanical strength, good ductility, negligible hysteresis and higher operating temperatures were of interest. This led to the development of Fe-based binary alloys. Fe-Al and Fe-Be alloys have long been known for their low field magnetostriction. Fe-Be alloy single crystals with 11.3 at.% Be content is reported to have a magnetostrictive strain of about 110 ppm along [100] directions [47]. Fe-Al alloy single crystals with 19.2 at.% Al are reported to have a magnetostrictive strain of about 94 ppm in the [100] direction [48].

2.6.2.1 Iron-Gallium Alloys

It was hypothesized by Guruswamy et al. [3, 11] that the addition of non-magnetic Ga to Fe results in a dramatic increase in the magnetostriction of Fe. Subsequent work on single crystal and polycrystalline Fe-Ga alloys confirmed that Ga addition can dramatically increase the magnetostriction of Fe [4-8, 14], with a magnetostriction value observed to be about three times that of the Fe-Al system and ten times that observed in pure iron. Fe-Ga alloys have several advantages: they are cheaper

because of the use of less expensive non-rare-earth elements and use of conventional processing techniques they have high strength and ductility and they have negligible hysteresis and require lower saturation magnetic fields. These characteristics make this alloy system attractive for numerous energy conversion applications.

Figure 2.8 shows the Fe-rich portion of the Fe-Ga phase diagram and Table 2.2 gives the stable phases present in the Fe-Ga alloy over different temperature and composition ranges. Fe-Ga alloys can exist as single-phase terminal solid solutions with A2 structure for Ga contents as high as 36 at.% at 1037 °C and 11 at.% at room temperature. At Ga contents greater than 20 at.%, the A2 terminal solid solution phase can change to different ordered phases like α', α'', α''', β-Fe_3Ga and α-Fe_3Ga.

Ever since the invention of large magnetostriction in Fe-Ga alloys, considerable research has been carried out on various aspects of Fe-Ga alloys. This includes studies to understand the effect of: (i) Ga content [4, 15, 16, 49], (ii) substitution of Ga with other alloying elements [7, 8, 12, 50], (iii) thermal history [13, 49], and (iv) ordering on the magnetostriction of Fe-Ga alloys [5-8, 10, 13]. Mechanical properties of Fe-Ga alloys are also widely examined to understand the behavior and challenges of these materials under different loading conditions [45, 51-55].

Knowing the integrity of Fe-Ga alloys subjected to various environments is necessary to determine the performance of the material. Earlier studies of corrosion behavior on Fe-Ga alloys show that these alloys have good corrosion resistance [9, 10] and the magnetostriction affects the corrosion behavior of these alloys. There are only very few studies examining the effect of hydrogen on the properties of magnetostrictive materials. One such work by Sachdeva et al. [56] on the effect of hydrogen on corrosion

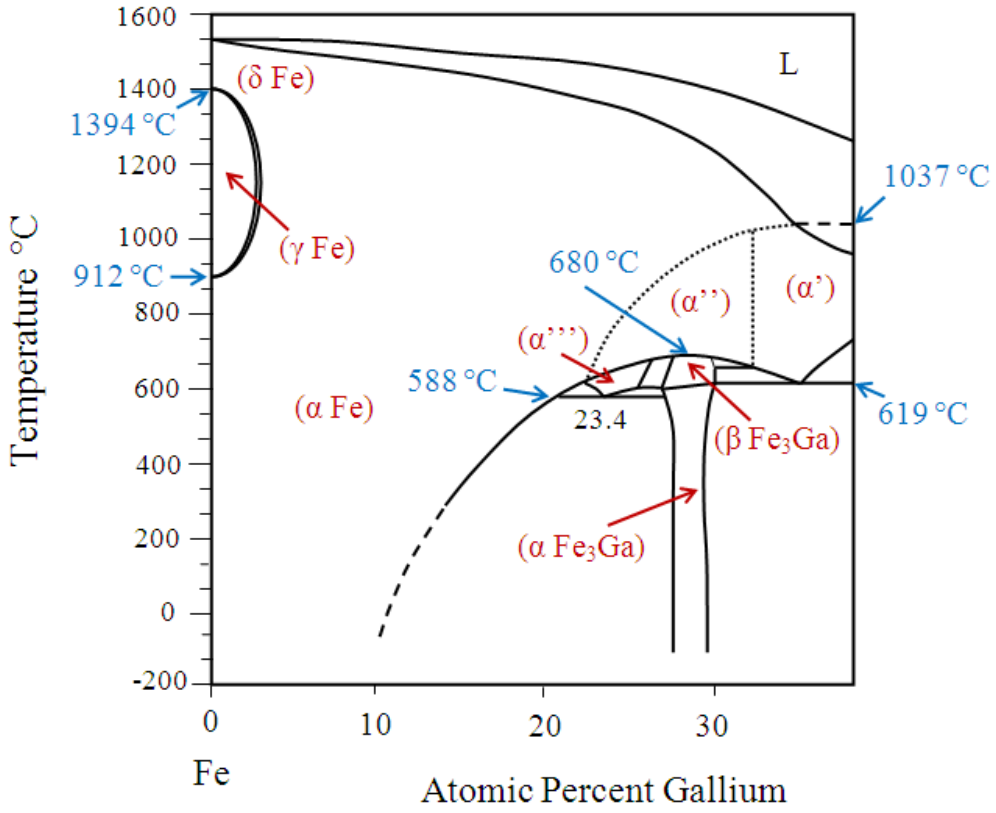

Figure 2.8 Iron rich portion of the Iron-Gallium phase diagram (adapted from reference [57]).

Table 2.2

Phases in Fe-rich portion of the Fe-Ga phase diagram [57].

Phase	**Composition at.% Ga**	**Strukturbericht designation**	**Pearson symbol**	**Space group**
γ Fe	0 to 2.8	A1	c*F*4	Fm3m
α Fe	0 to 36	A2	c*I*2	Im3m
α'	31.5 to 47.5	B2	c*P*2	Pm3m
α''	22.8 to 32.1	…	c*F*16	Fm3m
α'''	22.8 to 25.9	$D0_3$	c*F*16	Gm3m
βFe_3Ga	26 to 29	$D0_{19}$	h*P*8	P63/mmc
αFe_3Ga	26.2 to 29.2	$L1_2$	c*P*4	Pm3m

of Terfenol-D alloy is reported. The presence of hydrogen in Terfenol-D is reported to have a drastic decrease in the corrosion resistance and cause hydrogen embrittlement due to a hydride formation mechanism. The present work will be the first study reporting the results of hydrogen embrittlement behavior of magnetostrictive Fe-Ga alloys.

2.7 Hydrogen Embrittlement

Hydrogen interaction with materials leads to hydrogen embrittlement problems and is of high importance in the use of materials in diverse engineering applications. It was first reported by W. H. Johnson [58] in 1875 that the presence of hydrogen affects ductility and fracture stress of iron and steel. Since then, extensive research on hydrogen embrittlement of metals has been carried out. Hydrogen present even in few parts per million is sufficient to embrittle steels and iron alloys at room temperature [18]. Embrittlement can be described as a condition which decreases the toughness of the material or increases the ease of crack growth. The effect of hydrogen on the mechanical properties is dependent on different conditions such as the type of loading, metallurgical structure, impurity level, strength level, load level, strain rate, type of charging, charging current density, etc. [28].

2.8 Hydrogen Embrittlement Mechanisms

Systematic studies of hydrogen embrittlement have been widely carried out by many researchers, and various mechanisms have been proposed. There is no one single mechanism that explains all the hydrogen degradation phenomena and the overall process may include more than one of the mechanisms or all could contribute in some special

cases. It is also possible in some cases for one mechanism to dominate initially, but as conditions change, the dominant mechanism also changes. A brief explanation of the various prominent hydrogen embrittlement mechanisms proposed and developed over the past several decades is given here.

2.8.1 The Pressure Theory

The planar pressure theory is one of the earliest hydrogen embrittlement theories that was advanced by Zappfe and Sims in 1941 [19]. According to this theory, the hydrogen present in the material builds up a very high pressure at voids and other defects. This hydrogen pressure buildup aids in the fracture process. Although this theory was considered important to explain the blistering of steels in the presence of hydrogen, it cannot by itself explain hydrogen embrittlement in the case of high-strength steels where fracture occurs in steel in equilibrium with hydrogen at very low pressures. It is difficult to explain by this theory how significant internal pressure can be generated by hydrogen entering from a low external pressure.

2.8.2. Decohesion Theories

The hydrogen enhanced decohesion (HEDE) mechanism was first developed by Troiano et al. [20, 21] and further advanced by Oriani et al. [22]. According to this theory, the hydrogen dissolved in the metal lattice lowers the cohesive bonding strength of the metal or alloy, and results in fracture at a much lower stress than in the absence of hydrogen. The amount of hydrogen present in the metal lattice is generally very low, and so it is necessary for some method to exist by which the hydrogen can concentrate at the

fracture site. In case of fracture along a phase or grain boundary, the hydrogen concentration can occur due to hydrogen trapping at the second phase or at the grain boundaries. In case of transgranular cracking, the hydrogen concentration enhancement that occurs is attributed to the presence of triaxial stresses at the crack tip.

HEDE is considered as a dominant mechanism in the cases of internal hydrogen assisted cracking and hydrogen environment assisted cracking in high-strength alloys that do not form hydrides.

2.8.3 Surface Energy Theories

Surface energy theories were first proposed by Petch and Stables [23]. According to these theories, the hydrogen adsorbed at the crack tip and surface imperfections results in a reduction of surface energy. By lowering the surface energy of the newly formed cracks, the hydrogen reduces the stress intensity required for brittle fracture. Similar to the decohesion theory, the surface energy theory also seems reasonable only in the case of hydrogen derived from surface layers or grain boundaries. This is because hydrogen adsorption must occur at the same time as the fracture event in order for the reduction in surface energy to be effective in lowering the energy required for fracture.

2.8.4 Hydride Formation

The nucleation and growth of hydrogen-rich phases like the hydrides is the main cause of embrittlement in elements like Ti, V, Nb and Zr. This was first postulated by Gahr et al. [24] as a mechanism of hydrogen embrittlement in niobium. This stress-induced hydride formation and cleavage mechanism is one of the well-established

hydrogen embrittlement mechanisms with extensive experimental support [17]. Hydrides have mechanically different properties than the matrix, and so the crack nucleation and propagation occur preferentially along these brittle phases leading to embrittlement. It has been widely accepted that a hydride is not formed, or at least it is unstable, in the case of iron, carbon steels and low alloy steels. The absence of hydride formation can be attributed to the extremely low solubility of hydrogen in iron and steels unlike the case of hydride forming elements like Ti, V, Nb and Zr.

2.8.5 Localized Plasticity Theories

Various workers have suggested that hydrogen reduces the stress required for dislocation motion. The hydrogen enhanced localized plasticity (HELP) mechanism was first proposed by Beachem [25] and developed by Birnbaum et al. [26, 27]. This model explains softening in microscale caused by enhanced dislocation mobility in the presence of hydrogen. This is supported by enhanced dislocation motion with direct experimental observation of active in-situ experiments in a controlled-environment transmission electron microscope [17]. Presence of hydrogen in the lattice aids dislocation motion and locally reduces the flow stress, causing localized plastic deformation sufficient to result in subcritical crack growth with brittle characteristics on the macroscopic scale.

Of the various theories explained above, the decohesion theory appears to give a satisfactory explanation of the more common case of intergranular hydrogen embrittlement. Transgranular hydrogen embrittlement is difficult to explain with this theory because of relatively low hydrogen concentration of the matrix, but can be

supported by consideration of factors like hydrogen transport by dislocation and concentration of hydrogen at regions of high triaxial stresses.

2.9 Hydrogen Entry

Entry of hydrogen into the metal lattice is the first step in the hydrogen embrittlement process. The hydrogen entry is a complicated process and difficult to explain by a single mechanism or model. It depends on various material and experimental parameters. The form in which hydrogen diffuses into the lattice, i.e. whether in the form of monoatomic hydrogen, H^+ or H^-, is a point of discussion in literature.

Hydrogen can be introduced into metals and alloys in certain environments, and there are numerous ways for hydrogen to enter metals. Among these is electrolytic decomposition of hydrogen on metal electrodes. The electrolytic process is a very efficient way of introducing hydrogen since it can sustain a high equivalent pressure of hydrogen gas at the metal surface. The electrochemical evolution of atomic hydrogen takes place as a part of the cathodic reaction in an electrolytic cell. Before explaining the details of hydrogen evolution and entry in an aqueous electrolyte, a brief description of hydrogen entry from a gaseous phase is given.

2.9.1 Hydrogen Entry into Iron Alloys from a Gaseous Phase

The hydrogen entry into the metal lattice from a gaseous phase can be explained in terms of three major steps: physisorption, chemisorption and absorption [17]. This is shown in Figure 2.9. The first step is physisorption (Figure 2.9 (a)), which involves the physical adsorption of gaseous hydrogen (or other gases such as hydrogen sulfide) onto

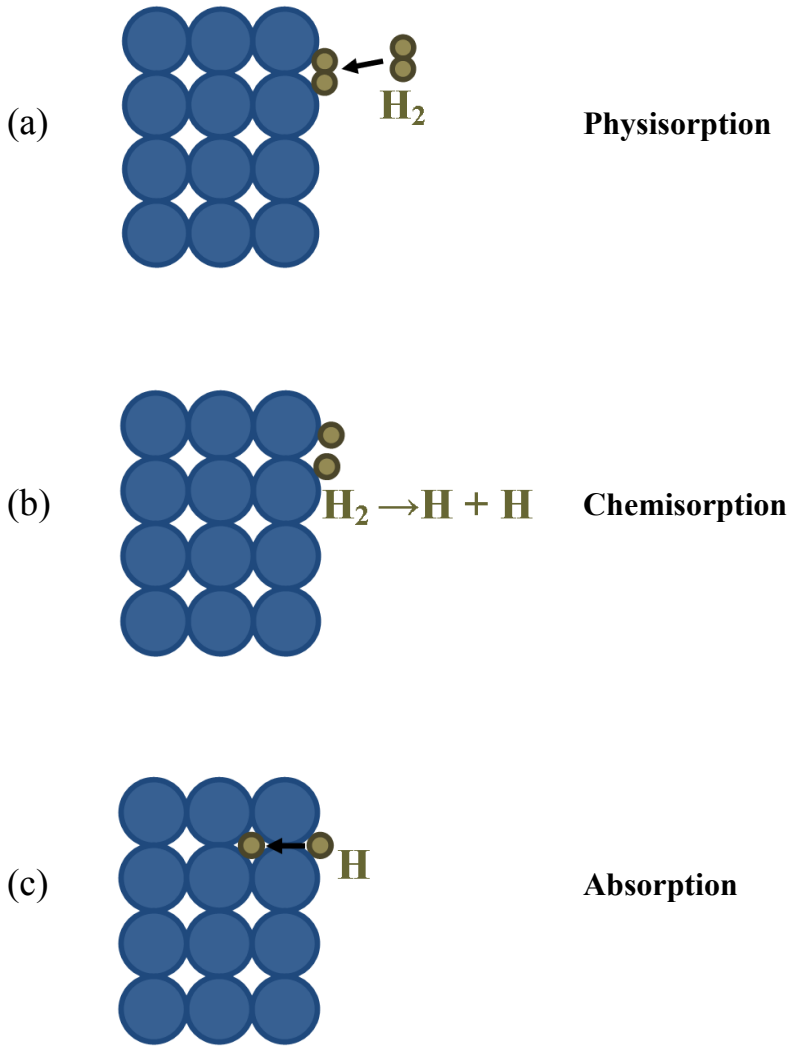

Figure 2.9 A schematic of hydrogen entry into metal lattice from a gaseous phase.

the surface and is the result of Van der Waals forces between the surface and the adsorbent. The next step is chemisorption (Figure 2.9 (b)), which involves the chemical reaction between the surface atoms and the adsorbed hydrogen molecule. During this step, molecular hydrogen dissociates to form hydrogen atoms. The final absorption step (Figure 2.9 (c)) involves the diffusion of the so-formed monoatomic hydrogen into the metal lattice.

2.9.2 Hydrogen Entry into Iron Alloys from a Liquid Phase

In most of the engineering applications, it is more feasible for the hydrogen to enter the metal lattice from an aqueous environment. A common way for the hydrogen to enter the metal lattice is through an electrolytic process, in which the hydrogen evolution and hydrogen absorption reactions occur at the cathode surface. The metal-electrolyte interface (Figure 2.10) is much more complicated than the metal-gas interface, due to the presence of a dense network of water dipoles in the electrolyte and due to competitive adsorption of various species on the metal surface [17]. This becomes even more complicated in the presence of a crack or pit where the conditions are localized, leading to inhomogeneous corrosion occurring at these regions and causing localized hydrogen evolution.

2.9.2.1 Mechanism of Cathodic Hydrogen Evolution from Aqueous Electrolytes

Depending upon the nature of the electrolyte, whether acidic or alkaline, the overall hydrogen evolution reaction (HER) can be written as:

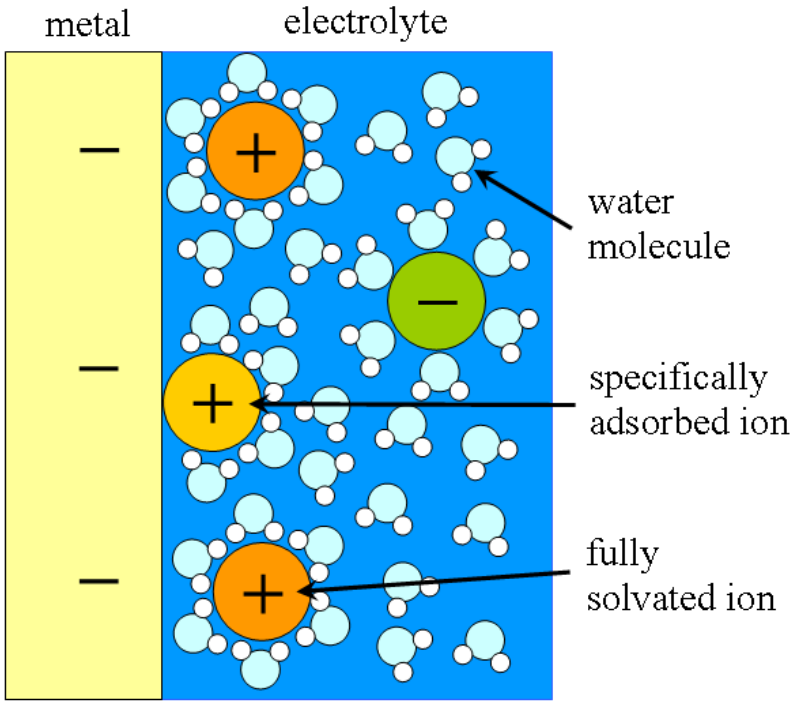

Figure 2.10 A schematic of a metal-electrolyte interface with water dipoles and ions adsorbed on the metal surface (adapted from reference [17]).

$$2H_3O^+ + 2e^- \rightarrow H_2 + 2H_2O \text{ (in acid solutions)} \quad (2.8)$$

$$2H_2O + 2e^- \rightarrow H_2 + OH^- \text{ (in alkaline solutions)} \quad (2.9)$$

These reactions are known to proceed in two successive steps [17]. The first step involves formation of monoatomic hydrogen which is adsorbed on the metal surface. This can either form by discharge of hydrated protons, as in the case of acid solutions:

$$H_3O^+ + M + e^- \rightarrow MH_{ads} + H_2O \quad (2.10)$$

or by electrolysis of water, as in the case of alkaline solutions:

$$H_2O + M + e^- \rightarrow MH_{ads} + OH^- \quad (2.11)$$

where, MH_{ads} represents hydrogen atoms adsorbed on the metal surface.

The next step in the HER is the formation of a hydrogen molecule (H_2) that evolves as hydrogen gas at the cathode surface. This reaction is dependant on the nature of the electrode metal and on the cathodic current density. Two of the monoatomic hydrogen atoms adsorbed on the metal surface can combine by chemical desorption (also called catalytic recombination) to form molecular hydrogen, which can occur in both acid and alkaline solutions:

$$MH_{ads} + MH_{ads} \rightarrow H_2 + 2M \quad (2.12)$$

or this can occur by electrochemical desorption, in which the adsorbed monoatomic hydrogen reacts with the hydrated proton in the electrolyte to form molecular hydrogen:

$$MH_{ads} + H_3O^+ + e^- \rightarrow H_2 + H_2O + M \text{ (in acid solutions)} \quad (2.13)$$

$$MH_{ads} + H_2O + e^- \rightarrow H_2 + OH^- + M \text{ (in alkaline solutions)} \quad (2.14)$$

2.9.2.2 Entry of Electrolytic Hydrogen into Metals

Most of the monoatomic hydrogen formed combines by chemical or electrochemical desorption to form gaseous hydrogen. A small portion of this monoatomic hydrogen enters the metal lattice. The rate of hydrogen absorption reaction (HAR) depends on a number of variables such as the nature of the metal or alloy, its composition and microstructure, surface conditions, electrolyte composition, charging current density, temperature, pressure, etc. The kinetics of hydrogen entry is studied by permeation of electrolytic hydrogen through a thin metal membrane, and a number of very sensitive electrochemical methods [59] have been developed to measure this precisely.

Two models of hydrogen absorption reaction are reported in the literature [60-62]. The first model proposed by Bockris et al. [60] suggests that the HAR is dependent on the HER. According to this mechanism, the adsorbed hydrogen gets absorbed into the metal lattice (Figure 2.11 (a)). Based on this model, the sequence of reactions occurring (in acid) at the cathode surface is given as:

(a)

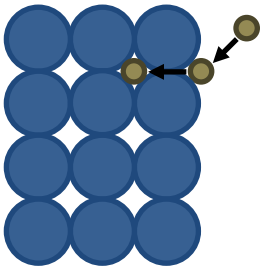

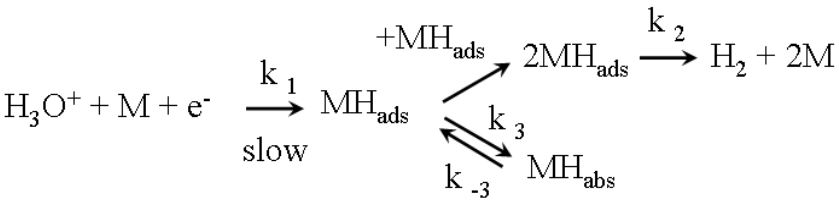

(b)

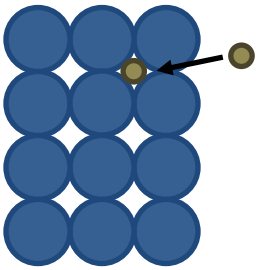

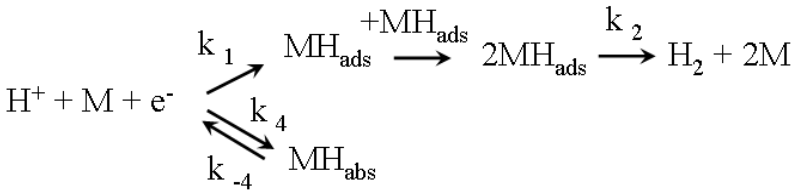

Figure 2.11 Models to explain hydrogen absorption reaction from an aqueous phase.

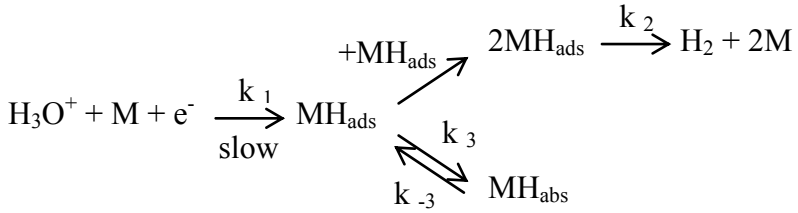

(2.15)

where, MH_{abs} refers to hydrogen atoms absorbed beneath the metal surface, and k_1, k_2, k_3, k_{-3} are rate constants of various steps. The permeation rate in this case should be proportional to the coverage of the metal surface by adsorbed hydrogen atoms [17].

The other model postulated by Bagotskaya [61] and Frumkin [62] suggests that the hydrogen entry into the metal occurs simultaneously during the hydrogen discharge reaction (Figure 2.11 (b)). In this model, HER and HAR occur independently. Based on this model, the sequence of reactions that occur at the cathode surface is given as:

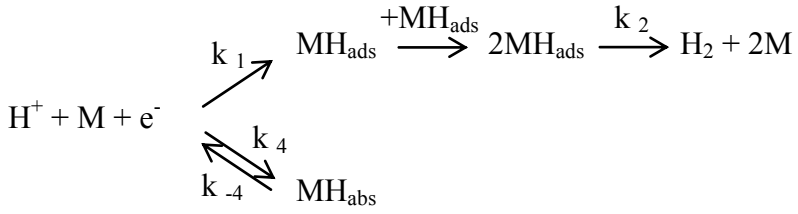

(2.16)

Hydrogen solubility in iron and iron-based alloys by the electrochemical process in an aqueous solution is proportional to the square root of current density [17].

2.9.3 Promoters of Hydrogen Entry into Metals

Certain compounds are known to promote hydrogen entry into metals from both liquid and gaseous environments [17]. They are termed hydrogen recombination poisons. Such compounds when present in the electrolyte hinder recombination of hydrogen, thus

preventing hydrogen gas evolution and promoting HAR. Some of the species found to promote hydrogen entry are:

i) Certain compounds of the following elements: phosphorus, arsenic, and antimony belonging to the V-A periodic group, and sulfur, selenium, and tellurium belonging to the VI-A periodic group

ii) The following anions: CN^- (cyanide), CNS^- (rhodanide), and I^- (iodide)

iii) The following compounds of carbon: CS_2 (carbon sulfide), CO (carbon monoxide), CON_2H_4 (urea), and CSN_2H_4 (thiourea)

These compounds show their full effect at relatively low concentrations, because at higher concentrations, they often lead to deposition of insoluble products that can inhibit hydrogen entry.

2.10 Hydrogen Diffusion in Iron

A number of studies to determine the diffusion of hydrogen in iron are reported [63-67]. A complete review of hydrogen diffusion in deformed and annealed iron is given by Kiuchi and McLellan [63]. The existing data of diffusivity exhibit a large scatter ranging over four orders of magnitude around the ambient temperature. In spite of experiments done on ultra-high-purity iron, the principal cause of these inconsistencies is the defect level present in the material used. Even the slightest change in defect concentration will affect the hydrogen trapping and thereby affect the diffusion measurements. Moreover, a quartz tube used for heat treatment can introduce silicon into the material, which can affect the hydrogen diffusion in iron. Similarly, other alloying elements present in iron, such as Cr and Mo, can significantly affect the diffusivity values

[64]. Diffusivity of hydrogen in iron and steels is reported by Radhakrishnan et al. [65] and Oriani [66], with an emphasis on metallurgical factors like grain size, cold work, annealing, microstructure and stress that affect the trapping of hydrogen. The room temperature (at 298 K) hydrogen diffusion coefficient values reported in the literature for pure iron (with very low dislocation densities) are in the range of 6.0×10^{-9} m^2/s to 8.0×10^{-9} m^2/s [17]. Typical values of diffusion coefficients of hydrogen in high-strength alloy steel at room temperature are on the order of 10^{-11} m^2/s [67].

2.11 Hydrogen Trapping in Iron

Hydrogen existing in monoatomic form, with an atomic size of about 1.06 A°, occupies an interstitial site in the BCC iron lattice. It can either occupy an octahedral or a tetrahedral site, as shown in Figure 2.12 [17].

The hydrogen homogenously present in the lattice at ambient temperature and pressure is only about 3 hydrogen atoms for every 10^8 atoms of iron [18], and this low content of hydrogen should not create a dangerous condition for embrittlement. However, it is extremely easy either to introduce significant concentration changes or large excess concentrations of hydrogen into the metals and these serve as the primary source for creating susceptibility towards embrittlement. It is possible in any common engineering or manufacturing processes, at higher temperatures or pressures, to introduce hydrogen in the metal lattice to a high concentration level. But if the material is returned to ambient conditions, the lattice is not capable of retaining the excess hydrogen in the super saturated solution.

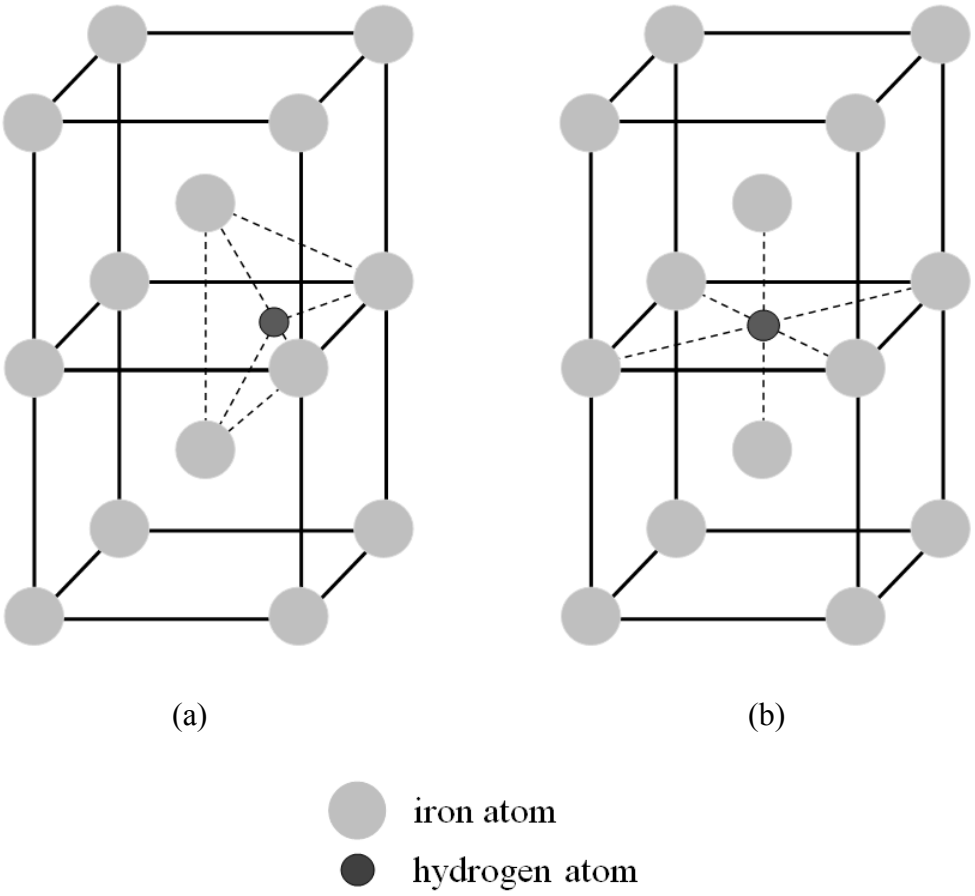

Figure 2.12 A schematic of hydrogen atom in interstitial site of BCC iron lattice: (a) tetrahedral site; (b) octahedral site.

To accommodate this excess hydrogen, there has to be sinks capable of absorbing large quantities of hydrogen. It has been proved experimentally that in addition to the interstitial sites in the lattice, hydrogen diffusing into a metal lattice interacts with lattice imperfections such as voids, dislocations, grain boundaries, solute atoms, second phase particles, nonmetallic inclusions, etc. Hydrogen interacts with the defects more strongly than they do with the lattice, resulting in localization of these diffusing species. Such sites inside the metals where localization of the diffusing hydrogen occurs are termed as hydrogen traps. The role of trapping in hydrogen transport in steels was reviewed by Oriani [66] in 1970. These traps can be classified into four types, as summarized in Table 2.3, based on the number of hydrogen atoms which can be accommodated in the trap and based on the binding energy of the trap [67].

It is important to understand this hydrogen interaction with such heterogeneities in the metal lattice, because these local interactions are responsible for the substeps to failure: crack initiation, growth and finally fracture. Therefore, controlling these microstructural parameters can help improve the hydrogen embrittlement resistance of materials.

2.12 Factors Affecting Hydrogen Embrittlement

2.12.1 Effect of Strain Rate

In contrast to other embrittlement phenomenon which has direct proportionality to strain rate, hydrogen embrittlement is inversely dependent on strain rate. The slower the strain rate, the more is the embrittlement. This behavior is explained by the planar

Table 2.3

Classification of hydrogen traps [67].

Classification	**Description**
Saturable	The number of sites for hydrogen atoms is fixed (e.g. boundaries, dislocations)
Nonsaturable	The number of sites for hydrogen atoms in the trap varies according to the fugacity (e.g. voids)
Reversible	The trap binding energy is relatively small, and hydrogen may escape from the trap as well as enter it
Irreversible	The trap binding energy is large, and hydrogen will not leave the trap at ambient temperature

pressure theory [19]. Upon straining, the voids enlarge and the hydrogen pressure in the voids drops. Further concentration buildup of hydrogen is necessary to maintain a damaging pressure. Therefore, if the rate of straining is more than the hydrogen pressure restoration, embrittlement should decrease [20]. Hydrogen embrittlement is diffusion controlled, and so at higher strain rates, there is insufficient time for appreciable hydrogen diffusion to the void or to the tip of a propagating crack.

2.12.2 Effect of Temperature

Hydrogen embrittlement effect disappears at low and high test temperatures. Similar to the effect of strain rate, according to the planar pressure theory, at lower temperatures, the rate of delivery of hydrogen to the voids decreases and that reduces the hydrogen embrittlement. At lower temperatures, the diffusion of hydrogen is also lower and that reduces hydrogen embrittlement. At higher temperature due to very high diffusivity, it is difficult to have sufficient hydrogen concentration gradient and the embrittlement decreases [20]. Therefore, the hydrogen embrittlement dominates near room temperature [18].

2.12.3 Effect of Stresses

It was experimentally shown by Kazinczy [68] that the hydrogen diffusion in steel increases in the presence of stresses, up to the yield point. This increase is attributed to the stress multiplication along slip planes in which the hydrogen flow is thereby increased. Therefore, the in-situ charging of hydrogen during the test increases the hydrogen diffusion into the sample.

2.12.4 Effect of Magnetic Field

Magnetization tends to affect the hydrogen embrittlement susceptibility of iron and iron-based alloys. It is reported that the presence of an applied magnetic field can decrease [29] or increase [30, 31] the hydrogen embrittlement susceptibility of a material. A strong applied magnetic field near saturation can affect the domain structure and therefore could change the interstitial-dislocation interaction, which affects the mechanical properties of the alloys [29, 30]. It has also been reported that the application of magnetic field near saturation affects the cathodic surface reactions, leading to enhanced hydrogen absorption and thereby increasing the susceptibility of steels to hydrogen-induced cracking [31, 32].

2.13 Reducing Hydrogen Embrittlement Susceptibility in Materials

There are two obvious ways to reduce the susceptibility of materials to hydrogen embrittlement: (i) either by controlling the hydrogen content in the material or (ii) by making the material more resistant to hydrogen embrittlement.

The presence of hydrogen or entry of hydrogen into the material in some applications is unavoidable. Hydrogen that preexists in the material or is introduced during processing steps can be reduced by a suitable de-embrittlement treatment. However, the most difficult problem is to avoid entry of hydrogen during service. This can be controlled by the use of appropriate inhibitors which will react with the hydrogen, accelerate hydrogen recombination reaction or cover the surface to block the active surface site for hydrogen absorption. Organic coatings make it difficult to achieve this as they are prone to damage or are permeable to hydrogen. Suitable metal coatings can offer

some reduction in hydrogen entry, as closed packed metals have a lower hydrogen diffusion coefficient than for iron.

The second way to reduce hydrogen embrittlement susceptibility is by making the material more resistant to hydrogen embrittlement. Most of the hydrogen embrittlement mechanisms are based on hydrogen interaction with defects. Therefore, controlling the defect structure in materials can help control the hydrogen embrittlement, which is achieved by thermal treatments that reduce the internal residual stress, dislocation density and segregation. This is the reason for cold worked material with higher dislocation density or fine grained material with more grain boundary area being more susceptible to hydrogen embrittlement than the annealed materials with larger grain sizes. Materials with more closed packed structure (like FCC compared to BCC) are less prone to hydrogen embrittlement. Suitable material design can only help reduce the susceptibility of materials to hydrogen embrittlement, but cannot completely eliminate it.

2.14 Acoustic Emission Measurements

When a solid is subjected to stress at certain levels, discrete acoustic wave packets are generated which can be detected by transducers placed on, or in acoustic contact with, the solid. The phenomenon of sound generation in materials under stress is termed acoustic emission (AE) or alternatively, stress wave emission [33].

A remarkable phenomenon of AE was observed and reported by Josef Keiser [34] and is widely accepted and referred to in AE literature. He observed that when a material is stressed, acoustic emissions are detected. This material unloaded to relax the stresses and reloaded again has no new emissions detected until the previous maximum stress has

been exceeded. This effect is termed as the Kaiser effect [69]. However, the Kaiser effect does not always occur. In some cases, emission does occur upon unloading at a specific fraction of the previous maximum load, known initially as the Modified Kaiser effect, but now is usually referred to as the Felicity effect [69]. The ratio of load at which emissions reoccur to the previous maximum load is expressed as Felicity ratio or Felicity percentage.

2.14.1 Acoustic Emission as a Nondestructive Evaluation Technique

AE has developed rapidly over the last couple of decades as a nondestructive evaluation technique and as a tool for materials research. It is a high sensitivity technique for detecting active microscopic events in a material. The atomic rearrangements which occur within a material during deformation and cracking produce elastic waves which travel through the material and can be detected at a surface by piezoelectric transducers. The transducer signals can be used to detect deformations or crack formation and propagation in a material; this has practical applications in the nondestructive testing of structures and components [35, 36]. It is possible, in principle, to obtain information about the nature and the severity of changes occurring at defects in structures under load; additionally, three or more transducers can be used to locate the position of the deformation within the structure or component.

A basic AE measurement setup comprises a transducer in acoustic contact with the material or the structure under test, a low noise signal cable connected to the electronic signal conditioner, and a computer-controlled data acquisition system for counting and recording the AE signals.

2.14.2 Acoustic Emission Technique in Deformation and Fracture Studies

All common structural materials (metallic alloys, glasses, polymers, ceramics and composites) exhibit AE. The intensity and frequency spectra of the elastic waves coming from the defect depend on the material, the nature of the deformation process, the local stresses at the defect and often on the environment in which the material is placed. AE techniques can be used to study deformation processes and fracture studies in a variety of materials and environments [37, 38].

In polycrystalline materials, the main source of hydrogen embrittlement is from the microscopic intergranular fracture. The cumulative AE event counts are proportional to the number of intergranular microcracks during stable crack growth [39, 70]; hence there is a correlation between AE activity and the embrittlement process. It has been reported that the level of acoustic emission is higher in the case of intergranular cracking than in the case of transgranular cracking, and this is attributed to the larger size increment that occurs during intergranular cracking during discontinuous crack propagation [40]. Similarly, a larger grain size increases the amount of AE because of the larger crack increments.

In most cases, there is a long time gap between the incubation and final fracture. Therefore, monitoring the incubation time to nucleate microcracks in terms of some directly observable AE analysis can be applied to detect failure mechanisms of hydrogen charged specimens under mechanical loading and these parameters can be of great help in protecting the structure from premature hydrogen embrittlement failures [71].

2.14.3 Advantages and Limitations of Acoustic Emission Technique

There are inherent advantages and limitations to the AE technique. The most important advantage of using this technique for nondestructive testing (NDT) is that it is essentially nonlocalized. The transducer used for detecting needs to be in acoustic contact with the structure and need not be near the emission source. It is very easy to scan a large structure using acoustic emission probes placed at 1-10 m intervals on the surface of the structure. This is advantageous in comparison to other nondestructive testing methods like radiography, ultrasonic inspection or eddy current inspection which require the probe to scan over the entire structure. It is also useful in cases where the defect location is physically inaccessible for inspection purposes. The other major advantage of AE as a NDT tool is its ability for continuous in-service monitoring of structures. The AE technique has its own limitations. The acoustic emission signals intensities in some cases are too low to be detected with conventional piezoelectric transducers, which then require sophisticated and expensive transducers. The main difficulty is associated with the background noise which is frequently present during in-service tests of structures. Care has to be taken to reduce interference from noise generated in pumps, waves or moving machinery [33].

CHAPTER 3

RESEARCH OBJECTIVES AND EXPERIMENTAL APPROACH

The main objectives of this research work were to examine the effect of hydrogen and magnetic field on the mechanical behavior of magnetostrictive Fe-Ga alloys. Fe-17.5 at.% Ga alloy was selected. The reason for selecting this composition is because this composition has a single phase (α phase – A2 structure) in the temperature range of 450 to 1425 °C and on cooling has a much smaller tendency to form ordered second phase regions (such as $L1_2$ or DO3 or B2 structures which have been identified to form in alloys with higher Ga contents, such as in Fe-27.5 at.% Ga). While the maximum magnetostriction observed in the Fe-Ga alloy system is at a Ga content of about 20 at.%, a slightly lower Ga content alloy was chosen so as to obtain a single phase alloy on reasonably fast cooling such as by air and at the same time obtain large magnetostriction values.

In order to avoid the effects of the grain boundaries and other defects that are present in polycrystalline materials, it was decided to use samples for the test made completely of a single crystal. Mechanical test results of single crystal samples reported in the literature are mostly done by using samples, as shown in Figure 3.1 (a), having only the test region made of single crystal. Even with careful control of the processing parameters, this can introduce errors in results due to the metal joining process used in

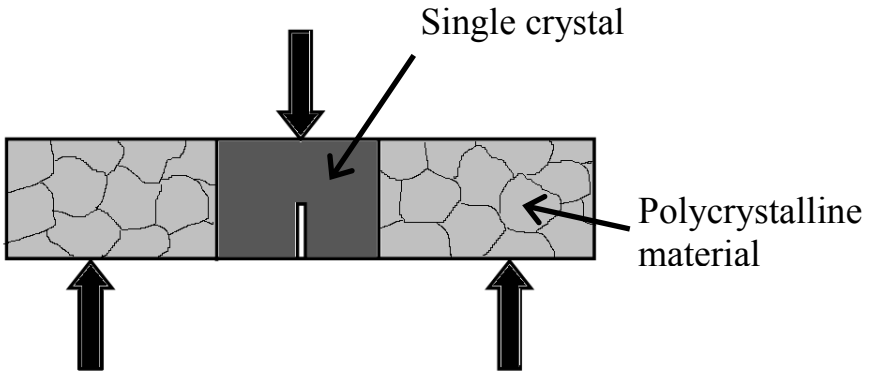

(a)

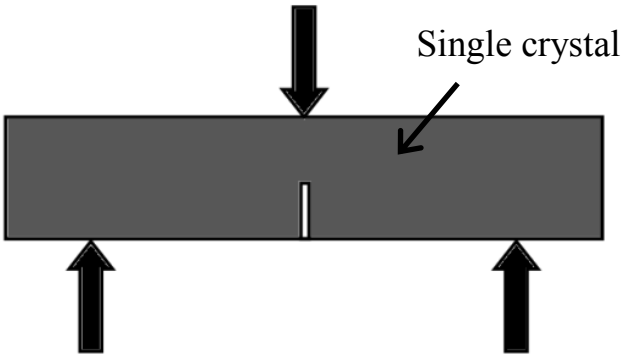

(b)

Figure 3.1 A schematic of samples used for three-point bend test (a) with only the test region made of single crystal; (b) entire sample made of single crystal.

joining the single crystal with the other base metal. Therefore, the test results from samples made completely with a single crystal (Figure 3.1 (b)) are more reliable and significant. But, the preparation of such single crystal samples of the desired orientation, large enough to make multiple identical test samples, involves meticulous care in the single crystal growth process and a number of laborious iterations of crystal orientation and polishing steps. Therefore, the first challenging step in this work was in growing a large enough Fe-17.5 at.% Ga single crystal, using the vertical Bridgman technique, to get four identical samples with desired orientation and dimensions. Faces of the single crystals samples used for the tests were kept close to (100) orientation.

Three-point bend tests and tensile tests were used to study the fracture behavior of these alloys. Due to the difficulty in obtaining single crystals of reasonable size, only the three-point bend tests were carried out on single crystal samples, and the tensile tests were carried out on polycrystalline magnetostrictive Fe-15 at.% Ga alloys. In order to optimize the three-point bend testing procedures and parameters, high-strength AISI 4340 steel, a material that is well examined for its hydrogen embrittlement susceptibility, was used.

To systematically study the effect of hydrogen and magnetic field on the fracture behavior of these alloys, the tests were designed to be carried out under different test conditions: (i) with neither hydrogen charging nor magnetic field, (ii) with hydrogen charging only, (iii) with hydrogen and magnetic field and (iv) with magnetic field only. Hydrogen was introduced in the samples by in-situ electrochemical charging in specially designed electrolytic cells. In-situ hydrogen charging was done before and during the test. The precharging time was selected from the literature based on the hydrogen fugacity and

diffusion in iron during electrochemical hydrogen charging. The hydrogen charging current density was determined from potentiodynamic polarization scan results.

The magnetic field was applied either using $Nd_2Fe_{14}B$ permanent magnets attached to the ends of the sample (for three-point bend tests) or by using a solenoid coil (for tensile tests). In the case of three-point bend tests, in order to study the effect of direction of applied magnetic field, the magnetic field was applied either along the length axis or width axis of the sample. Acoustic emission signals were collected continuously during the entire test period. For this purpose, a high performance acoustic emission sensor was connected to the test setup, and the signal from the sensor was collected using a National Instruments data acquisition board and Labview® software. The acoustic emission signal at the initiation of fracture was also collected using a NICOLET® 310 oscilloscope with a maximum sample rate of one sample per μs. Acoustic emission results were correlated with the fracture test results to understand the fracture behavior. The fracture surfaces of tensile and bend tested samples were examined using a scanning electron microscope (SEM).

Transmission electron microscopy (TEM) was used to examine the α-phase of Fe-17.5 at.% Ga alloy, for which TEM samples were prepared from the single crystal sample that was used for the three-point bend test. Magnetic measurements were done on the Fe-17.5 at.% Ga alloy sample using a vibrating sample magnetometer (VSM) to determine the saturation magnetization value for the alloy. Magnetostriction measurements were done on the [001]-oriented Fe-17.5 at.% Ga alloy single crystal sample used for the three-point bend test in ambient condition, to determine the magnetostriction coefficient $(3/2)\lambda_{100}$.

CHAPTER 4

EXPERIMENTAL PROCEDURES

4.1 Alloy Preparation

The Fe-17.5 at.% Ga alloy single crystals used for the three-point bend tests were prepared using high vacuum arc melting, followed by single crystal growth using the vertical seedless Bridgman technique. Fe-15 at.% Ga polycrystalline alloy with preferential [001] texture for tensile tests was prepared using high vacuum arc melting, followed by thermomechanical processing.

4.1.1 Vacuum Arc Melting

Ingots of Fe-17.5 at.% Ga and Fe-15 at.% Ga alloys were prepared from high-purity (99.99%) elements (Fe and Ga) by vacuum arc melting technique in an Edmund Buehler® high vacuum arc melting system. Fe and Ga were weighed out as per stoichiometry and placed in the chamber. The chamber was evacuated to a vacuum level of $<10^{-4}$ torr (10^{-7} atm) and back-filled with ultra-high-purity (UHP) argon to about 0.7 atmosphere. Before arc melting the actual alloy, a piece of titanium was melted to getter any residual oxygen and moisture in the chamber. The alloys were then melted by using a low-power arc in the initial stages, followed by a gradual increase in power to assure complete melting. Due to higher vapor pressure of Ga relative to Fe, careful melting

procedures were adopted to assure negligible loss of Ga. Each ingot typically weighed about 20 grams and each ingot was remelted four times to assure alloy homogeneity.

4.1.2 Directional Casting

The arc melted ingots were then directionally cast using a setup as shown in Figure 4.1. Each of these arc melted alloy ingots were melted on top of a copper block placed on a water-cooled copper surface. When the ingot melted completely, the liquid metal was allowed to flow into a cylindrical cavity of the copper block with an alumina insulation sleeve to form a 9.4 mm diameter cylindrical rod. On contact of the liquid metal with the water-cooled copper surface, the solidification process occurs primarily by rapid-one-dimensional heat extraction in the downward direction through the water-cooled copper block surface. The directional casting was intended to promote a preferred crystallographic orientation in the ingot. These alloys are hereafter referred to as directional cast alloys.

4.1.3 Single Crystal Growth Process

Seedless vertical Bridgman technique, which has a better control of the temperature gradient across the liquid/solid interface, was used to grow single crystals. The crucible containing a liquid metal is moved away from the melting zone down the temperature gradient in the furnace using a stepper motor-controlled drive system. Through a proper control of temperature gradient in the furnace and the rate of movement of the crucible, single crystals of the alloys can be obtained. Figure 4.2 shows a schematic of the vertical Bridgman technique that was used for single crystal growth.

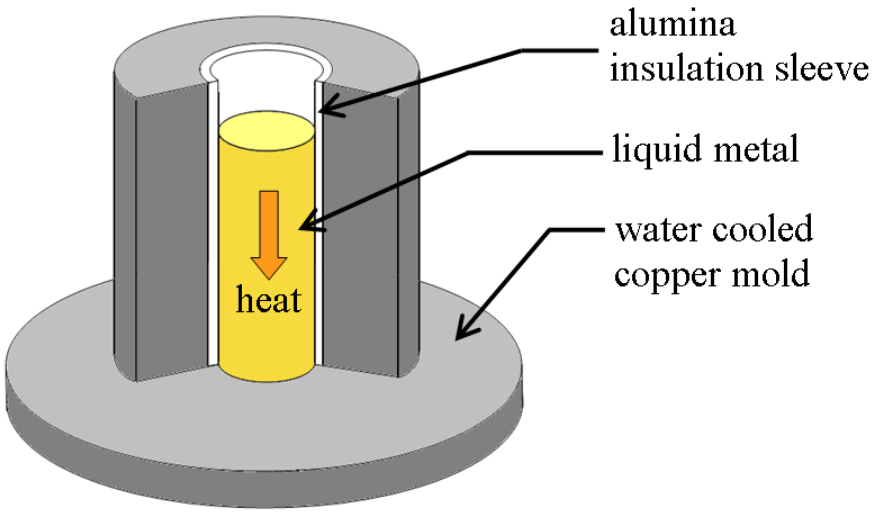

Figure 4.1 A schematic of the directional casting setup.

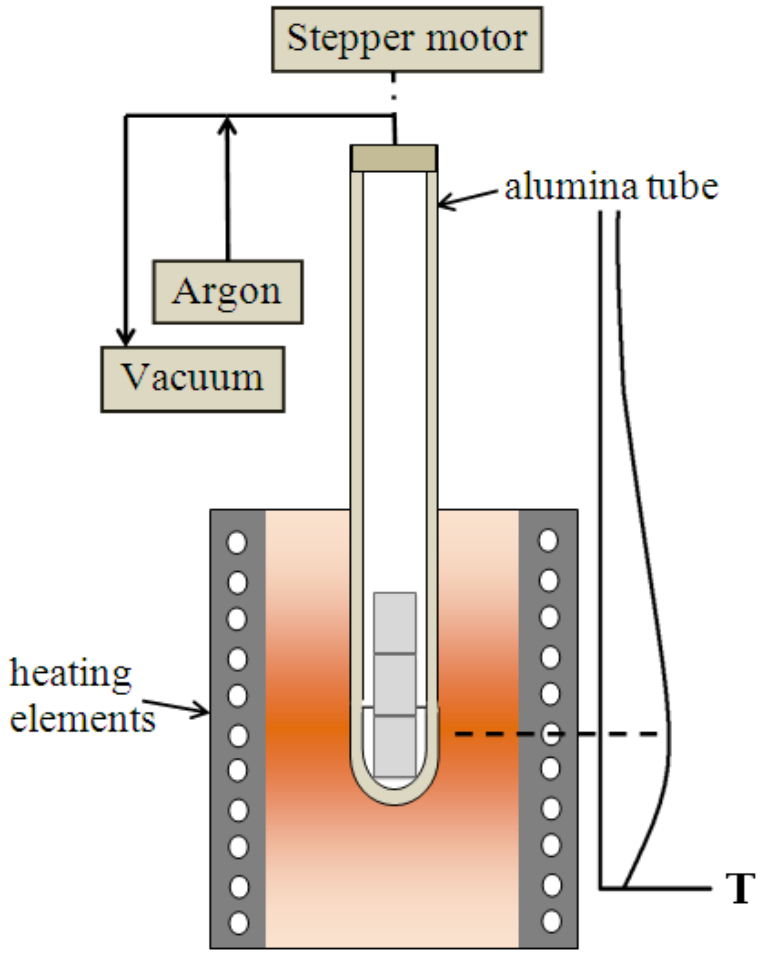

Figure 4.2 A schematic of the vertical Bridgman crystal growth set up used for growing Fe-17.5 at.% Ga alloy single crystal.

Several of the directional cast alloy rods were placed in a long closed-one-end alumina tube with inner diameter of about 12.5 mm. The tube was positioned in a two zone resistance heated furnace, and the sample position was set at the maximum temperature region. The alumina tube was evacuated and flushed with ultra-high-purity (UHP) argon several times. Small argon gas flow was maintained during the heating of the tube to a set-maximum temperature of 1530 °C, allowing the alloy rods to melt. After ensuring the completion of the melting process, the tube was lowered at a controlled rate of about 4 mm/hr down the furnace using a Velmex® stepper motor-drive mechanism. As the tube moved down the maximum temperature region, solidification of the melt started from the bottom end of the tube. A cylindrical single crystal, 72 mm in length and 12.5 mm in diameter, was cut from this directionally grown (DG) alloy rod. This single crystal was oriented and cut to get samples for the three-point bend test.

4.1.4 Thermomechanical Processing

Polycrystalline (Fe-15 $Ga)_{99}(NbC)_1$ alloy rolled strips prepared for an earlier study on texture development were used for examining the effect of hydrogen and magnetic field on the tensile behavior. The thermomechanical process used for preparing this rolled sheet sample is described below. Vacuum arc melted ingots of Fe-15 at.% Ga alloy with 1 volume % NbC addition were melted together to prepare a 25 mm x 25 mm x 75 mm block of (Fe-15 $Ga)_{99}(NbC)_1$ alloy. This arc melted and cast alloy ingot was homogenized at 1200 °C, hot rolled at 1100 °C, given a two stage warm rolling at 400°C with a reduction of about 66% in each stage, with an intermediate anneal at 900 °C for 1 h, and annealed at 700 °C for 2 h.

4.2 Single Crystal Orientation

X-ray diffraction examination of the single crystal cut from the DG alloy rod was performed using the Cu Kα radiation in a Siemens® D5000 high-resolution x-ray diffractometer. The $2\theta_{hkl}$ of various peaks for the alloy were obtained from a θ-2θ scan. These $2\theta_{hkl}$ values were used to perform rocking curve scans, in which the x-ray detector is fixed at a position corresponding to the 2θ value expected for a given (h k l) diffraction ((200) in this work) and the sample is rotated about the diffraction axis. Rocking curves along with detector and phi scans were used for crystal orientation determination. The maximum value in the rocking curve is the ω value corresponding to the optimal specimen orientation for diffraction from the (200) plane, and provides the amount of crystal misorientation from the [100] direction. This misorientation information was used to cut and polish the single crystal sample for three-point bend tests. The preparation of a single crystal sample to the desired orientation on all its six faces involves a number of laborious iterations of crystal orientation and polishing steps. It was also challenging to have a well-oriented single crystal large enough to make the entire set of bend test samples using that single crystal. For the three-point bend test, single crystal samples with edges close to <100> orientation were desired.

4.3 Three-Point Bend Test

A three-point bend test was used to study the fracture behavior of Fe-17.5 at.% Ga single crystal samples in the presence of hydrogen and magnetic field. The tests were designed to be carried out in four different test conditions: (i) with neither hydrogen charging nor magnetic field; (ii) with only hydrogen charging; (iii) with hydrogen

charging and magnetic field applied along the sample length axis; (iv) with hydrogen charging and magnetic field applied along the sample width axis.

Because of the difficulty in obtaining the single crystal samples, it is important to optimize the test setup and parameters before doing tests on the single crystal samples. For this, high-strength AISI 4340 steel was decided to be used. A high-strength alloy like the AISI 4340 steel is highly susceptible to hydrogen embrittlement and so is widely used for hydrogen embrittlement studies. The AISI 4340 steel used in this work was obtained in a cold drawn, normalized and subcritical annealed condition. The chemical composition as provided by the supplier is given in Table 4.1.

Three-point bend tests were carried out using a three-point bend test fixture on an Instron® 4505 universal testing machine. Crosshead speed of 0.1 mm/min was used conforming to slow strain rate testing to evaluate the susceptibility of metallic materials to environmentally assisted cracking (ASTM G129 – 00 Standard) [72]. Sampling rate of 1 pt/s was used for data collection during the test. The fracture surfaces of samples tested under different conditions were examined using a FEI Nova™ scanning electron microscope and some of the samples were examined using a TOPCON® scanning electron microscope SM-300.

4.3.1 Bend Test Sample Preparation

Samples of Fe-17.5 at.% Ga single crystal and AISI 4340 steel for the three-point bend test (Figure 4.3 (a)) were prepared with dimensions having length: thickness: width (L: D: W) ratio close to 8:2:1 conforming to ASTM E399 – 09 standard [73]. The length was made a little longer to have enough length on either side of the three-point bend

Table 4.1

Chemical composition of AISI 4340 steel used in this work (as provided by the supplier).

Element	**C**	**Mn**	**P**	**S**	**Si**	**Cr**	**Ni**	**Mo**	**Al**	**Cu**
Percentage	0.42	0.76	0.008	0.004	0.26	0.81	1.82	0.27	0.026	0.18

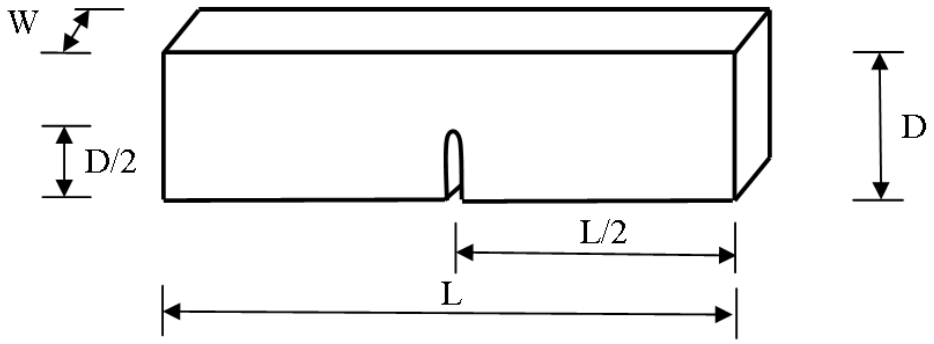

(a)

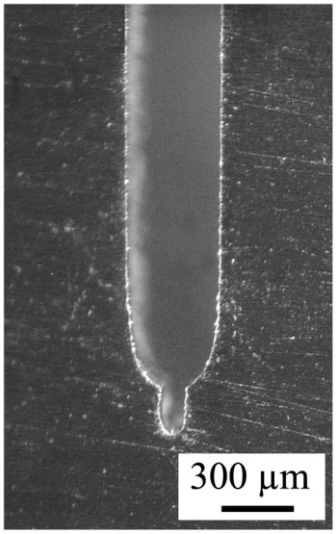

(b)

Figure 4.3 Three-point bend test sample: (a) a schematic of the sample dimensions; (b) optical microscope image of the notch tip.

fixture to avoid sample slip during bending. The notch was cut at the centre of the length (L) along the width (W) direction, with a total notch depth close to half the sample thickness (D). The notch was cut using a Buehler Isomet® low speed saw with a 300 μm thick diamond blade. The notch tip (Figure.4.3 (b)) was made sharper by polishing with a steel wire having a diameter of about 80 μm. The notch profile was made identical in all the samples. Sample surfaces were mechanically polished to 1200 grit finish.

4.3.2 Three-Point Bend Test Setup

A schematic of the test setup for in-situ hydrogen charging and magnetic field applied to the sample during the three-point bend test is shown in Figure 4.4. Cathodic charging of hydrogen was done electrolytically in a specially designed electrochemical cell which was attached to the three-point bend test fixture. Aqueous solution of 1 N sulfuric acid (H_2SO_4) with 1 g/L thiourea (hydrogen recombination poison) was used as the electrolyte. Platinum foil was used as the anode, and the test sample was used as the cathode. Hydrogen was precharged for 3 h before the bend test, followed by in-situ charging during the test. The hydrogen precharging time was selected based on the assumption that hydrogen diffusion rate is the same as that in pure iron. The optimum hydrogen charging current density for a Fe-17.5 at.% Ga single crystal sample and AISI 4340 steel sample were obtained from the potentiodynamic polarization scan prior to the three-point bend test. The potentiodynamic polarization scan was done using a three-electrode method, with a saturated calomel reference electrode and platinum counter electrode, in an electrolyte of 1 N H_2SO_4 with 1 g/L thiourea.

The magnetic field was applied to the bend test sample using $Nd_2Fe_{14}B$ permanent

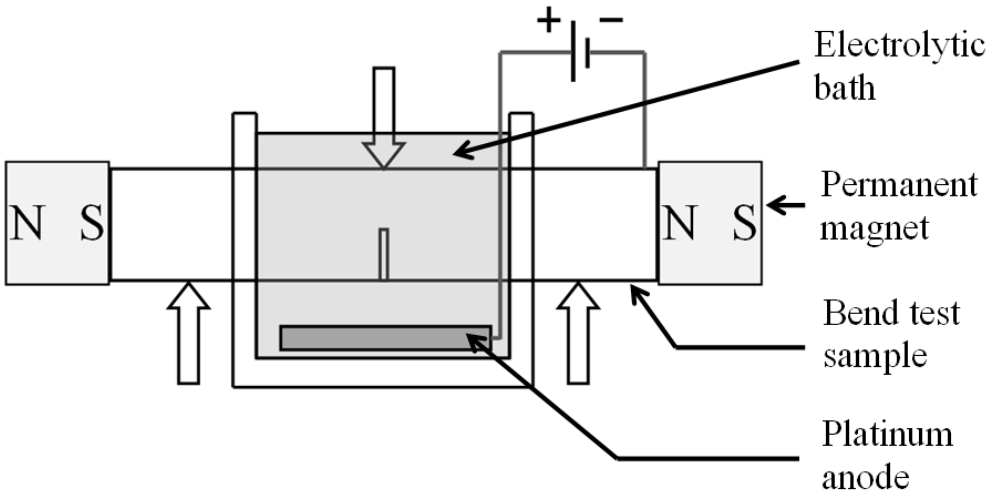

Figure 4.4 A schematic of the test setup for in-situ hydrogen charging and magnetic field applied to the sample during the three-point bend test.

magnets attached to the sample. To study the effect of direction of applied magnetic field, two configurations as shown in Figure 4.5 were used. The magnetic field was applied either along the length axis (Figure 4.5 (a)) or along the width axis (Figure 4.5 (b)) of the bend test sample. The magnetic field applied in such a configuration gives an almost homogenous magnetic field near the notch region with a field strength well over the saturation field value for these alloys.

4.4 Tensile Test

Tensile tests on Fe-15 at.% Ga polycrystalline samples were carried out in four different conditions: (i) annealed sample with neither hydrogen charging nor magnetic field, (ii) annealed sample with only hydrogen charging, (iii) as-rolled sample with only hydrogen charging, and (iv) annealed sample with hydrogen charging and magnetic field.

Tensile tests were carried out using an Instron® 4505 universal testing machine. A crosshead speed of 1 mm/m and a sampling rate of 10 pts/s were used for data collection during the test. The fracture surfaces of samples tested under different conditions were examined using a FEI Nova™ scanning electron microscope.

4.4.1 Tensile Sample Preparation

Tensile samples of dimensions as shown in Figure 4.6 were machined from the thermomechanically processed as-rolled $(Fe\text{-}15Ga)_{99}(NbC)_1$ alloy. Some of the samples were vacuum glass sealed in quartz vials and annealed at 720 ºC for 1 h. The sample surfaces were mechanically polished to 1200 grit finish. Tensile tests were carried out using as-rolled and annealed samples.

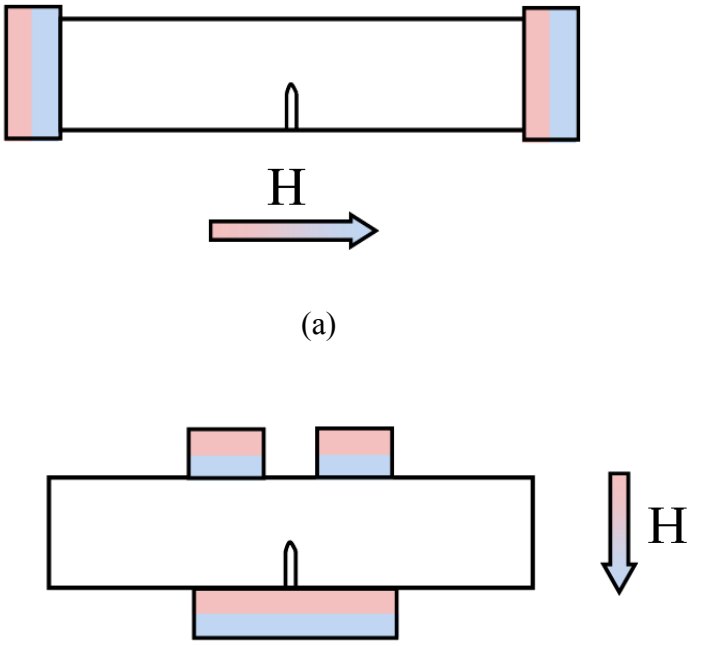

Figure 4.5 A schematic showing the magnetic field application configurations in the bend test sample: (a) along the length axis; (b) along the width axis.

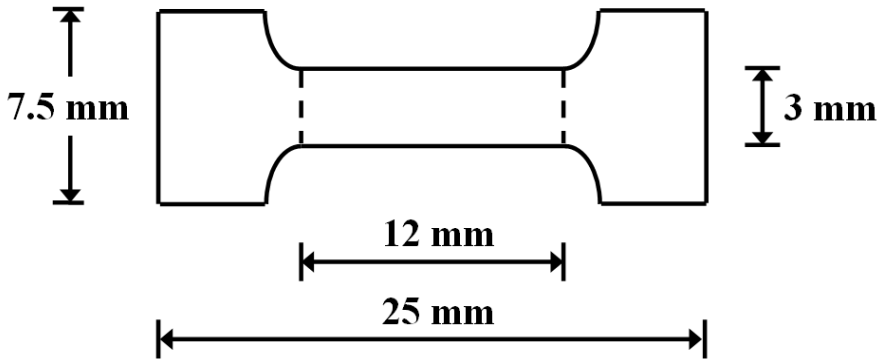

Figure 4.6 A schematic of tensile test sample dimensions.

4.4.2 Tensile Test Setup

A schematic diagram of the test setup for in-situ hydrogen charging and application of magnetic field during the tensile test is shown in Figure 4.7. Cathodic charging of hydrogen was done electrolytically in a specially designed in-situ electrochemical cell. Aqueous solution of 0.1 N H_2SO_4 was used as the electrolyte. Platinum foil was used as the anode and the Fe-15 at.% Ga tensile sample as the cathode. A current density of 50 A/m^2 was chosen to be used for hydrogen charging. Hydrogen was precharged for 30 minutes prior to the test, followed by in-situ charging during the tensile test. The magnetic field was applied to the tensile sample using a solenoid coil placed around the gauge length of the tensile sample. The magnetic field strength at the core of the solenoid was measured to be about 100 A/m.

4.5 Acoustic Emission Measurements

Acoustic emission signals were collected using a SE150M high performance acoustic emission sensor. The sensor was clamped to the three-point bend test fixture. Lubricant was used between the sensor and the fixture to avoid forming an air gap, thereby reducing the noise. The signal from the sensor was collected using a National Instruments data acquisition board and Labview® software, with a resolution of one data point per 50 μs. The signal was collected continuously from the beginning to the end of the bend test. The signal was also collected on a high resolution oscilloscope – Nicolet 310, with a resolution of one data point per μs.

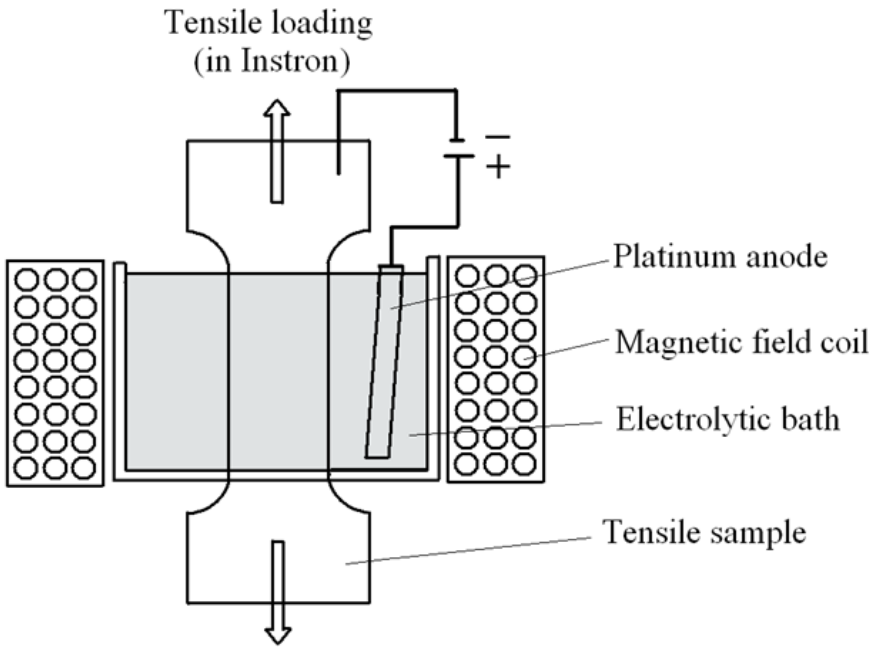

Figure 4.7 A schematic of the test setup for in-situ hydrogen charging and magnetic field applied to the sample during the tensile test.

4.6 Magnetic Hysteresis Measurement

Saturation magnetization measurements for Fe-17.5 at.% Ga alloy were made using a Lakeshore® 7307 vibrating sample magnetometer (VSM) with a Lakeshore® Model 450 gauss meter with ± 30 kG Hall probe. The Fe-17.5 at.% Ga alloy sample used for the measurement was cut from the as-cast ingot, having a cubic shape of approximately 2 x 2 x 2 mm^3. Measurements were carried out at room temperature.

4.7 Magnetostriction Measurements

The magnetostriction coefficient $(3/2)\lambda_{100}$ measurements of Fe-17.5 at.% Ga alloy single crystal were made on the same [001]-oriented single crystal sample cut from one end of the three-point bend test sample tested at room temperature. A full bridge technique was used with an active strain gage attached to the sample and three dummy gages attached to a Bi rod, which has a coefficient of thermal expansion similar to Fe. A schematic of the magnetostriction measurement setup is shown in Figure 4.8 (a). The strain gage was attached to the sample parallel to the [001] direction on a 12.5 mm x 6 mm face. The sample along with an attached strain gage was placed in between two iron end rods and a small dead weight was applied. The magnetic field was applied using a field coil surrounding the sample. Magnetostrictive strain was measured by applying the magnetic field (i) parallel to the [001] direction (Figure 4.8 (b)) and (ii) parallel to the [010] direction (Figure 4.8 (c)). Signals corresponding to the applied magnetic field and the magnetostriction were collected using an IOTECH® ADC 488/16A analog-digital convertor and an IOTECH® MUX 488/16SC signal conditioning multiplexer unit. Labview® software was used for the data acquisition.

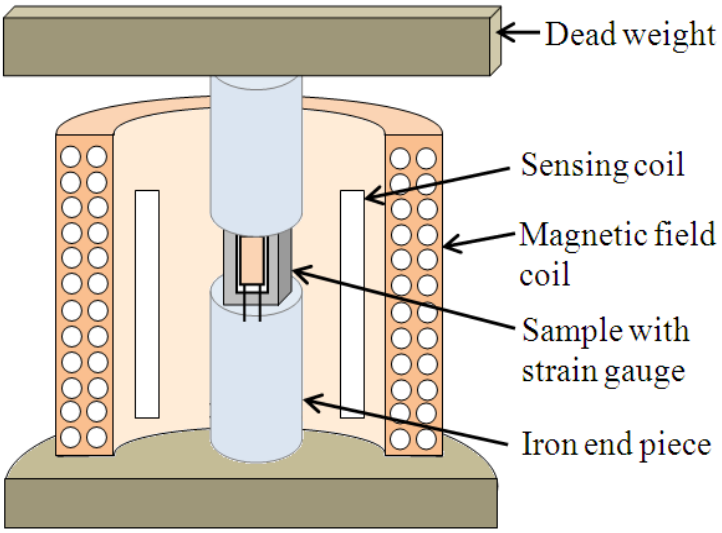

(a)

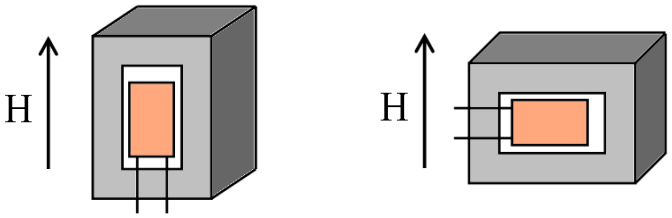

(b) (c)

Figure 4.8 Magnetostriction measurement: (a) a schematic of the measurement setup; (b) parallel measurement and (c) perpendicular measurement.

4.8 Transmission Electron Microscopy

Transmission electron microscopy (TEM) was used to examine the phases present in the Fe-17.5 at.% Ga alloy single crystal. TEM sample preparation involved cutting a slice of about 400 μm thick from the [001]-oriented Fe-17.5 at.% Ga single crystal sample. The 400 μm thick cut slice was polished in a number of steps starting from 600 and 1200 grid SiC polishing paper, followed by 3, 1 and 0.3 μm diamond polishing compound, down to a final thickness of about 100 μm thick. This 100 μm thick slice was used to cut 3 mm diameter discs using a precision drill. The 3 mm discs were electropolished in a Struers twin jet electropolisher using an electrolyte consisting of perchloric acid, ethylene glycol monobutyl ether, ethanol and water to obtain samples with electron transparent regions for TEM examination. Before the TEM examination, the transparency of the sample was checked in a FEI Nova™ SEM using the STEM mode. TECNAI F20s TEM in the Electron Microscopy Center User Facility at the Argonne National Laboratory was used for TEM examination.

CHAPTER 5

RESULTS AND DISCUSSION

In this section, the results of the single crystal orientation, magnetic hysteresis and magnetostriction measurements of the Fe-17.5 at.% Ga alloy single crystal are first presented. Then, the results of Fe-17.5 at.% Ga alloy single crystal TEM examination and potentiodynamic polarization scan results are presented. Following this, the results from the three-point bend tests on AISI 4340 steel and Fe-17.5 at.% Ga alloy single crystal samples and tensile tests of polycrystalline Fe-15 at.% Ga alloy are presented.

5.1 Single Crystal Characterization Using X-Ray Diffraction

Figure 5.1 shows the θ-2θ scan of the face cut normal to the length axis from the as-grown Fe-17.5 at.% Ga alloy single crystal. Peaks corresponding to various crystallographic planes are given. The single crystal nature of the as-grown Fe-17.5 at.% Ga alloy DG rod was confirmed using x-ray diffraction rocking curves corresponding to (200), (220) and (310) reflections and the rotation of the sample about the phi and theta axis. The long axis of the as-grown crystal was determined to be about 13 degrees away from the [100] direction. Using the crystal misorientation information obtained from the rocking curve along with phi and detector scans, the crystal was oriented close to [100] orientation. Figure 5.2 shows the rocking curve corresponding to (200) reflection from

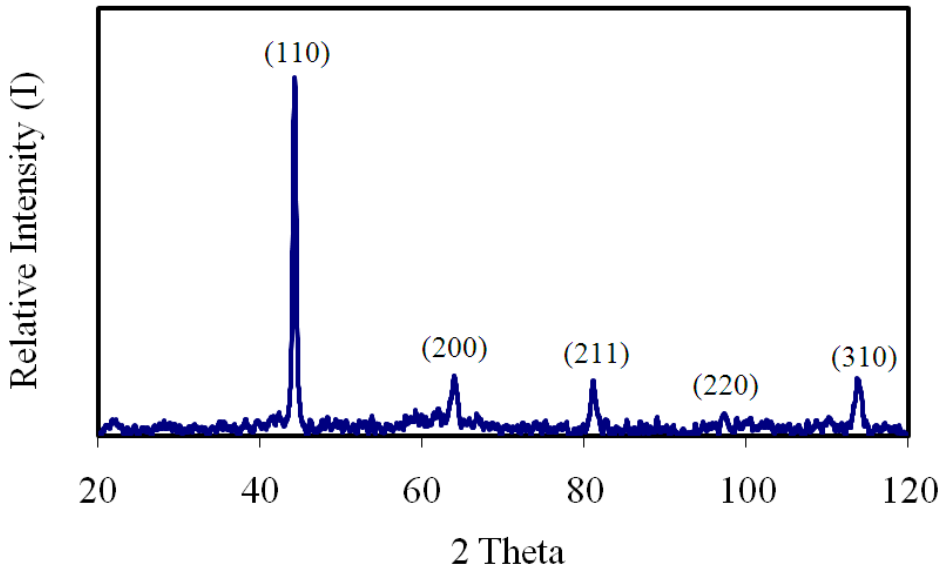

Figure 5.1 A θ-2θ diffraction pattern of the cut face from the as-grown Fe-17.5 at.% Ga alloy.

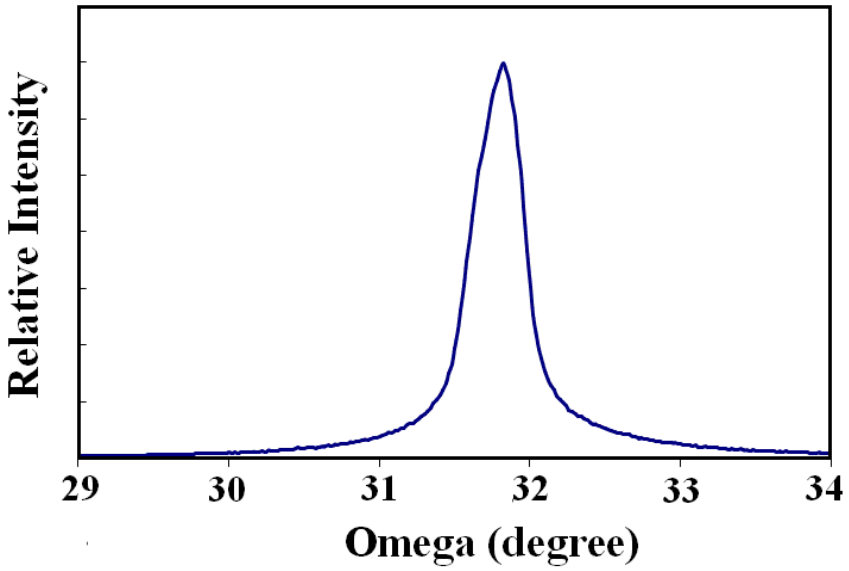

Figure 5.2 A rocking curve corresponding to (002) reflection on the (200) face of [100]-oriented Fe-17.5 at.% Ga single crystal.

one of the faces of the [100]-oriented Fe-17.5 at.% Ga single crystal sample. The maximum in the rocking curve is the omega (ω) value corresponding to optimal specimen orientation for diffraction from the (200) plane. The ω_{max} value of 31.81° obtained from the rocking curve and the 2-theta value of 64.22° corresponding to diffraction from (200) planes of Fe-17.5 at.% Ga alloy indicates that the crystal sample is oriented to within 0.3° from the [100] direction. Figure 5.3 shows a schematic of the oriented single crystal that was used for preparing four identical samples for the three-point bend test. Due to size requirements for the three-point bend test sample and size of the single crystal sample obtained from DG rod, one of the edges of the single crystal (edge 'a' in Figure 5.3) was within 0.3° from the [100] direction, whereas the other two edges of the single crystal (edge 'b' and 'c' in Figure 5.3) were 6 degrees away from the [010] and [001] directions, respectively. This crystallographic orientation was maintained almost the same in all four samples (Figure 5.4) to compare the results of samples tested under different conditions.

5.2 Magnetic Hysteresis Measurement

Figure 5.5 (a) shows the magnetic hysteresis curve of as-cast Fe-17.5 at.% Ga alloy measured at room temperature. The maximum magnetic field applied was 10 kG. The x-axis of the hysteresis curve is the applied magnetic field in G, whereas the y-axis is mass magnetization in emu/g. The saturation magnetization, which is magnetic moment per unit mass above the saturation magnetic field, is obtained from the magnetic moment value corresponding to an applied magnetic field of 10 kG. The saturation magnetization value obtained for Fe-17.5 at.% Ga was 173 emu/g. An enlarged view of this hysteresis curve in the near-zero magnetic field region is shown in Figure 5.5 (b). It can be seen that

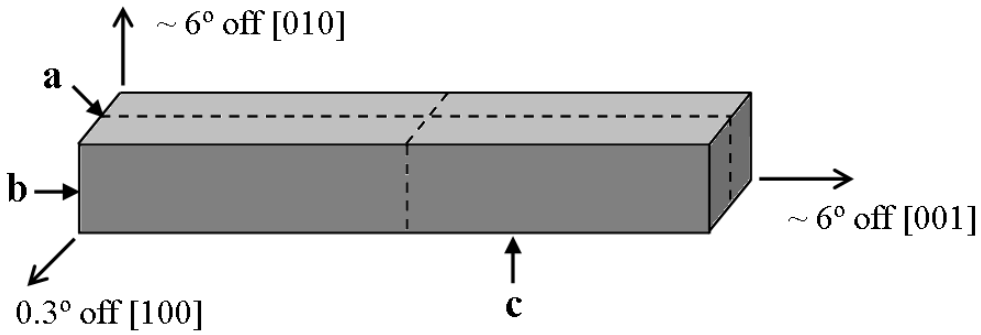

Figure 5.3 A schematic of the crystallographic orientation of the Fe-17.5 at.% Ga single crystal used for preparing four identical samples for the three-point bend tests.

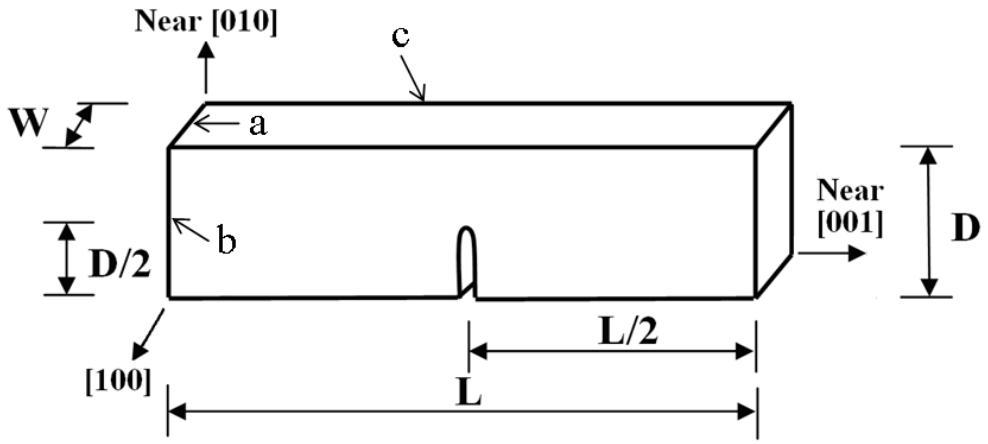

Figure 5.4 A schematic of crystallographic orientation of the Fe-17.5 at.% Ga three-point bend test sample.

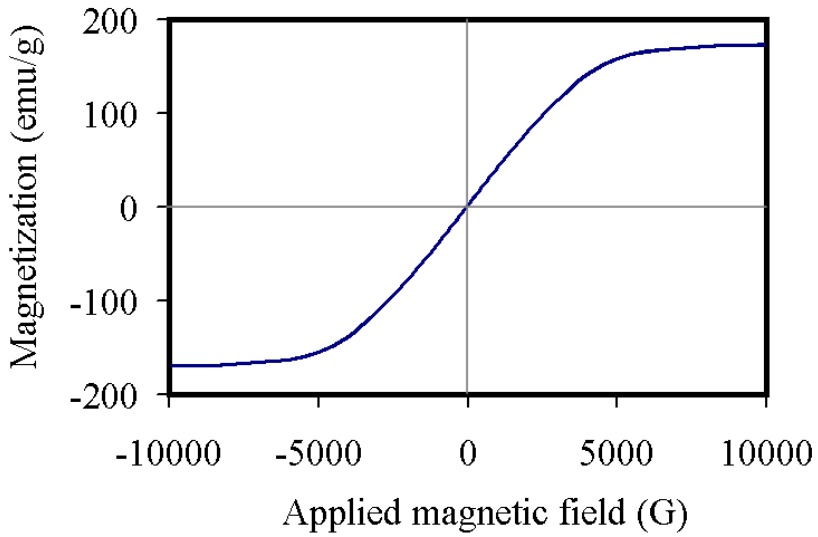

(a)

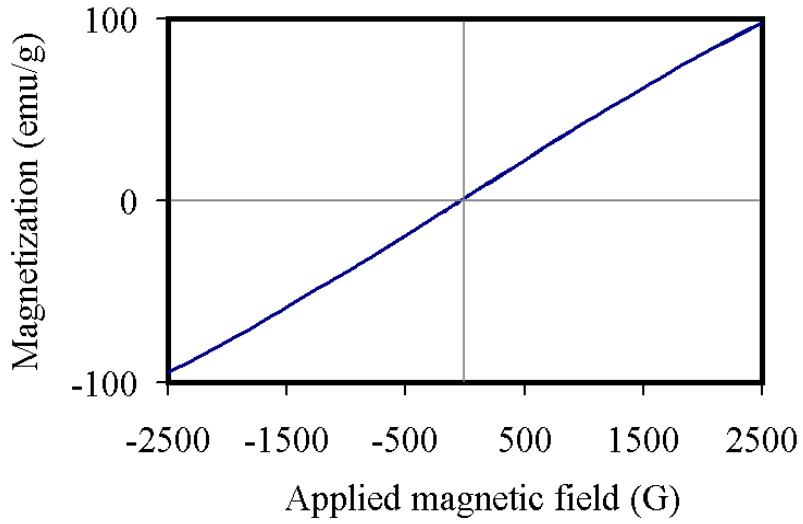

(b)

Figure 5.5 Magnetization curve of as-cast Fe-17.5 at.% Ga alloy showing (a) the full curve and (b) an enlarged view of the near-zero magnetic field region.

the alloy has a very low coercivity and very small hysteresis.

5.3 Magnetostriction Measurements

The magnetostriction coefficient $(3/2)\lambda_{100}$ measurements of the Fe-17.5 at.% Ga alloy single crystal were made on the [001]-oriented single crystal sample. The single crystal sample used for the magnetostriction measurement was vacuum sealed in a quartz tube and heat treated at 1150°C for 2 h followed by water quenching. Figure 5.6 shows the magnetostrictive strain versus magnetic field curves obtained with strain measured along the [001]-direction after applying a magnetic field (i) parallel to the [001] direction ($\lambda_{parallel}$) (Figure 5.6 (a)) and (ii) parallel to the [010] direction ($\lambda_{perpendicular}$) (Figure 5.6 (b)). The difference between these two measured values ($\lambda_{parallel} - \lambda_{perpendicular}$) provided a magnetostriction coefficient $(3/2)\lambda_{100}$ value of 359×10^{-6}.

5.4 Transmission Electron Microscopy Studies

The transmission electron microscopy studies of Fe-17.5 at.% Ga alloy were carried out on a sample prepared from the [001]-oriented single crystal. Figure 5.7 (a) shows a bright field TEM image of the Fe-17.5 at.% Ga sample and the diffraction pattern of the same area is shown in Figure 5.7 (b). The TEM image in Figure 5.7 (a) shows bend contours and thickness fringes. However, no dislocations, grain boundaries or second phase regions were seen in the sample. Detailed examination is however needed to completely rule out the presence of nanoscale coherent second phase regions.

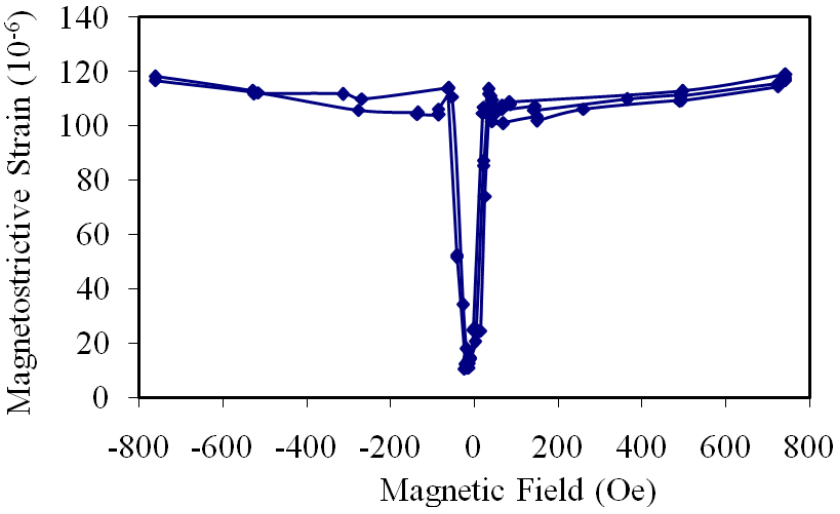

(a)

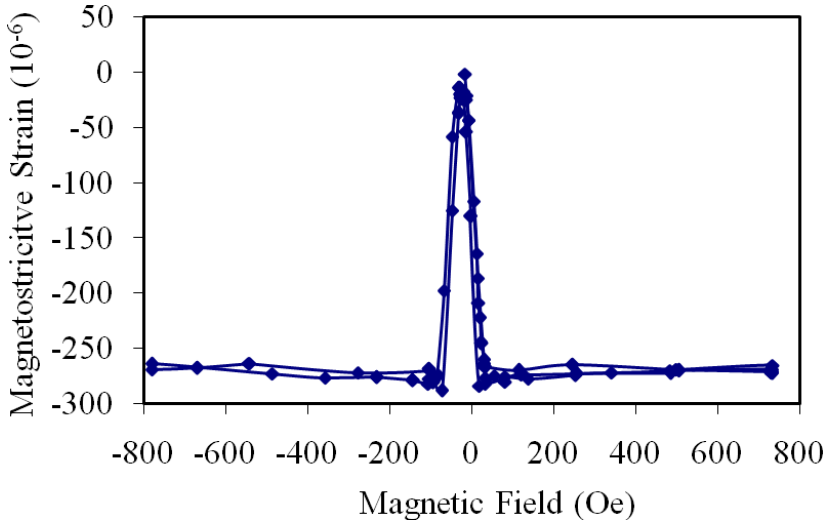

(b)

Figure 5.6 Magnetostrictive strain versus applied magnetic field curves of [001]-oriented Fe-17.5 at.% Ga single crystal in the annealed condition, with strain measured along the [001]-direction after applying magnetic field (a) parallel to [001] direction; (b) parallel to [010] direction.

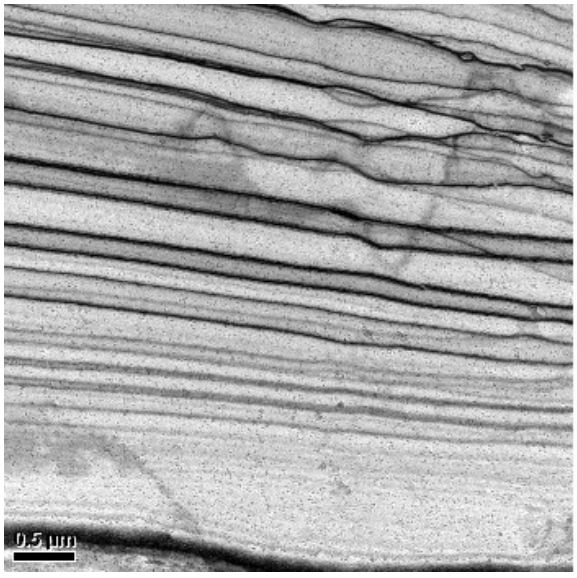

(a)

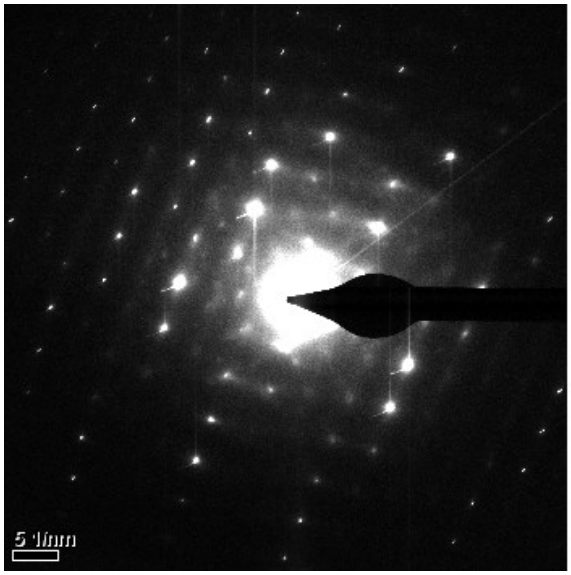

(b)

Figure 5.7 TEM results: (a) bright-field TEM image of Fe-17.5 at.% Ga single crystal sample showing the presence of only the α-phase region; (b) a diffraction pattern from the region shown in Figure 5.7 (a).

5.5 Potentiodynamic Polarization Scan Results

The data for a plot of potential versus logarithm of current density (E vs Log|i|) were obtained from the potentiodynamic polarization scan. The potentiodynamic polarization scan results of the Fe-17.5 at.% Ga single crystal sample and AISI 4340 steel sample are shown in Figure 5.8. Corresponding to a current density of 100 A/m^2, there is no rate limiting step observed on the cathodic line of the polarization plot and so, this current density value was chosen for cathodic hydrogen charging for both the Fe-17.5 at.% Ga single crystal as well as the AISI 4340 steel.

5.6 Three-Point Bend Test Results

Before carrying out the three-point bend tests on Fe-17.5 at.% Ga alloy single crystal samples, AISI 4340 steel samples were used to verify the testing parameters and test configuration. Four sets of identical AISI 4340 steel samples were prepared and tested in five different test conditions.

The load versus midspan deflection data acquired by the computer connected to the Instron machine were used to calculate the bending stress and bending strain [74]. The bending stress (σ_b) and bending strain (ε_b) are given by equations (5.1) and (5.2), respectively.

$$\sigma_b = \frac{3PL}{2WD^2} \quad (MPa) \tag{5.1}$$

$$\varepsilon_b = \frac{6dD}{L^2} \tag{5.2}$$

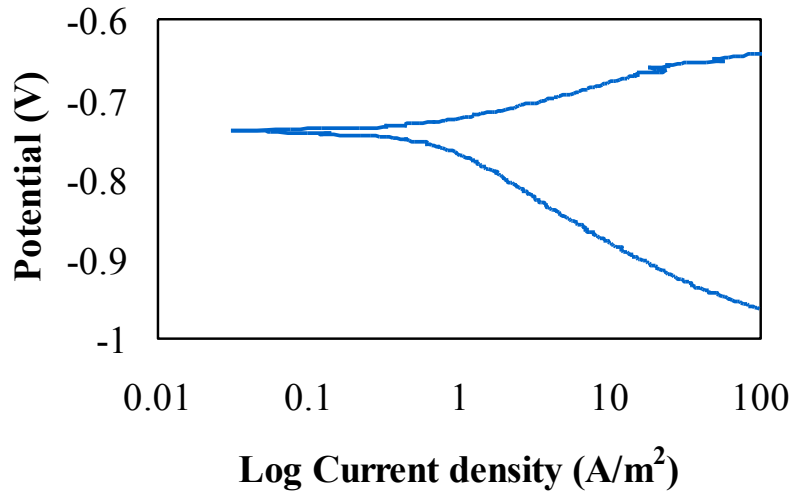

(a)

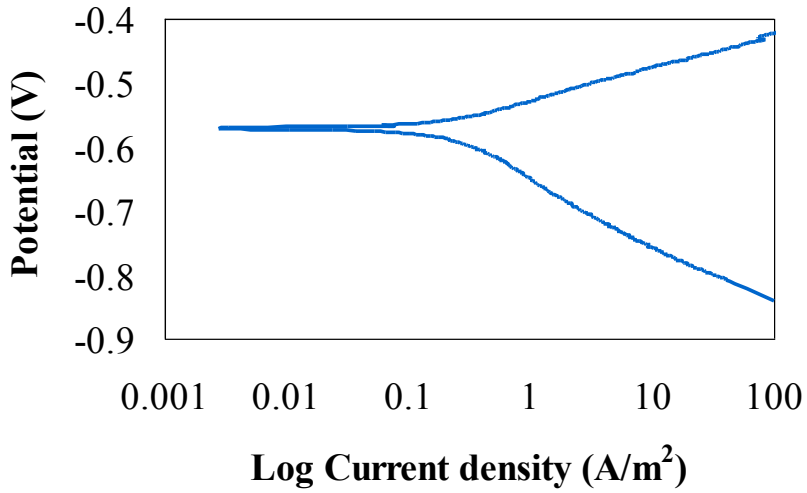

(b)

Figure 5.8 Potentiodynamic polarization scan results of (a) Fe-17.5 at.% Ga alloy single crystal sample and (b) AISI 4340 steel sample in 1N H_2SO_4 with 1 g/L thiourea.

where, P is the load (N), L is the length of the sample (mm), W is the width of the sample (mm), D is the depth or thickness of the sample (mm) and d is the displacement or mid-span deflection (mm).

A quantitative estimate of the effect of hydrogen can be expressed in terms of the hydrogen embrittlement index (HEI). This can be defined as the ratio of a given property when measured in the presence of hydrogen to that in absence of hydrogen and it is given by equation (5.3).

$$\mathrm{HEI} = \frac{(\varepsilon_0 - \varepsilon_H)}{\varepsilon_0} \times 100 \tag{5.3}$$

where, ε_0 is the maximum bending strain in the case without hydrogen charging, and ε_H is the maximum bending strain in the case with hydrogen charging. A larger value of HEI signifies a larger effect of hydrogen on ductility.

5.6.1 Three-Point Bend Test Results of AISI 4340 Steel Samples

Four identical samples were tested for each test condition. The three-point bend test results of four sets of AISI 4340 steel samples tested in five different test conditions are presented in the bending stress versus bending strain plot (Figures 5.9 and 5.10). Each curve is an average of four tests and the error range for each set is also shown in the figure. The average maximum bending stress and bending strain values for these test samples are shown in Table 5.1. The error range varied for the samples tested under different conditions as can be seen from the error bars on the respective bending stress – bending strain curves for each of the five different test conditions. The standard deviation

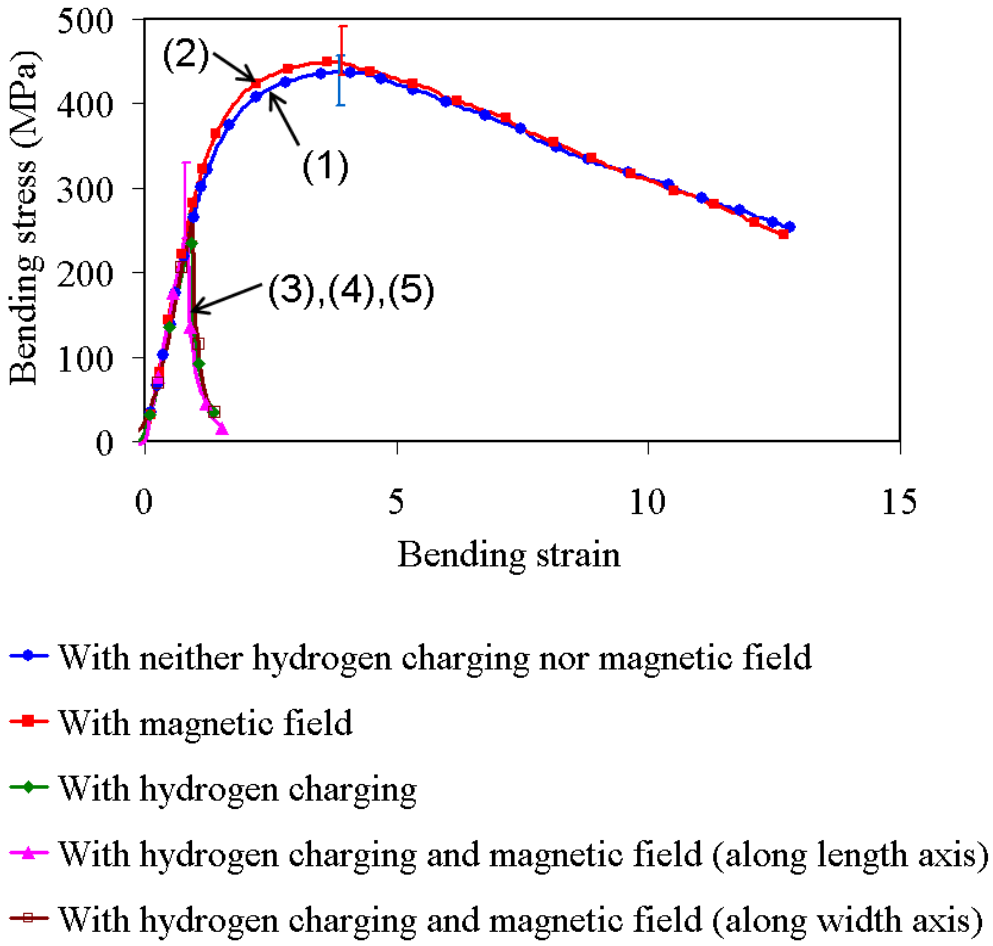

Figure 5.9 Three-point bend test results of AISI 4340 steel samples under various test conditions.

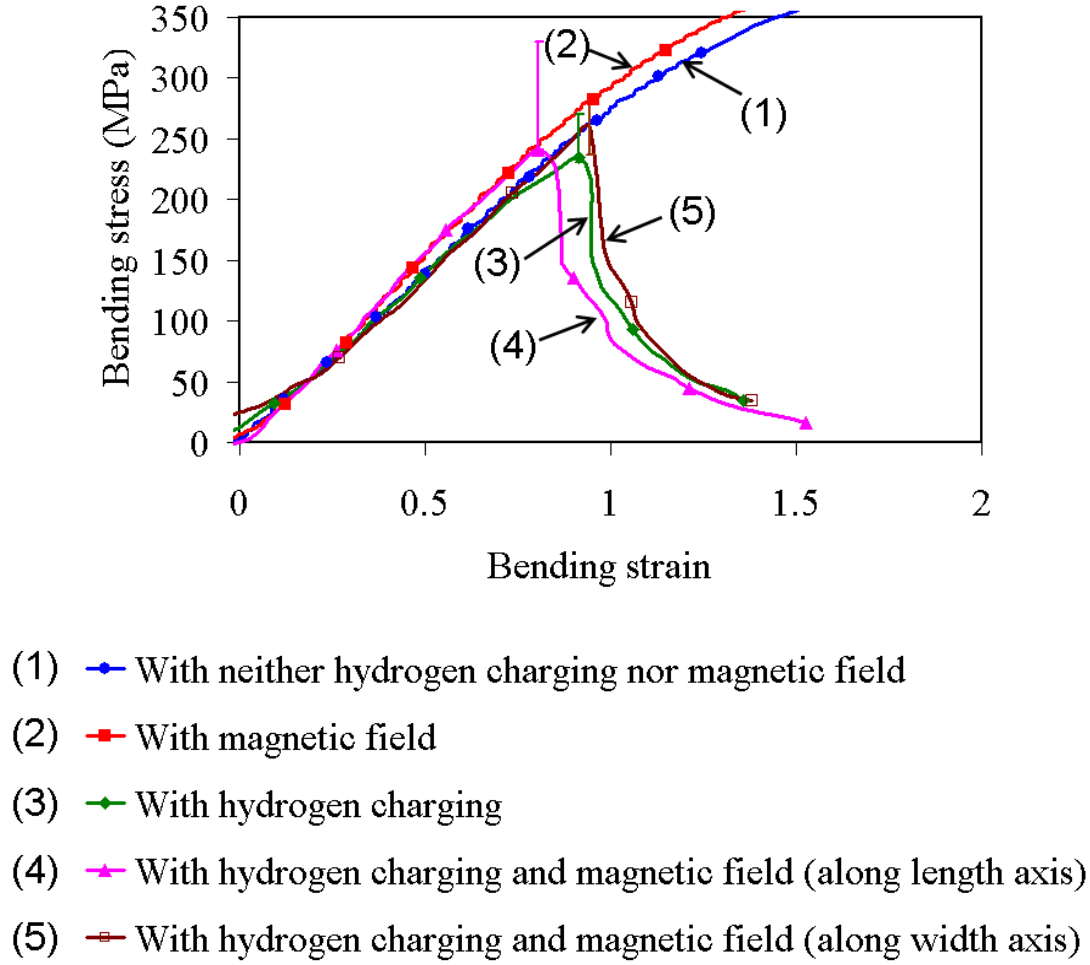

Figure 5.10 Three-point bend test results of AISI 4340 steel samples under various test conditions - a magnified view of Figure 5.9 to clearly show results of hydrogen charged samples.

Table 5.1

Three-point bend test results of AISI 4340 steel samples tested under different test conditions.

Test conditions	**Maximum bending stress (MPa)**	**Maximum bending strain (%)**	**Hydrogen embrittlement index**
With neither hydrogen charging nor magnetic field	438	3.8	
With magnetic field	450	4.2	
With hydrogen charging	235	0.9	76
With hydrogen charging and magnetic field (along length axis)	241	0.8	79
With hydrogen charging and magnetic field (along width axis)	259	0.9	76

of the three-point bend test results of four sets of samples tested under five different test conditions are shown in Table 5.2.

The AISI 4340 steel sample tested with neither hydrogen charging nor magnetic field was observed to have a maximum bending stress of 438 MPa at a corresponding bending strain of 3.8 %. The sample tested with only magnetic field was seen to have a maximum bending stress of 450 MPa at a corresponding bending strain of 4.2 %. The difference between these two test conditions are within the error range and so, the effect of magnetic field on the sample tested without hydrogen charging is seen to be negligible.

The AISI 4340 steel sample tested with hydrogen charging is seen to have a maximum bending stress of 235 MPa with a corresponding bending strain of 0.9 %. It is seen that the presence of hydrogen lowers the bending stress and bending strain values drastically. The HEI for the sample tested with hydrogen charging shows a very high value of 76, indicating that the presence of hydrogen affects the material ductility drastically and this alloy is highly prone to hydrogen embrittlement.

In the case of samples tested with hydrogen charging and magnetic field applied along the length axis, the observed maximum bending stress is 241 MPa and corresponding bending strain is 0.8 %. The HEI in this case is 79. In the case of samples tested with hydrogen charging and magnetic field applied along the width axis, the observed maximum bending stress is 259 MPa and the corresponding bending strain is 0.9 %. The HEI in this case is 76. The samples tested with hydrogen charging in the presence of applied magnetic field has bending stress and bending strain values close to that of the hydrogen charged samples tested without magnetic field. The direction of applied magnetic field is not seen to have any significant effect on the bending stress and

Table 5.2

Standard deviation of the three-point bend test results of AISI 4340 steel samples tested under different test conditions.

Test conditions	**Standard deviation of the maximum bending stress (MPa)**	**Standard deviation of the maximum bending strain (%)**
With neither hydrogen charging nor magnetic field	22.9	0.51
With magnetic field	24.2	0.48
With hydrogen charging	15.9	0.07
With hydrogen charging and magnetic field (along length axis)	38.7	0.11
With hydrogen charging and magnetic field (along width axis)	17.1	0.12

bending strain values and is within the error range. The HEI for hydrogen charged samples with and without magnetic field are almost the same.

The standard deviation of the maximum bending stress ranges from about 15 to 40 MPa. The standard deviation of the corresponding bending strain ranges from about 0.1 to 0.5 %. In case of hydrogen charged samples, the deviation in bending strain value is about 0.1 % and from these results, it can be concluded that, in case of hydrogen charged samples, the test setup gives close and reproducible ductility values.

5.6.1.1 SEM Fracture Studies

Figure 5.11 and 5.12 show the fracture surfaces of the AISI 4340 steel three-point bend test samples tested under various test conditions. The fracture surface of the sample tested with neither hydrogen charging nor magnetic field (Figure 5.11 (a)) is seen to have a ductile type fracture resulting from microvoid nucleation, growth and coalescence. It is seen to have a large distribution of dimples, indicating extensive plastic deformation. The fracture surface of the sample tested with hydrogen charging (Figure 5.11 (b)) is seen to have predominantly cleavage type fracture regions with some ductile regions. The only difference in these ductile regions is that the sample tested without hydrogen charging has more elongated dimples than that observed in the sample tested with hydrogen charging. The flat and smooth facets on the fracture surface indicate quasi-cleavage type of failure. In the quasicleavage mode, fracture occurs along transgranular paths, producing fracture surfaces similar to that caused by pure cleavage type fracture. The distinct difference is that the cleavage characteristics of maintaining one or few growing crack fronts as the crack progresses from one crystal to another are usually absent in

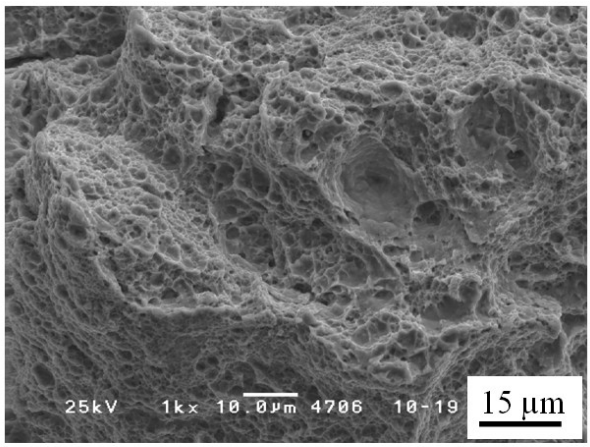

(a)

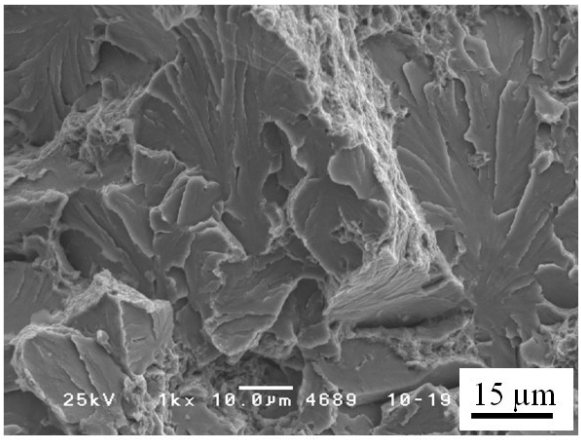

(b)

Figure 5.11 SEM fracture surface images of three-point bend tested AISI 4340 steel samples (a) with neither hydrogen charging nor magnetic field; (b) with hydrogen charging.

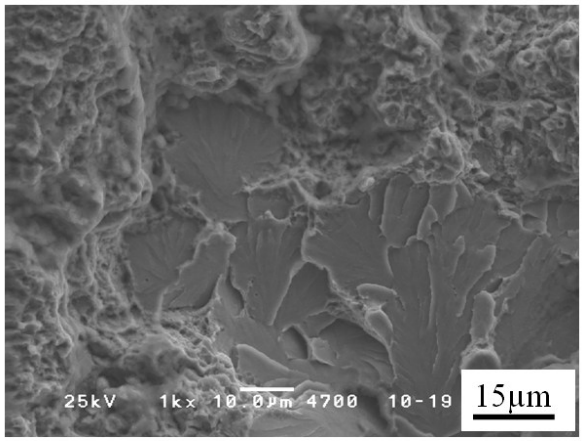

(c)

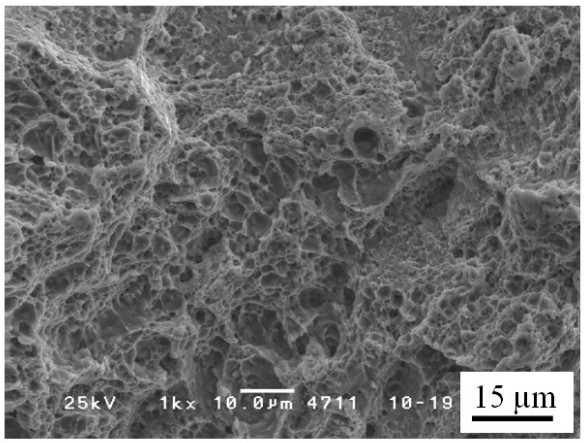

(d)

Figure 5.12 SEM fracture surface images of three-point bend tested AISI 4340 steel samples (a) with hydrogen charging and magnetic field; (b) with magnetic field.

quasicleavage. The fracture proceeds by the growth of these crack fronts that occurs by uniting with small embedded cracks in the material ahead of the macroscopic crack. This behavior is termed as satellite nucleation of cracks [75].

The fracture surface of the sample tested with hydrogen and magnetic field shows a mix of ductile and quasicleavage type of fracture (Figure 5.12 (a)), very similar to that of the hydrogen charged sample tested without magnetic field (Figure 5.11 (b)). The fracture surface of the sample tested with only magnetic field (Figure 5.12 (b)) has extensive ductile tearing and is not very different from that tested with neither hydrogen nor magnetic field (Figure 5.11(a)). Hydrogen embrittlement is characterized by a change in the fracture mode from ductile tearing to brittle quasicleavage type fracture.

5.6.1.2 Acoustic Emission Measurement Results

The acoustic emission signals collected during the three-point bend test of AISI 4340 steel with and without hydrogen charging are shown in Figures 5.13 and 5.14, respectively. The x-axis is the actual time of the bend test in minutes and y-axis is the signal intensity in voltage. The intensity of the acoustic emission signal corresponds to the energy release during crack propagation and each major step of the crack growth process is detected as an emission event.

The sample tested with hydrogen charging (Figure 5.13 (a)) is seen to have a single acoustic emission event, which shows sudden cracking. The sample tested without hydrogen charging (Figure 5.14 (a)) shows many emission events, indicating progressive crack growth, and each major step of the crack growth has an associated emission event. The cumulative acoustic emission intensity in the case of the sample without hydrogen

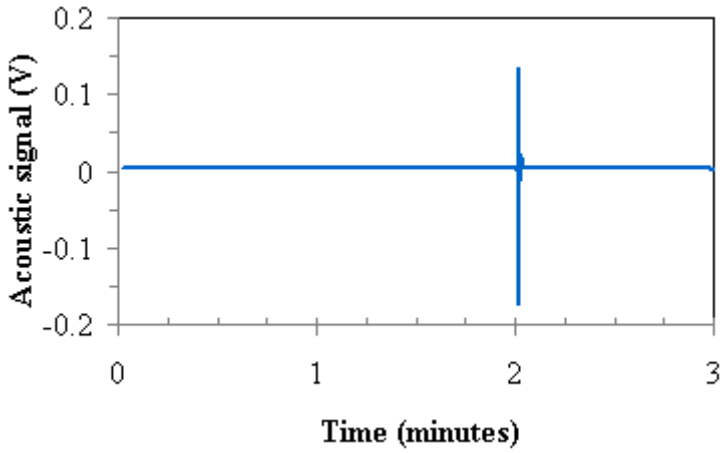

(a)

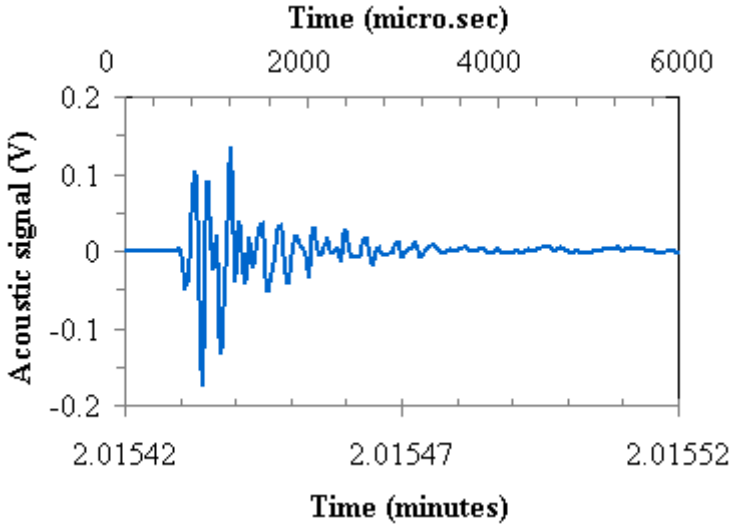

(b)

Figure 5.13 Acoustic emission spectra of the AISI 4340 steel sample tested: (a) with hydrogen charging; and (b) an enlarged view of the highest intensity emission signal in Figure 5.13 (a).

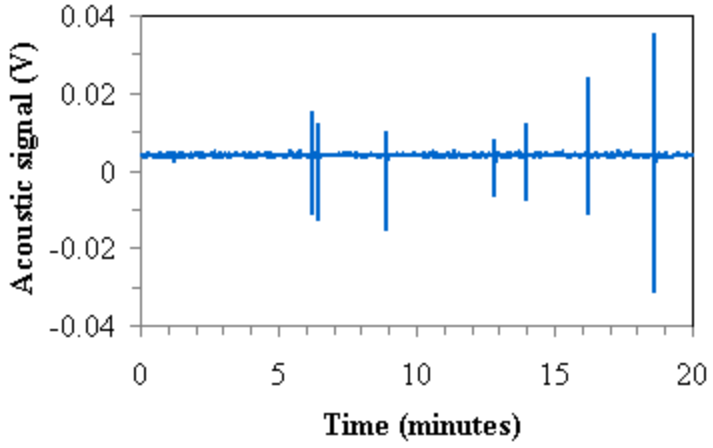

(a)

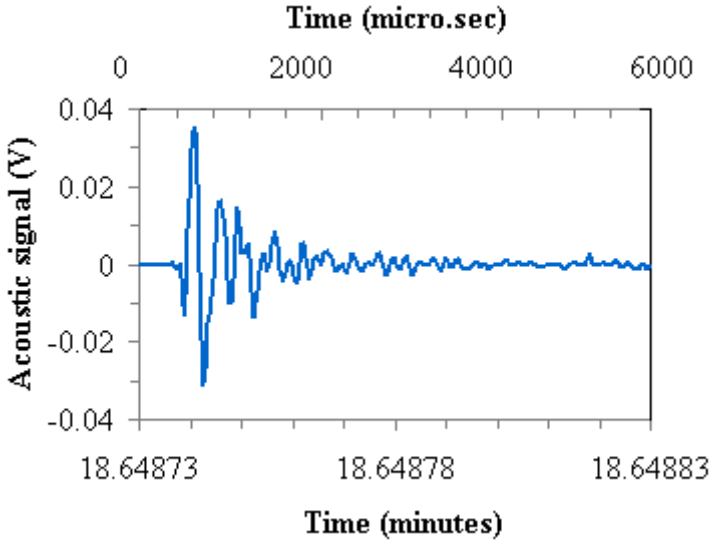

(b)

Figure 5.14 Acoustic emission spectra of AISI 4340 steel sample tested: (a) without hydrogen charging; and (b) an enlarged view of the highest intensity emission signal in Figure 5.14 (a).

charging is higher than that of the sample tested with hydrogen charging. This intensity corresponds to the energy consumed during crack propagation, with the ductile fracture process (of sample tested without hydrogen charging) being a more energy-consuming process than the brittle cleavage fracture (of sample tested with hydrogen charging) [75]. Figures 5.13 (b) and 5.14 (b) show the acoustic emission signal patterns for shorter time periods of 6000 microseconds (6 milliseconds) near the maximum intensity peaks of Figures 5.13 (a) and 5.14 (a), respectively.

5.6.2 Three-Point Bend Test Results of Fe-17.5 at.% Ga

Single Crystal Samples

The bending stress versus bending strain plots of data obtained from the three-point bend tests of Fe-17.5 at.% Ga alloy single crystal samples tested in four different test conditions are presented in Figure 5.15. The maximum bending stress and the corresponding bending strain values for these test samples are shown in Table 5.3.

The sample tested without hydrogen charging and magnetic field has a maximum bending stress of 210 MPa at a bending strain of about 1.4 %. The sample tested with hydrogen charging has a maximum bending stress of 132 MPa at a strain value of 0.9 %. This shows that the presence of hydrogen drastically reduces the ductility and fracture stress values. The hydrogen charged sample tested with magnetic field applied along the length axis has a maximum bending stress of 146 MPa at a strain value of 1.08 %. The hydrogen charged sample tested with magnetic field applied along the width axis has a maximum bending stress of 151 MPa at a strain value of 1.13 %. In the case of samples tested with hydrogen charging and magnetic field, irrespective of the direction of applied

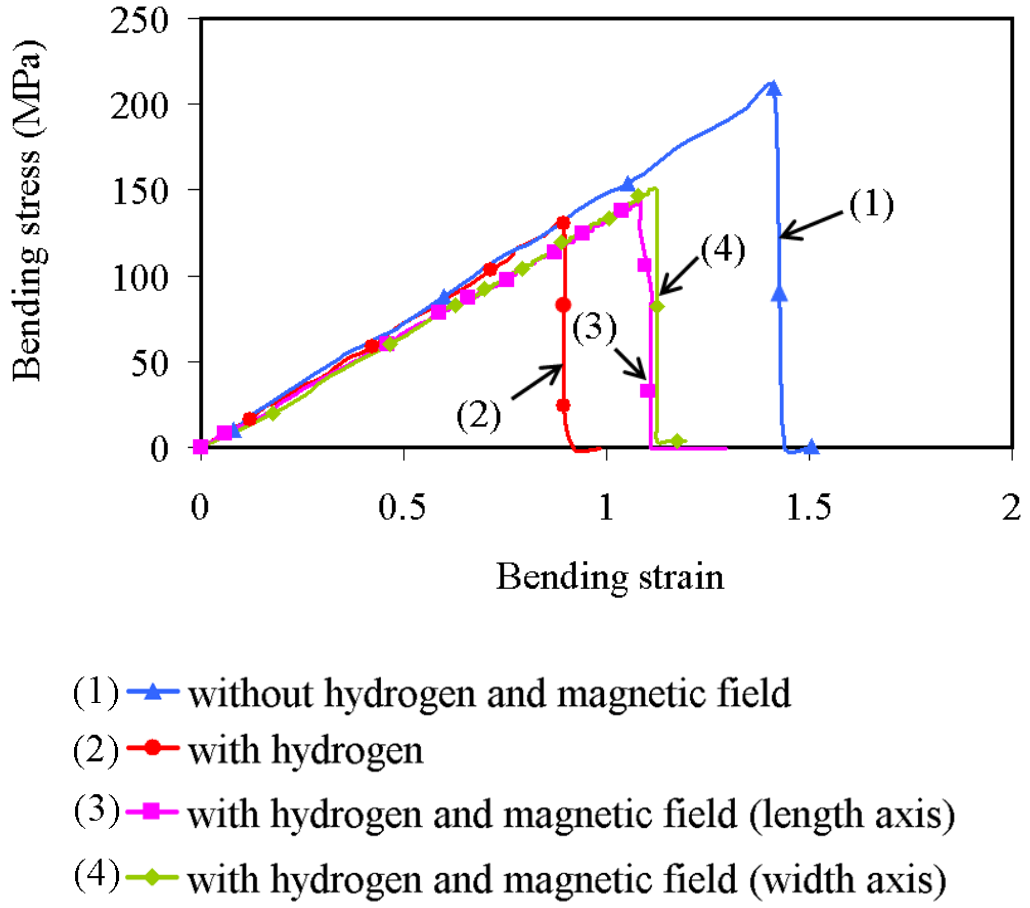

Figure 5.15 Three-point bend test results of Fe-17.5 at.% Ga single crystal samples under various test conditions.

Table 5.3

Three-point bend test results of Fe-17.5 at.% Ga single crystal samples tested under different test conditions.

Test conditions	**Maximum bending stress (MPa)**	**Maximum bending strain (%)**	**Hydrogen embrittlement index**
Without hydrogen charging and magnetic field	210	1.4	
With hydrogen charging	132	0.9	36
With hydrogen charging and magnetic field (along length axis)	146	1.08	23
With hydrogen charging and magnetic field (along width axis)	151	1.13	19

magnetic field, there is an increase in the bending strain values compared to the sample tested with only hydrogen charging. An applied magnetic field increases the bending strain value by about 10-20 % along with an increase in the cleavage stress value by about 20-25 %. This increase in bending strain is associated with a decrease in elastic modulus value with applied magnetic field. A similar decrease in elastic modulus for this alloy in the case of bend test samples with applied magnetic field near saturation was reported by Datta et al. [51, 55]. HEI for the sample tested with hydrogen charging in the presence of magnetic field shows a slightly lower value than that without magnetic field (Table 5.3).

It can be seen that the bending stress value in the case of the hydrogen charged sample with magnetic field applied along the width axis is about 10 % higher than that of the sample with magnetic field applied along length axis and corresponding increase in bending strain value is about 5 %. This difference can be attributed to the rotation and alignment of magnetic domains in the magnetized sample in the presence of stresses. Gradual variation of stress from tensile to compressive values across the sample plane parallel to the notch makes it difficult to interpret the influence of direction of applied magnetic field and this requires mathematical modeling to understand the magnetic domains structure within the material in the presence of combined stresses.

5.6.2.1 SEM Fracture Studies

Figure 5.16 (a-d) shows the low magnification SEM fracture surface images of the Fe-17.5 at.% Ga single crystal samples tested under various test conditions. At low magnification, the fracture surface looks almost flat and parallel to the notch plane. This

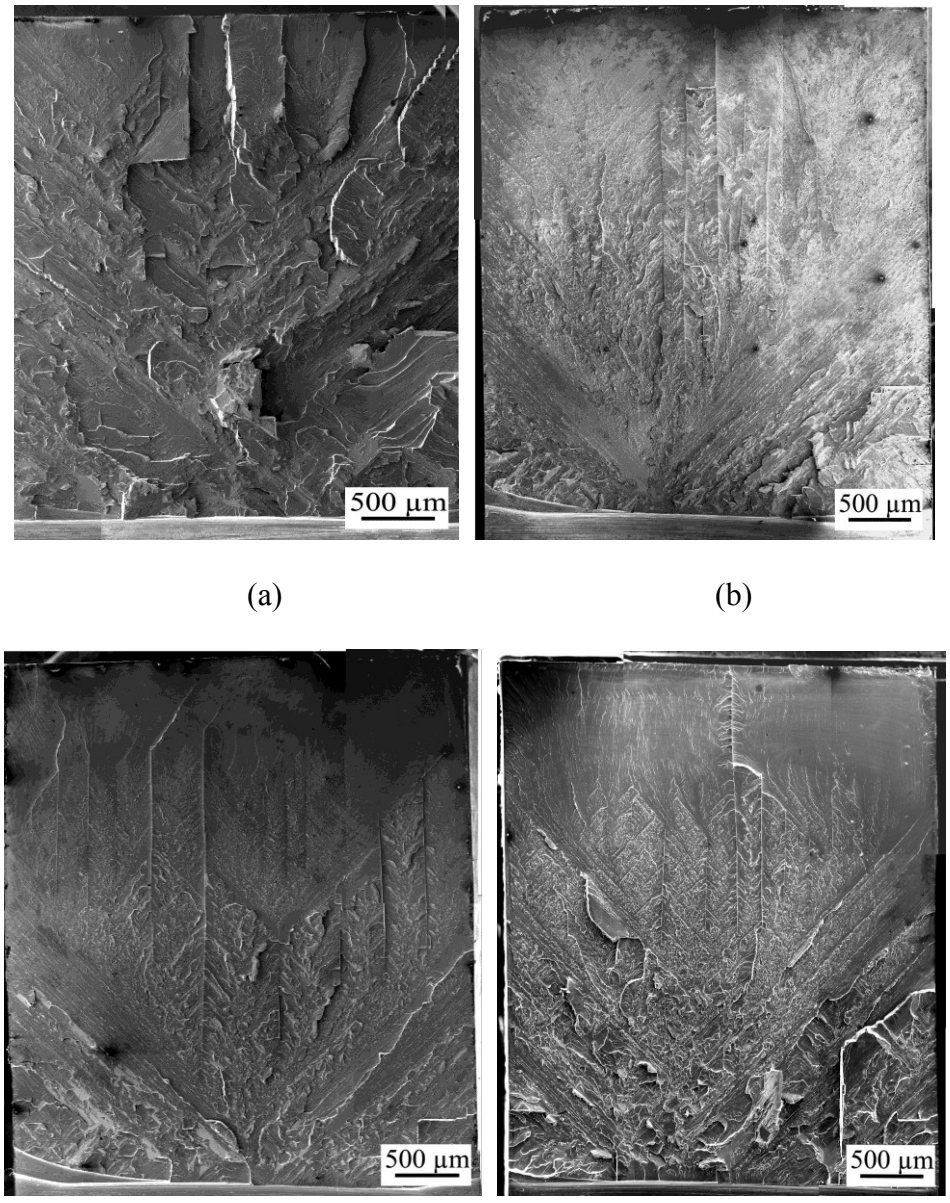

Figure 5.16 SEM fracture surfaces of Fe-17.5 at.% Ga single crystal three-point bend test sample: (a) with neither hydrogen charging nor magnetic field; (b) with hydrogen charging; (c) with hydrogen charging and magnetic field (along length axis); and (d) with hydrogen charging and magnetic field (along width axis).

is due to the close orientation of the sample notch plane to the (100) slip plane. In all four samples, it is observed that the fracture initiated at the notch tip, which is the lower end of the fracture surface image, and has progressed overall along the [010] direction on the (001) cleavage plane (Figure 5.17). The fracture surface of the sample tested without hydrogen charging and magnetic field (Figure 5.16 (a)) is seen to have multiple steps in the fracture plane with ductile fracture features, indicative of plastic deformation during fracture. In the other three samples tested with hydrogen charging (Figures 5.16 (b), 5.16 (c) and 5.16 (d)), there are fewer steps that are seen near the crack initiation region, after which the crack propagation seems to have occurred by sudden cleavage fracture. The hydrogen charged samples tested with and without magnetic field have similar fracture surfaces. But in the case of samples tested with hydrogen charging and magnetic field applied along the width direction (Figure 5.16 (d)), it is observed that there is more plastic deformation region compared to the other hydrogen charged samples (Figures 5.16 (b) and 5.16 (c)). This observation of fracture surface features can well be related to the increase in the bending stress and bending strain values observed for this sample compared to other hydrogen charged samples.

At higher magnification, the sample tested without hydrogen charging and magnetic field (Figures 5.18 (a) and 5.18 (b)) is seen to have both ductile (Figure 5.18 (a)) as well as quasicleavage (Figure 5.18 (b)) fracture regions. Figure 5.18 (a) shows cup-and-cone dimple morphology, indicating ductile tearing, whereas Figure 5.18 (b) shows a region with quasicleavage fracture that occurred in multiple steps. The sample tested with hydrogen charging (Figure 5.19) shows a more brittle character as revealed by a larger fraction of cleavage facets on the fracture surface. There are very few or no

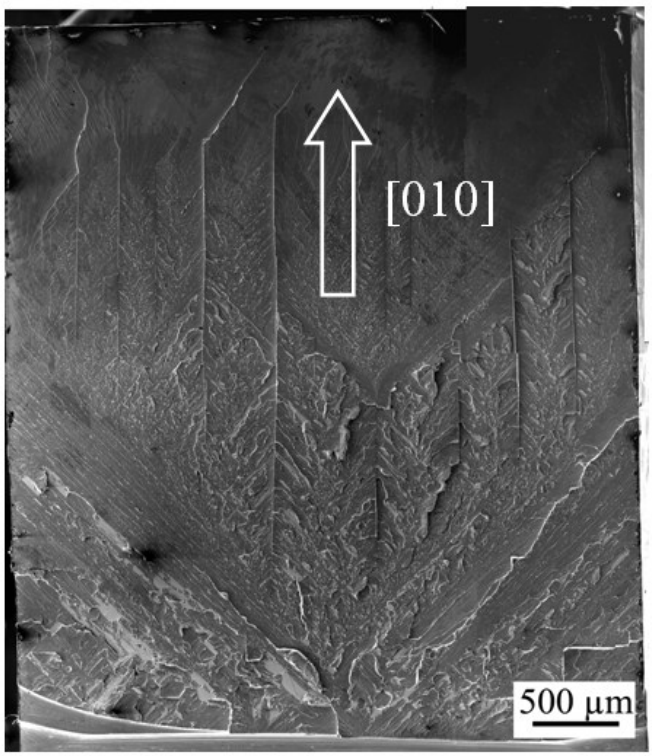

Figure 5.17 SEM fracture surfaces of Fe-17.5 at.% Ga single crystal three-point bend test sample showing cleavage crack growth along the [010] direction on the (001) cleavage plane.

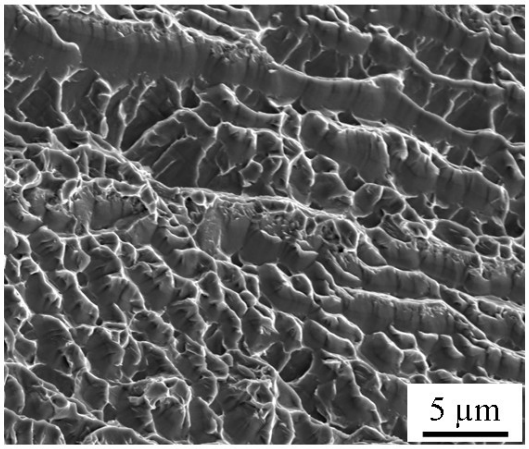

(a)

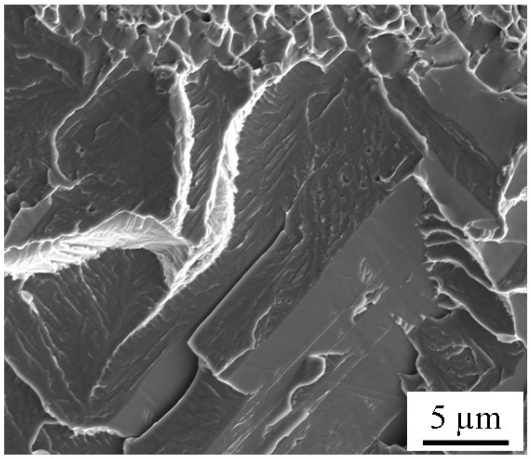

(b)

Figure 5.18 SEM fracture surfaces of Fe-17.5 at.% Ga single crystal three-point bend test sample tested without hydrogen charging and magnetic field.

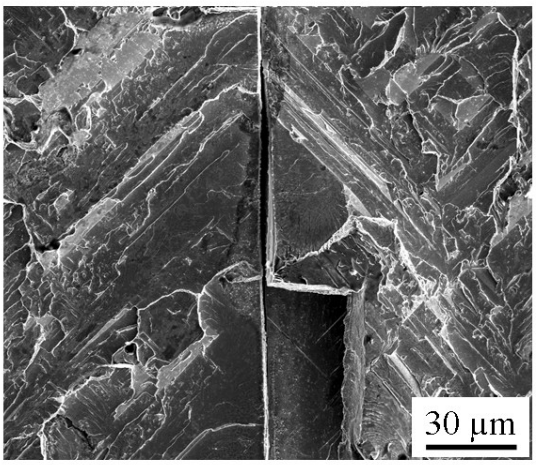

(a)

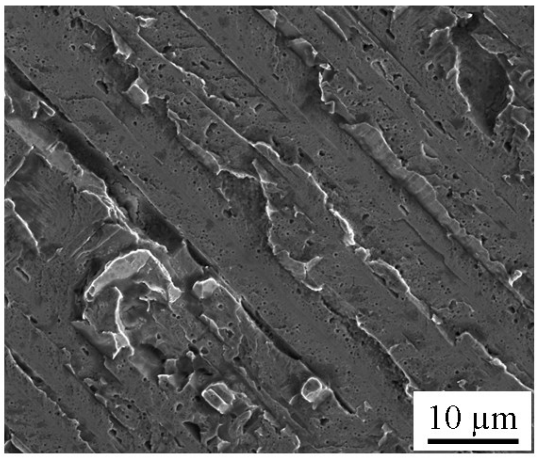

(b)

Figure 5.19 SEM fracture surfaces of Fe-17.5 at.% Ga single crystal three-point bend test sample tested with hydrogen charging.

ductile features seen on this sample. Similar fracture features are seen in the case of the sample tested with hydrogen charging and magnetic field along the length axis (Figure 5.20). The sample tested with hydrogen charging and magnetic field along the width axis has a combination of quasicleavage (Figure 5.21 (a)) and cleavage (Figure 5.21 (b)) fracture regions. Hydrogen embrittlement in this alloy is characterized by a change in the fracture mode from a more ductile to a brittle cleavage type fracture.

In the case of hydrogen charged sample, crack propagation is along the bending plane and occurs as mode I type cleavage fracture, similar to that observed by Hirth et al. [28, 76]. It was shown by Hirth et al. that dynamic charging during the test results in crack nucleation at a much lower strain than that in precharged samples or samples without hydrogen charging. The reduction in strain value in the hydrogen charged sample compared to the uncharged sample confirms this. The stress concentration at the notch tip leads to defect concentration at the notch tip. The solute hydrogen accumulates at these lattice defects, lowers the cohesive strength of the lattice and as the stress increases continuously, the crack initiates at a critical combination of stress and hydrogen concentration.

5.6.2.1.1 Cleavage fracture features seen on hydrogen charged samples

The major characteristic of cleavage is the orientation relationship between the plane of the crack and the crystal structure through which the crack passes. For example, in iron, cleavage occurs along the {100} planes and sometimes along the boundaries between the matrix and {112} mechanical twins [75, 77, 78]. This orientation relationship causes several microscopic fracture surface features usually associated with cleavage. The most evident feature is the flatness of the facets, seen as highly reflecting

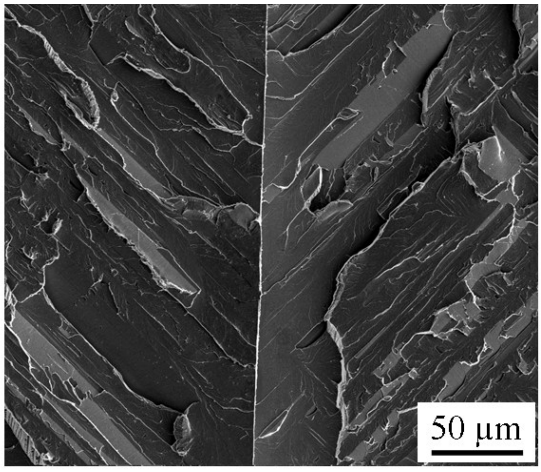

(a)

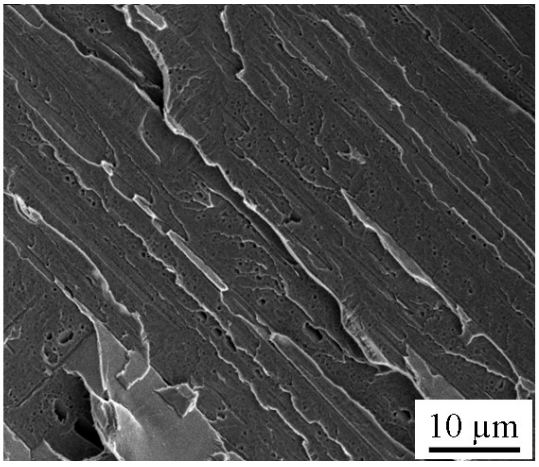

(b)

Figure 5.20 SEM fracture surfaces of Fe-17.5 at.% Ga single crystal three-point bend test sample tested with hydrogen charging and magnetic field along length axis.

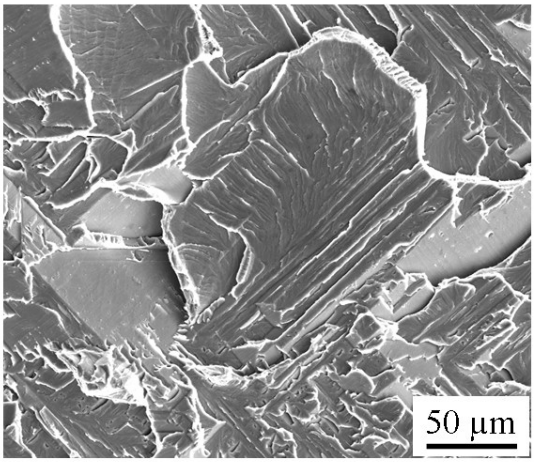

(a)

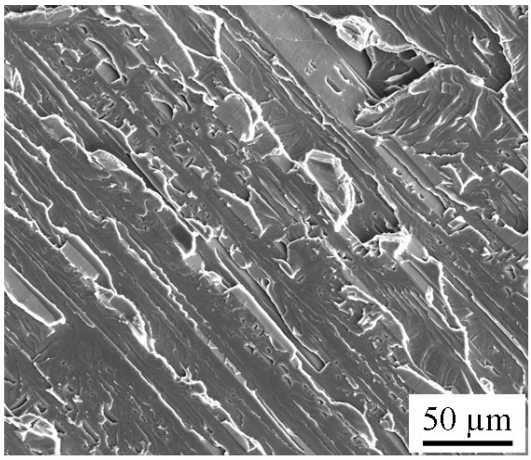

(b)

Figure 5.21 SEM fracture surfaces of Fe-17.5 at.% Ga single crystal three-point bend test sample tested with hydrogen charging and magnetic field along width axis.

regions under the microscope. The persistence of cleavage cracks in following certain specific families of crystallographic planes gives rise to the second most evident fractographic feature – cleavage steps. A brief explanation of the various cleavage fracture features observed in the hydrogen charged Fe-17.5 at.% Ga single crystal sample that occur during crack initiation and propagation are given here.

The cleavage crack is initiated at one point along the notch tip and it fans out into the whole crystal from this one point. This action produces cleavage surfaces, as shown in Figure 5.22, and the overall appearance is called a fan [75]. The arrow shows how the crack initiated at the bottom centre and propagated fanning out.

Another type of feature formed by cleavage is shown in Figure 5.23 (a). These features are called tongues and are formed by local fracture along twin-matrix interfaces [75, 78]. The overall crack propagation direction is indicated by the large arrow, whereas the smaller arrows indicate the way that the crack is locally diverted by individual twins. It can be seen here that the tongues have formed at right angles to one another, which is typically observed in the cleavage of iron. The smaller arrow shows the twins with {112} <111> orientation and are close to about 45° to the {100} cleavage plane [75].

The mechanism of tongue formation and crack propagation along the twin-matrix interface in the iron single crystal was explained by Beachem [75] and a very similar observation is seen in the case of the Fe-Ga single crystal in this work. These tongues are formed when a cleavage crack growing along as the {100} plane intersects a {112} twin interface and propagates along the interface for a short distance, whereas the {100} cleavage continues around the twin. Final local fracture occurs when the metal remaining between the two local cracks deforms and separates. This local propagation direction is

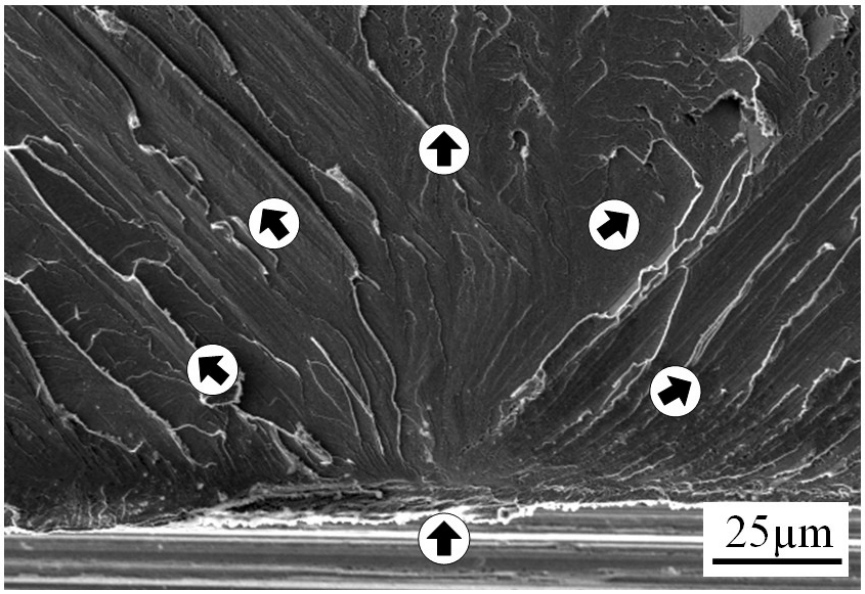

Figure 5.22 Cleavage crack initiation and propagation in Fe-17.5 at.% Ga single crystal sample tested with hydrogen charging.

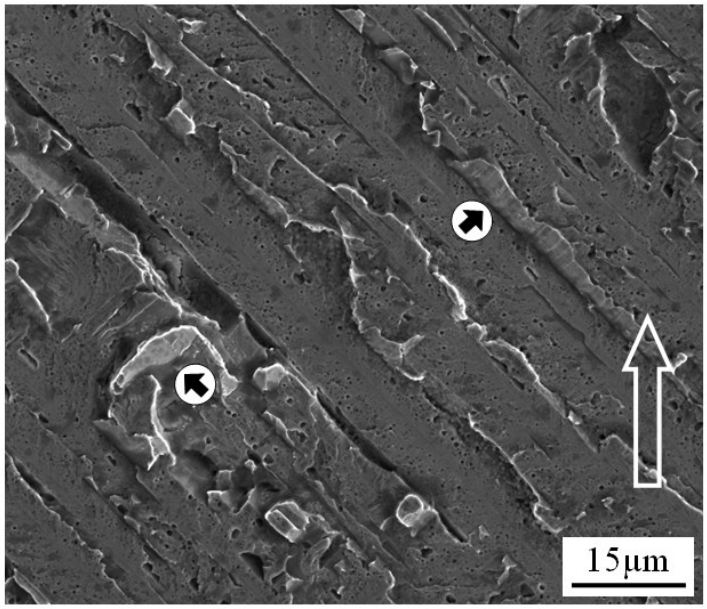

(a)

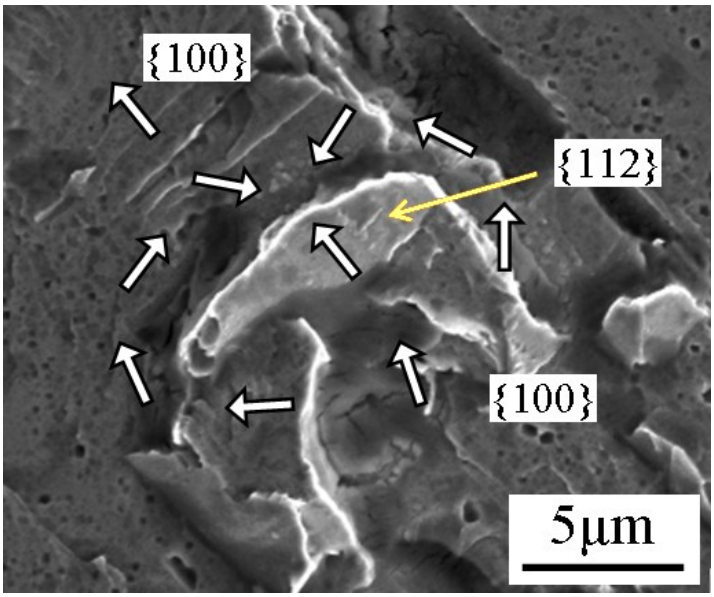

(b)

Figure 5.23 Cleavage fracture features seen in Fe-17.5 at.% Ga single crystal sample tested with hydrogen charging (based on observation by Beachem [75] in iron-single crystals).

shown by the arrows in Figure 5.23 (b). These simultaneous propagations occurring along {100} and {112} planes eventually join along a third path. It has been shown by Hwang et al. [77] that cathodic charging introduces hydrogen-induced slip and twinning in iron alloys.

Another cleavage feature caused by simultaneous cleavage along {100} and {112} twin-matrix interfaces is shown in Figure 5.24 and is termed as a herring bone pattern [79]. The fracture directions are shown by the arrows (Figure 5.24 (b)), with the centre being one of the <100> directions and the directions to either side being two of the <110> directions. The regions to either side of the central strip are formed by cleavage on the {100} and pairs of {112} twin-matrix interfaces. Considering the overall fracture to be the (100) plane, the twins contributing to fracture along with (100) cleavage in these side regions would be the {112} set of planes [75]. This is reported to be a typical fracture feature, especially in case of environmental induced cleavage fractures of single crystals [79].

5.6.2.2 Acoustic Emission Measurement Results

The acoustic emission signals collected during the three-point bend tests under various test conditions are shown in Figure 5.25, 5.26, 5.27 and 5.28. The x-axis refers to the actual time of the bend test in minutes and y-axis refers to the signal intensity in voltage. The intensity of the acoustic emission signal corresponds to the energy release during crack propagation and each major step of the crack growth process is detected as an emission event. Figures 5.25 (a), 5.26 (a), 5.27 (a) and 5.28 (a) show the acoustic emission signal over the entire time span of the test, whereas Figures 5.25 (b), 5.26 (b),

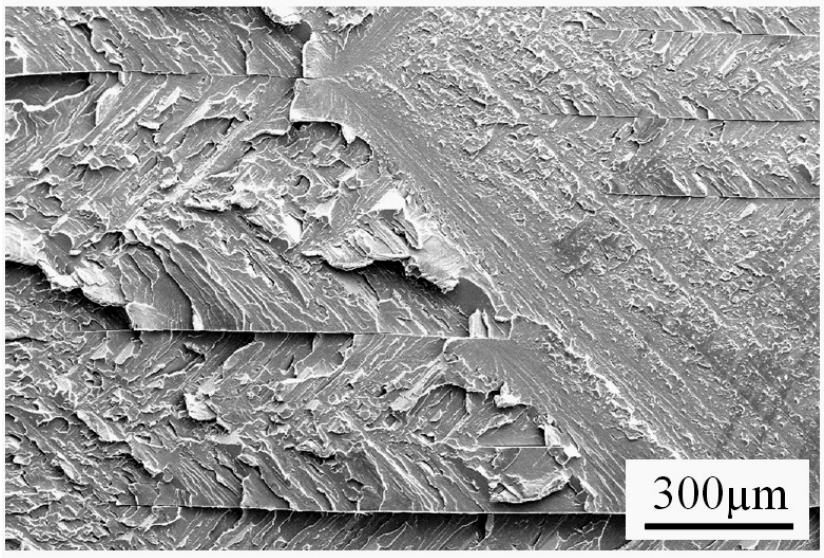

(a)

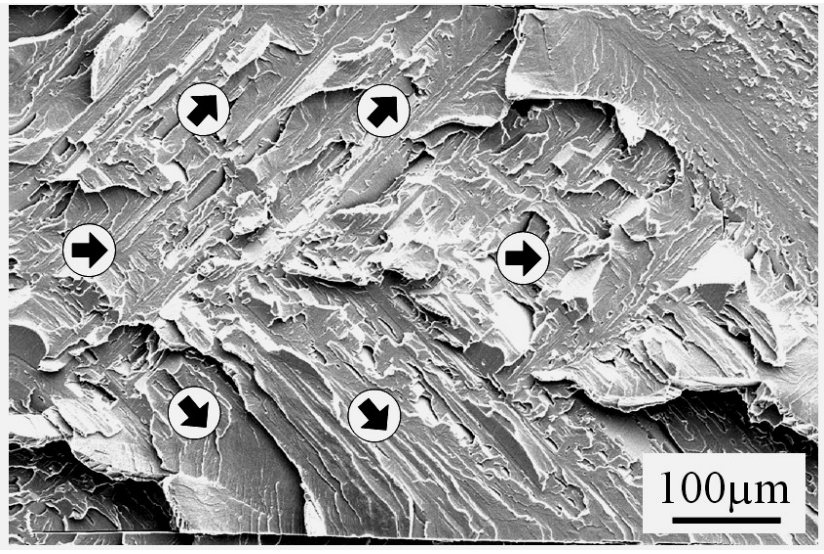

(b)

Figure 5.24 Herring-bone pattern seen on the fracture surface of Fe-17.5 at.% Ga single crystal sample tested with hydrogen charging.

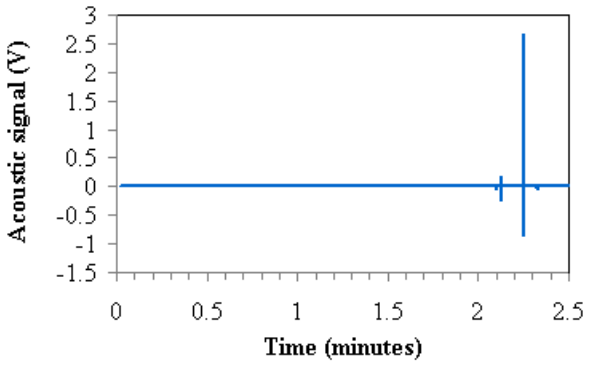

(a)

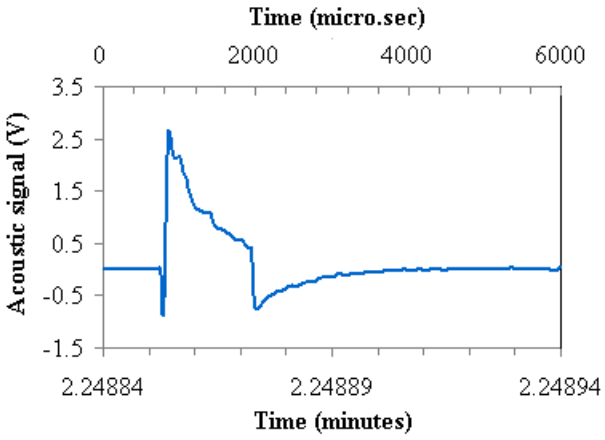

(b)

Figure 5.25 Acoustic emission spectra of the Fe-17.5 at.% Ga single crystal sample tested: (a) without hydrogen charging; and (b) an enlarged view of the highest intensity emission signal in 5.25 (a).

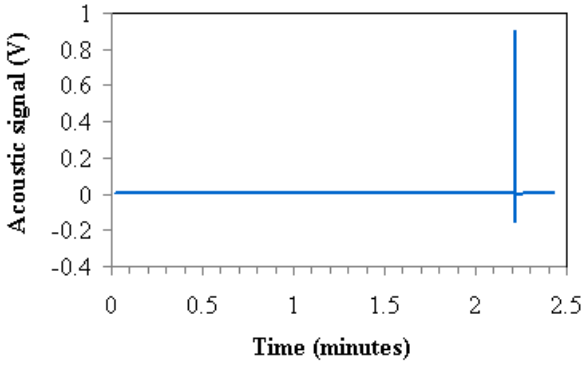

(a)

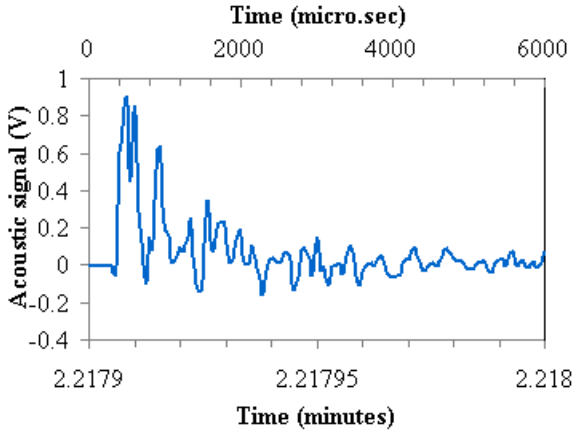

(b)

Figure 5.26 Acoustic emission spectra of the Fe-17.5 at.% Ga single crystal sample tested: (a) with hydrogen charging; and (b) an enlarged view of the highest intensity emission signal in 5.26 (a).

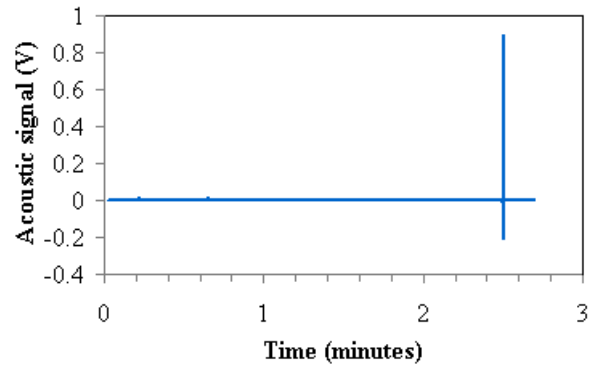

(a)

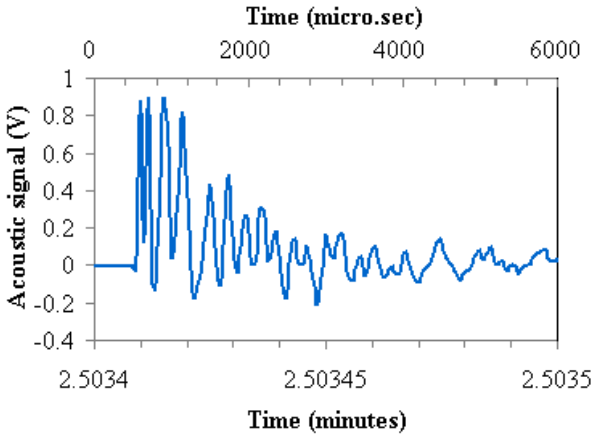

(b)

Figure 5.27 Acoustic emission spectra of the Fe-17.5 at.% Ga single crystal sample tested: (a) with hydrogen charging and magnetic field along the length axis; and (b) an enlarged view of the highest intensity emission signal in 5.27 (a).

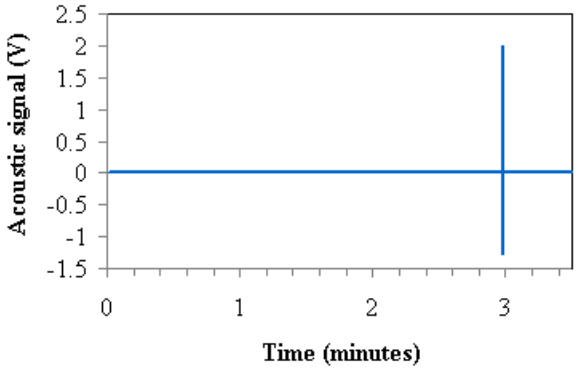

(a)

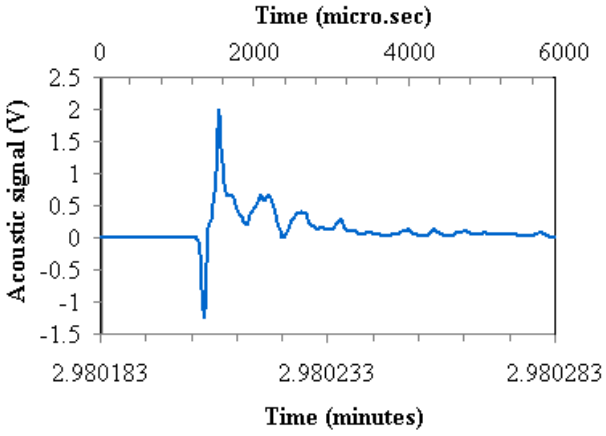

(b)

Figure 5.28 Acoustic emission spectra of the Fe-17.5 at.% Ga single crystal sample tested: (a) with hydrogen charging and magnetic field along the width axis; and (b) an enlarged view of the highest intensity emission signal in 5.28 (a).

5.27 (b) and 5.28 (b) show the acoustic emission signal for shorter time periods near the maximum intensity peaks of Figures 5.25 (a), 5.26 (a), 5.27 (a) and 5.28 (a), respectively.

The sample tested without hydrogen charging (Figure 5.25 (a)) is seen to have many emission events, indicating progressive crack growth occurring in multiple steps, whereas the samples tested with hydrogen charging (Figures 5.26 (a), 5.27 (a) and 5.28 (a)) show single emission events, indicating a rapid crack growth. The acoustic emission intensity in the case of the sample without hydrogen charging is much higher than that of the sample with hydrogen charging. This can be related to the fact that the ductile fracture process is a higher energy-consuming process than cleavage fracture [75]. It is observed that the intensity in case of the hydrogen charged sample tested with magnetic field applied along the width axis (Figure 5.28 (a)) lies between that of the sample tested without hydrogen charging (Figure 5.25 (a)) and the sample with hydrogen charging (Figure 5.26 (c)). This is consistent with the increase in the plastic deformation region seen in this sample (Figure 5.16 (d)). It is also observed that the magnified acoustic emission pattern corresponding to ductile fracture (Figure. 5.25 (b)) is distinctively different from that of brittle fracture (Figures 5.26 (b) and 5.27 (b)). A combination of these features is seen in the case of a sample with hydrogen charging and magnetic field along the width axis (Figure 5.28 (b)). The nonsinusoidal pattern observed in case of the sample tested without hydrogen charging and magnetic field (Figure 5.25 (b)) may also be attributed to a high signal intensity, which might have saturated the AE signal detector. Similar is the case of the hydrogen charged sample with magnetic field applied along the width axis (Figure 5.28 (b)), where the intensity is little less than in the case of Figure 5.25 (b), but is still high enough to saturate the detector.

5.7 Tensile Test Results

Tensile tests were carried out on Fe-15 at.% Ga polycrystalline samples in four different test conditions. The load versus displacement data acquired by the computer connected to the Instron machine were used to calculate the tensile stress and tensile strain. The tensile stress (σ) and tensile strain (ε) are given by equations (5.4) and (5.5), respectively.

$$\sigma = \frac{P}{WD} \quad (MPa) \tag{5.4}$$

$$\varepsilon = \frac{d}{L} \tag{5.5}$$

where, P is the load (N), W is the width of the sample (mm), D is the thickness of the sample (mm), d is the displacement (mm) and L is the gage length of the sample (mm).

From the tensile stress versus tensile strain plot, the yield strength, ultimate tensile strength and elongation value were found. For a quantitative estimate of the effect of hydrogen, HEI was also determined using the equation (5.3).

5.7.1 Tensile Test Results of Fe-15 at.% Ga Polycrystalline Samples

The consolidated tensile test results of Fe-15 at.% Ga alloy polycrystalline samples tested in four different test conditions are presented as tensile stress versus tensile strain plots in Figure 5.29. The yield strength, ultimate tensile strength and elongation values determined for these test samples are shown in Table 5.4.

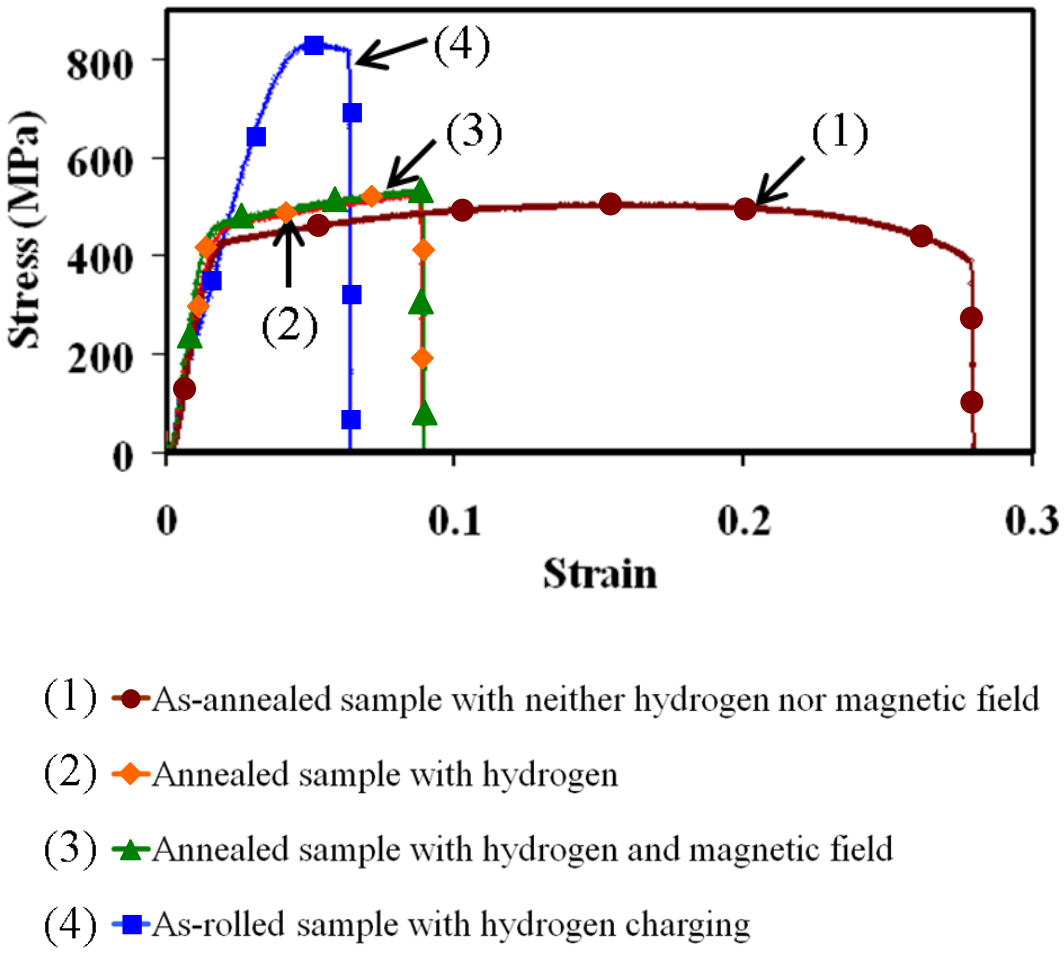

Figure 5.29 Tensile test results of Fe-15 at.% Ga samples tested under various test conditions.

Table 5.4

Tensile test results of Fe-15 at.% Ga polycrystalline samples tested under different test conditions.

Test conditions	**Elongation (%)**	**Yield Strength (MPa)**	**Ultimate Tensile Strength (MPa)**	**Hydrogen Embrittlement Index**
Annealed sample, with neither hydrogen charging nor magnetic field	28	425	500	-
Annealed sample, with hydrogen charging	9	450	525	68
Annealed sample, with hydrogen and magnetic field	9	450	525	68
As-rolled sample, with hydrogen charging	6.5	800	825	77

The tensile test result of the as-annealed sample shows a yield strength value of 425 MPa, an ultimate tensile strength of 500 MPa and elongation of 28 %. These properties are comparable to that of mild steel. The excellent ductility with high strength levels makes its suitable for sensor, power generation and actuator applications. The annealed sample tested with hydrogen charging is seen to have a yield strength value of 450 MPa, an ultimate tensile strength of 525 MPa with an elongation of 9 %. This result was the same in the case of the annealed sample tested with hydrogen charging and magnetic field. Therefore, it is observed that the presence of hydrogen drastically reduces the ductility of these alloys. This is well reflected in the HEI for this test condition being about 68. However, this decrease in ductility is accompanied by a slight increase in the strength. The as-rolled sample tested with hydrogen charging is seen to have a yield stress value of 800 MPa and an ultimate tensile strength value of 825 MPa with an elongation of about 6.5 %. This shows that in case of the as-rolled sample tested with hydrogen, the decrease in ductility and increase in strength is even more drastic and is about twice the magnitude observed in the case of the annealed alloy that was hydrogen charged. The HEI in this case is about 77.

The increase in strength can be attributed to the dislocation core pinning effect as reported by Hirth [80]. In the case of hydrogen charged samples, the hydrogen in the metal lattice pins the dislocation, thereby causing an increase in strength. In the case of the as-rolled sample, high dislocation densities present in the as-rolled alloy results in enhanced hydrogen trapping and higher hydrogen levels. Higher level of pinning of dislocations leads to the enormous increase in the strength level observed. Similar

observation of increase in strength was observed on 316L austenitic stainless steel by Matsuo et al. [81].

The samples with hydrogen charging in the presence of magnetic field did not seem to have much change in the ductility or strength values compared to those without magnetic field. But the effect of magnetic field was observed in case of Fe-17.5 at.% single crystal samples. This can be attributed to the polycrystalline nature of the sample, in which the orientation of each grain is nearly random, and the relatively low magnetic field that could be applied using the solenoid coil due to spatial constraints.

5.7.1.1 SEM Fracture Studies

Figures 5.30, 5.31 and 5.32 show the fracture surfaces of the Fe-15 at.% Ga alloy samples after tensile tests under various test conditions. The fracture surface of the hydrogen charged samples (Figures 5.30 (b), (c) and (d)) show brittle cleavage failure compared to the as-annealed surface showing plastic deformation typical of a ductile fracture (Figure 5.30 (a)). The fracture surface of the as-annealed sample (Figure 5.31 (a)) shows a combination of intergranular and transgranular mode of fracture, showing ductile tearing. The fracture surface of the as-rolled and hydrogen charged sample (Figure 5.31 (b)) shows a quasicleavage mode of brittle fracture. The fine tear ridges seen in the interior of the grains are typical of hydrogen embrittlement. There is not much of a difference seen between the fracture surfaces of annealed and hydrogen charged sample (Figure 5.32 (a)) compared to that with the presence of magnetic field (Figure 5.32 (b)). Grains are equiaxed and the fracture has closely followed grain boundaries, showing a predominantly intergranular fracture typical of hydrogen embrittlement.

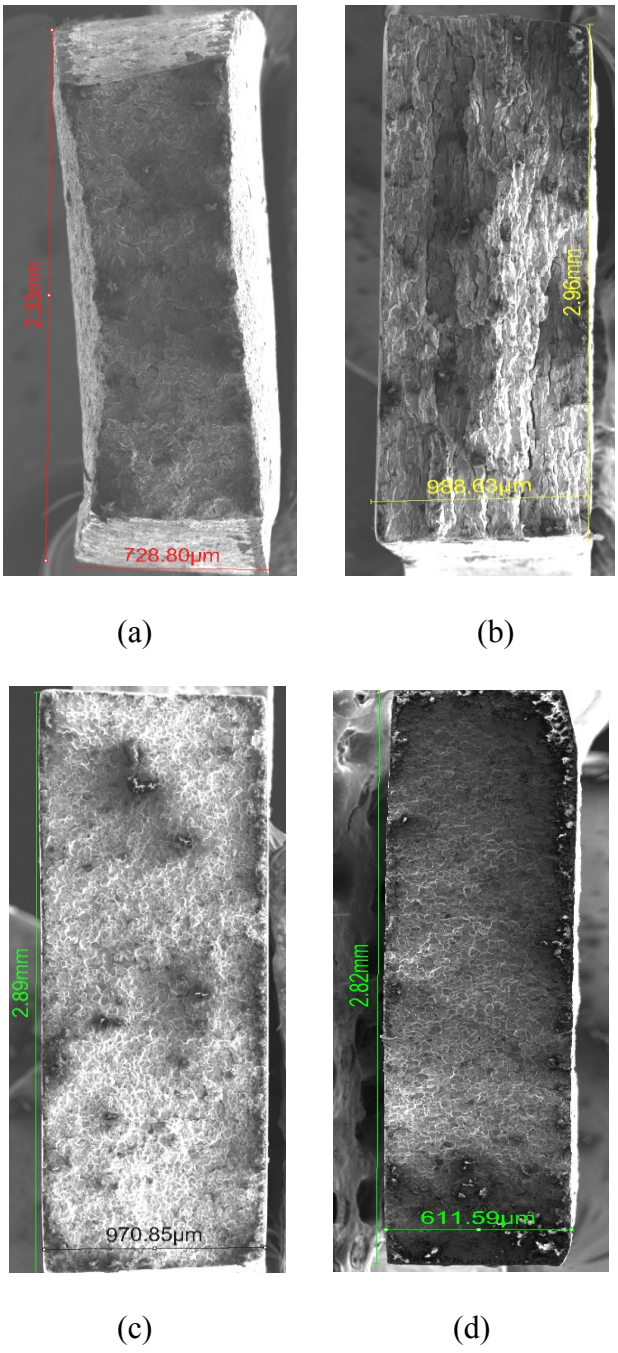

(a) (b)

(c) (d)

Figure 5.30 SEM fracture surface images of tensile tested Fe-15 at.% Ga alloy samples: (a) as-annealed; (b) as-rolled and hydrogen charged; (c) annealed and hydrogen charged; and (d) annealed and hydrogen charged in the presence of magnetic field.

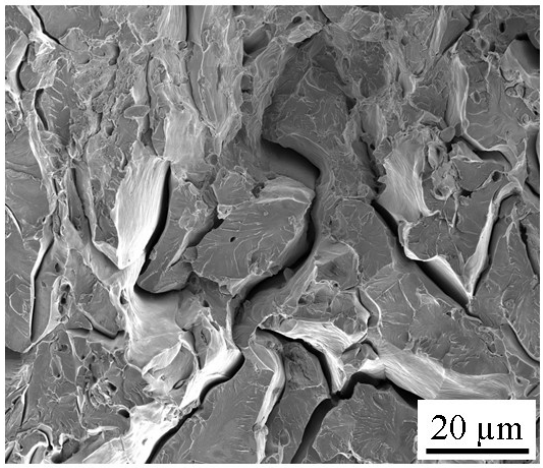

(a)

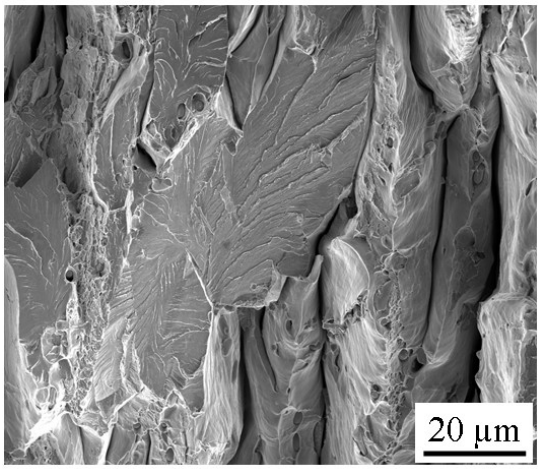

(b)

Figure 5.31 SEM fracture surface images of tensile tested Fe-15 at.% Ga alloy samples: (a) as-annealed; and (b) as-rolled and hydrogen charged.

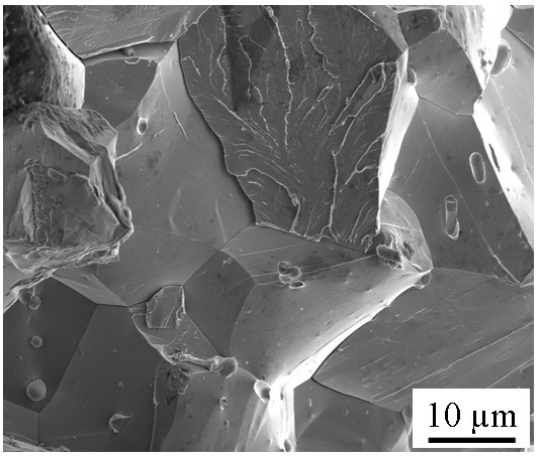

(a)

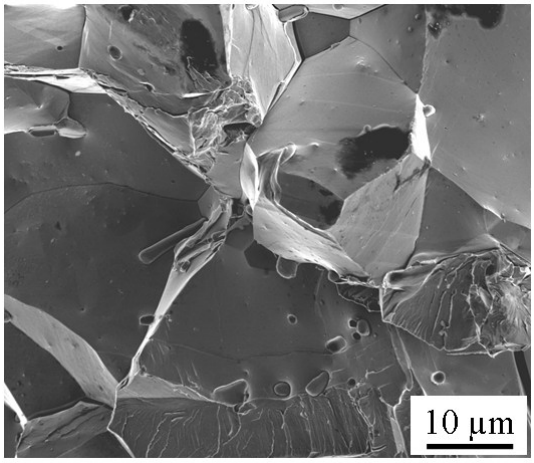

(b)

Figure 5.32 SEM fracture surface images of tensile tested Fe-15 at.% Ga alloy samples: (a) annealed and hydrogen charged; and (b) annealed and hydrogen charged in the presence of magnetic field.

CHAPTER 6

CONCLUSIONS

6.1 Three-Point Bend Test Results of Fe-17.5 at.% Ga Alloy Single Crystals

The effect of hydrogen and magnetic field on the mechanical properties of the [001] oriented Fe-17.5 at.% Ga alloy single crystal was studied using the three-point bend tests. The Fe-17.5 at.% Ga single crystal was grown using the vertical Bridgman technique and oriented samples for the three-point bend test were cut and polished. The prepared samples had one of the edges oriented within 0.3° from the [100] direction, whereas the other two edges were 6° away from the [010] and [001] directions, respectively. This alloy shows a large low-field magnetostriction coefficient value (3/2) λ_{100} of about 359×10^{-6}. The saturation magnetization value for the Fe-17.5 at.% Ga alloy was measured to be 173 emu/g. The transmission electron microscopy results show that the single crystal consists of a single phase (α-Fe phase).

Hydrogen charging in these alloys resulted in a drastic reduction of ductility and strength. The sample tested without hydrogen charging and magnetic field has a maximum bending stress of about 210 MPa and a bending strain of about 1.4 %. The sample tested with hydrogen charging has a maximum bending stress of about 132 MPa at a strain value of 0.9 %. This alloy has a hydrogen embrittlement index of 35.7. The

mode I cleavage fracture occurred along the (001) plane, and the observed maximum bending stress of about 132 MPa sets the upper bound for cleavage stress in this alloy. An applied magnetic field increases the bending strain value by about 10-20 % along with an increase in the cleavage stress value by about 20-25 %. This is associated with the changes in elastic modulus with applied field due to the large magnetostrictive nature of the sample. The fracture behavior is affected by the direction of applied magnetic field on the hydrogen charged samples, but it is difficult to interpret this result because of the gradual variation of stresses present from tensile to compressive in the bend test configuration. Detailed mathematical modeling is necessary to predict the magnetic domain structure in the presence of such stresses. Hydrogen embrittlement was characterized by a change in fracture surface from a ductile dimpled fracture surface to a brittle cleavage type fracture surface. The acoustic emission signals obtained appear to be consistent with the fracture behaviors.

6.2 Tensile Test Results of Rolled and Annealed Fe-15 at.% Ga Alloy

The effect of hydrogen and magnetic field on the mechanical properties of polycrystalline Fe-15 at.% Ga alloy samples were studied, using tensile tests. Electrochemical charging of hydrogen in these alloys resulted in a drastic reduction of ductility and strength. Increase in strength with hydrogen charging is observed, which is attributed to the dislocation core pinning effect, where the trapped hydrogen tends to increase the strength of the alloy by pinning of dislocations. This effect is drastic with a larger increase in strength in the case of as-deformed alloys, which is due to high

dislocation density in as-deformed alloy and high levels of hydrogen trapping by dislocations. Hydrogen embrittlement in these alloys was characterized by a change in fracture surface from a more ductile to a brittle cleavage type fracture. The effect of applied magnetic field seems to be relatively small in the case of polycrystalline annealed Fe-15 at.% Ga alloy. This could be attributed to the polycrystalline nature of the sample, in which the orientation of each grain is nearly random. This could also be due to a relatively low magnetic field that could be applied using the solenoid coil, due to spatial constraints.

6.3 Three-Point Bend Test Results of AISI 4340 Steel

The effect of hydrogen and magnetic field on the mechanical properties of AISI 4340 steel were studied on four sets of samples tested under five different test conditions, using the three-point bend test. This was carried out to check and validate the testing procedures prior to testing Fe-17.5 at.% Ga single crystals. The AISI 4340 steel sample tested with neither hydrogen charging nor magnetic field was observed to have a maximum bending stress of 438 MPa at a corresponding bending strain of 3.8 %. The effect of magnetic field on the sample tested without hydrogen charging was seen to be negligible. The sample tested with hydrogen charging was seen to have a drastic reduction in bending stress and bending strain values. The HEI for the sample tested with hydrogen charging shows a very high value of 76.32, indicating that the presence of hydrogen affects the material ductility drastically, and this alloy is highly prone to hydrogen embrittlement. The samples tested with hydrogen charging and magnetic field, applied both along the length axis and along the width axis, had similar bending stress

and bending strain values to that of the hydrogen charged sample tested without magnetic field. The HEI for hydrogen charged samples with and without magnetic field are similar. The fracture surfaces of the bend test sample shows that the hydrogen embrittlement in this alloy was characterized by a change in fracture surface from a more ductile to a brittle cleavage type fracture. The acoustic emission events observed are consistent with the fracture behavior and energy consumed during the fracture process.

APPENDIX

MAGNETIC TERMS - CONVERSION OF UNITS

Magnetic term	**Symbol**	**SI**	**CGS**	**Conversion factor**
Magnetic field	H	A/m	Oe	1 A/m = $4\pi/10^3$ Oe
Magnetic induction	B	T	G	1 T = 10^4 G
Magnetization	M	A/m	emu/cm^3	1 A/m = 10^{-3} emu/cm^3
Mass magnetization	σ	Am^2/kg	emu/g	1 Am^2/kg = 1 emu/g
Magnetic moment	m	Am^2	emu	1 Am^2 = 10^3 emu

Volume susceptibility	k	dimensionless	dimensionless	4π (SI) = 1 (CGS)
Mass susceptibility	χ	m^3/kg	emu/oe.g	1 m^3/kg = $10^3/4\pi$ emu/oe.g
Permeability of free space	μ_0	H/m	dimensionless	$4\pi \times 10^{-7}$ H/m = 1 (CGS)

REFERENCES

[1] B. D. Cullity, and C. D. Graham, *Introduction to Magnetic Materials*, 2nd ed., Hoboken, NJ: John Wiley & Sons, Inc., 2009.

[2] E. du Trémolet de Lacheisserie, *Magnetostriction: Theory and Applications of Magnetoelastcicity*, Ann Arbor, MI: CRC Press Inc., 1993.

[3] S. Guruswamy, N. Srisukhumbowornchai, A.E. Clark, J.B. Restorff, and M. Wun-Fogle, "Strong, ductile, and low-field-magnetostrictive alloys based on Fe-Ga," *Scripta Materialia*, vol. 43, pp 239-244, 2000.

[4] N. Srisukhumbowornchai, and S. Guruswamy, "Large magnetostriction in directionally solidified FeGa and FeGaAl alloys," *Journal of Applied Physics*, vol. 90, no. 11, pp 5680-5688, 2001.

[5] N. Srisukhumbowornchai, and S. Guruswamy, "Influence of ordering on the magnetostriction of Fe-27.5 at.% Ga alloys," *Journal of Applied Physics*, vol. 92, no. 9, pp 5371-5379, 2002.

[6] T.V. Jayaraman, R. P. Corson, and S. Guruswamy, "Ordering, magnetostriction, and elastic properties in Fe-27.5 at.% Ga alloy single crystals," *Journal of Applied Physics*, vol. 102, 053905, 2007.

[7] S. Guruswamy, T. V. Jayaraman, R. P. Corson, G. Garside, and S. Thuanboon, "Short range ordering and magnetostriction in Fe-Ga and other Fe alloy single crystals," *Journal of Applied Physics*, vol. 104, 113919, 2008.

[8] S. Guruswamy, G. Garside, C. Ren, B. Saha, and M. Ramanathan, "Ordering and magnetostriction in Fe alloy single crystals," *Progress in Crystal Growth and Characterization of Materials*, vol. 57, no.2-3, pp 43-64, 2011.

[9] T. V. Jayaraman, N. Srisukhumbowornchai, S. Guruswamy, and M. L. Free, "Corrosion studies of single crystals of iron-gallium alloys in aqueous environments," *Corrosion Science*, vol. 49, pp 4015-4027, 2007.

[10] T. V. Jayaraman, "Magnetostriction and corrosion studies in single crystals of iron-gallium alloys," Ph.D. dissertation, University of Utah, Salt Lake City, UT, 2007.

[11] N. Srisukhumbowornchai, "Development of highly magnetostrictive Fe-Ga and Fe-Ga-Al alloys," Ph.D. dissertation, University of Utah, Salt Lake City, UT, 2001.

[12] J. R. Cullen, A. E. Clarke, M. Wun-Fogle, J. B. Restorff, and T. A. Lagrasso, "Magnetoelasticity of Fe-Ga and Fe-Al alloys," *Journal of Magnetism and Magnetic Materials*, vol. 226-230, pp. 948-949, 2001.

[13] T. A. Lagrasso, A. R. Ross, D. L. Schlagel, A. E. Clark, and M. Wun-Fogle, "Structural transformations in quenched Fe-Ga alloys," *Journal of Alloys and Compounds*, vol. 350, pp. 95-101, 2003.

[14] A. E.Clark, J. B. Restorff, M. Wun-Fogle, T. A. Lograsso, and D. L. Schlagel, "Magnetostrictive properties of body-centered cubic Fe-Ga and Fe-Ga-Al alloys," *IEEE Transactions on Magnetics*, vol. 36, no. 5, pp. 3238-3240, 2000.

[15] A. E. Clarke, K. B. Hathaway, M. Wun-Fogle, J. B. Restorff, T. A. Lagrasso V. M. Keppens, G. Petculescu, and R. A. Taylor, "Extraordinary magnetoelasticity and lattice softening in bcc Fe-Ga alloys," *Journal of Applied Physics*, vol. 93, no. 10, pp. 8621-8623, 2003.

[16] S. Guruswamy, P. Mungsantisuk, R. Corson, and N. Srisukhumborwornchai, "Rare-earth free Fe-Ga based magnetostrictive alloys for actuator and sensors," *Transaction of Indian Institute of Metals*, vol. 57, no. 4, pp 315-323, 2004.

[17] R. A. Oriani, J. P. Hirth, and M. Smialowski, *Hydrogen Degradation of Ferrous Alloys*, Park Ridge, NJ: Noyes Publications, 1985.

[18] I. M. Bernstein, "The role of hydrogen in the embrittlement of Iron and Steel," *Material Science and Engineering*, vol. 6, pp 1-19, 1970.

[19] C. A. Zapffe, and C. E. Sims, "Hydrogen embrittlement, internal stress and defects in steel," *Transactions of American Institute of Mining and Metallurgical Engineers*, vol. 145, pp. 225-261, 1941.

[20] J. G. Morlet, H. H. Johnson, and A. R. Troiano, "A new concept of hydrogen embrittlement in steel," *Journal of Iron and Steel Institute*, vol. 189, pp. 37-44, 1958.

[21] A. R. Troiano, "The role of hydrogen and other interstitials in the mechanical behavior of metals," *Campbell memorial lecture, Transactions of the ASM*, vol. 52, pp. 54-80, 1960.

[22] R. A. Oriani, and P. H. Josephic, "Equilibrium aspects of hydrogen-induced cracking of steels," *Acta Metallurgica*, vol. 22, pp.1065-1074, 1974.

[23] N. J. Petch, and P. Stables, "Delayed fracture of metals under static load," *Nature*, vol. 169, pp. 842, 1954.

[24] S. Gahr, M. L. Grossbeck, and H. Birnbaum, "Hydrogen embrittlement of Nb I – Macroscopic behavior at low temperatures," *Acta Metallurgica*, vol. 25, no.2, pp. 125-134, 1977.

[25] C. D. Beachem, "New model for hydrogen-assisted cracking (hydrogen embrittlement)," *Metallurgical Transactions*, vol. 3, no. 2, pp 437-451, 1972.

[26] T. Matsumoto, J. Eastman, and H. K. Birnbaum, "Direct observation of enhanced dislocation mobility due to hydrogen," *Scripta Metallurgica*, vol. 15, no. 9, pp 1033-1037, 1981.

[27] H. K. Birnbaum, and P. Sofronis, "Hydrogen enhanced localized plasticity – a mechanism for hydrogen-related fracture," *Materials Science and Engineering*, vol. 176, pp. 191-202, 1994.

[28] S. C. Chang, and J. P. Hirth, "Hydrogen degradation of spheroidized AISI 1090 steel," *Metallurgical Transactions A*, vol. 16 (A), pp. 1417-1425, 1985.

[29] J. Mu, C. Hsiao, and W. Chu, "Effect of magnetization on hydrogen embrittlement of iron," *Scripta Metallurgica*, vol. 23, pp. 1015-1020, 1989.

[30] M. Ruscak, and T. P. Perng, "Combined effect of hydrogen and magnetization on the tensile properties of 2.25Cr-1Mo steel," *Scripta Metallurgica*, vol. 29, pp. 123-128, 1993.

[31] F. J. Sanchez, B. Mishra, and D. L. Olson, "Magnetization effect on hydrogen absorption in high-strength steels and its implications," *Scripta Materialia*, vol. 53, pp. 1443-1448, 2005.

[32] J. E. Jackson, A. N. Lasseigne-Jackson, F. J. Sanchez, D. L. Olson, and B. Mishra, "The influence of magnetization on corrosion in pipeline steels," *Proceedings of Sixth International Pipeline Conference*, Alberta, Canada, 2006.

[33] R. V. Williams, *Acoustic Emission*, Bristol, UK: Adam Hilger Ltd, 1980.

[34] J. Kaiser, "An investigation into the occurrence of noises in tensile tests or a study of acoustic phenomena in tensile tests," Ph.D. dissertation, Technische Hochschule – Munchen, Munich, Germany, 1950.

[35] J. R. Matthews, *Acoustic Emission*, New York, NY: Gordon and Breach Science Publishers, 1983.

[36] R. G. Liptai, D. O. Harris, and C. A. Tatro, *Acoustic Emission*, American Society for Testing and Materials - Special Technical Publication 505, 1972.

[37] H. L. Dunegan, "Using acoustic emission technology to predict structural failure," *Metals engineering quarterly*, pp. 8-16, 1975.

[38] H. L. Dunegan, and A. S. Tetelman, "Non destructive characterization of hydrogen embrittlement cracking by acoustic emission techniques," *Engineering Fracture Mechanics*, vol. 2, pp. 387-401, 1968.

[39] V. N. Kudryavtsev, W. Stengel, and R. Waterschek, "Detection of hydrogen embrittlement of a carbon steel by acoustic emission," *Corrosion*, vol. 37, no.12, pp. 690-695, 1981.

[40] P. McIntyre, and G. Green, "Acoustic emission during stress corrosion cracking in high strength steels," *British Journal of Non-Destructive Testing*, pp. 135-140, 1978.

[41] W. D. Callister, *Material Science and Engineering – An Introduction*, New York, NY: John Wiley and Sons Inc., 1996, pp. 659-686.

[42] S. Chikazumi, *Physics of Magnetism*, New York, NY: John Wiley and Sons Inc., 1964.

[43] H. Zijlstra, *Experimental Methods in Magnetism: Measurement of magnetic quantities*, vol. 2, New York, NY: American Elsevier Publishing Company Inc., 1967.

[44] J. E. Goldman, "Magnetostriction of annealed and cold worked nickel rods," *Physical Review*, vol. 72, no.6, pp. 529-530, 1947.

[45] J. H. Yoo, G. Pelligrini, S. Dutta, and A. B. Flatau, "An examination of Galfenol mechanical-magnetic coupling coefficients," *Smart Materials and Structures*, vol. 20, 075008, 2011.

[46] A. E Clark, and K. Hathaway, "Physics of giant magnetostriction," in *Handbook of Giant Magnetostrictive Materials*, G. Endahl, Ed. San Diego, CA: Academic Press, 2000, pp. 1-125.

[47] A. E. Clark, M. Wun-Fogle, J. B Restorff, T. A. Lograsso, and G. Petchulescu, "Magnetostriction and elasticity of body-centered cubic $Fe_{100-x}Be_x$ alloys," *Journal of Applied Physics*, vol. 95, no. 11, pp. 6942-6944, 2002.

[48] R. C. Hall, "Magnetostriction of aluminum-iron single crystals in the region of 6 to 30 atomic percent aluminum," *Journal of Applied Physics*, vol. 28, no. 6, pp. 707-713, 1957.

[49] S. Datta, M. Huang, J. Raim, T. A. Lograsso, and A. B. Flatau, "Effect of thermal history and gallium content on magneto-mechanical properties of iron-gallium alloys," *Material Science and Engineering A*, vol. 435-436, pp. 221-227, 2006.

[50] P. Mungsantisuk, R. Corson, and S. Guruswamy, "Influence of Be and Al on the magnetostrictive behavior of FeGa alloys," *Journal of Applied Physics*, vol. 98, 123907, 2005.

[51] S. Datta, and A. B. Flatau, "Measurement of magnetic field dependent Young's modulus of Iron-Gallium alloy in flexural mode," *Smart Structures and Materials*

2006: Active Materials: Behavior and Mechanics, W. D. Armstrong, Ed., Proceedings of SPIE, vol. 6170, 61700N, 2006.

[52] J. H. Yoo, and A. B. Flatau, "Measurement of field-dependence elastic modulus of iron-gallium alloy using tensile test," *Journal of Applied Physics*, vol. 97, 10M318, 2005.

[53] R. A. Kellogg, A. M. Russell, T. A. Lagrasso, A. B. Flatau, A. E. Clark, and M. Wun-Fogle, "Tensile properties of magnetostrictive iron-gallium alloys," *Acta Materialia*, vol. 52, pp. 5043-5050, 2004.

[54] P. R. Downey, and A. B. Flatau, "Magnetoelastic bending of Galfenol for sensor applications," *Journal of Applied Physics*, vol. 87, 10R505, 2005.

[55] S. Datta, J. Atulasimha, and A. Flatau, "Modeling of magnetostrictive Galfenol sensor and validation using four point bend test," *Journal of Applied Physics*, vol. 101, 09C521, 2007.

[56] D. Sachdeva, and R. Balasubramaniam, "The effect of hydrogen on corrosion of $Tb_{0.3}Dy_{0.7}Fe_{1.92}$," *Journal of Electrochemical Society*, vol. 155, no. 2, pp. c75-c80, 2008.

[57] H. Okamoto, "Phase diagrams of binary iron alloys," Monograph Series on *Alloy Phase Diagrams,* no. 9, H. Okamoto, Ed., Materials Park, OH: ASM International, 1993, pp. 147-151.

[58] W. H. Thomson, "On some remarkable changes produced in iron and steel by the action of hydrogen and acids," *Proceedings of the Royal Society of London*, vol. 23, pp. 168-179, 1875.

[59] M. A. V. Devanathan, Z. Stachurski, and W. Beck, "Technique for evaluation of hydrogen embrittlement characteristics of electroplating baths," *Journal of the electrochemical society*, vol. 110, no. 8, pp. 886-890, 1963.

[60] J. O. Bockris, J. McBreen, and L. Nanis, "Hydrogen evolution kinetics and hydrogen entry into α-iron," *Journal of the Electrochemical Society*, vol. 112, no. 10, pp. 1025-1031, 1965.

[61] I. A. Bagotskaya, *Zhurnal Fizicheskoi Khimii*, vol. 36, pp. 2667, 1962.

[62] A. N. Frumkin, *Advances in electrochemistry and electrochemical engineering*, P. Delahay, Ed., vol. 3, New York, NY: Interscience Publishers Inc., 1963.

[63] K. Kiuchi, and R. B. McLellan, "The solubility and diffusivity of hydrogen in well-annealed and deformed iron," *Acta Metallurgica*, vol. 31, pp. 961-984, 1983.

[64] K. T. Kim, J. K. Park, J. T. Lee, and S. H. Hwang, "Effect of alloying elements on hydrogen diffusivity in alpha iron," *Journal of Materials Science*, vol. 16, no. 9, pp. 2590-2596, 1981.

[65] T. P. Radhakrishnan, and L. L. Shreir, "Hydrogen permeation through iron and steels by electrochemical transfer – II; Influence of metallurgical factors on hydrogen permeation," *Electrochemical Acta*, vol. 12, pp. 889-903, 1967.

[66] R. A. Oriani, "The diffusion and trapping of hydrogen in steel," *Acta Metallurgica*, vol. 18, pp. 147-157, 1970.

[67] L. L. Shreir, R. A. Jarman, and G. T. Burstein, *Corrosion: volume 1 – Metal Environment Reactions*, Butterworth Heinmann, 1994.

[68] F. de Kazinczy, "Effect of stress on hydrogen diffusion in steel," *Jernkonttorets Annaler Arg*, vol. 139 (H), pp. 885-892, 1955.

[69] ASTM E1316-00, "Standard terminology for non-destructive examinations," American Society of Testing and Materials, 2000.

[70] D. D. Dedhia, and W. E. Wood, "Application of acoustic emission analysis to hydrogen-assisted cracking," *Materials science and engineering*, vol. 49, pp. 263-273, 1981.

[71] A. K. Bhattacharya, N. Parida, and P. C. Gope, "Monitoring hydrogen embrittlement cracking using acoustic emission technique," *Journal of materials science*, vol. 27, pp. 1421-1427, 1992.

[72] ASTM G129-00, "Standard practice for slow strain rate testing to evaluate the susceptibility of metallic materials to environmentally assisted cracking," American Society of Testing and Materials, pp. 533-539, 2006.

[73] ASTM E399-09, "Standard test method for linear-elastic plane-strain fracture toughness K_{IC} of metallic materials," American Society of Testing and Materials, pp. 516-548, 2009.

[74] ASTM E 855-08, "Standard test methods for bend testing of metallic flat materials for spring applications involving static loading," American Society of Testing and Materials, pp. 779-787, 2009.

[75] C. D. Beachem, "Microscopic fracture processes," *Fracture – An Advanced Treatise, Volume 1: Microscopic and Macroscopic Fundamentals*, H. Liebowitz, Ed. New York, NY: Academic Press, 1968, pp. 243-349.

[76] T. D. Lee, T. Goldenberg, and J. P. Hirth, "Effect of hydrogen on fracture of U-notched bend specimens of spheroidized AISI 1095 steel," *Metallurgical Transactions A*, vol. 10, pp. 199-208, 1979.

[77] C. Hwang, and I. M. Bernstein, "Hydrogen induced slip and twinning in iron alloys," *Scripta Metallurgica*, vol. 16, pp. 85-90, 1982.

[78] F. Sorbello, P. E. J. Flewitt, G. Smith, and A. G. Crocker, "The role of deformation twins in brittle crack propagation in iron-silicon steel," *Acta Materialia*, vol. 57, pp. 2646-2656, 2009.

[79] S. P. Lynch, "Herring bone patterns on fracture surfaces," *Scripta Metallurgica*, vol. 20, pp. 1067-1072, 1986.

[80] J. P. Hirth, "Effects of hydrogen on the properties of iron and steel," *Metallurgical Transactions A*, vol. 11 (A), pp. 861-890, 1980.

[81] T. Matsuo, J. Yamabe, S. Matsuoka, and Y. Murakami, "Influence of hydrogen and prestrain on tensile properties of type 316L austenitic stainless steel," *Effects of Hydrogen on Materials, Proceedings of the 2008 International Hydrogen Conference,* B. Somerday, P. Sofronis, R. Jones, Eds., ASM International, 2009, pp. 105-112.